INFORMATION TO USERS

This manuscript has been reproduced from the microfilm master. UMI films the text directly from the original or copy submitted. Thus, some thesis and dissertation copies are in typewriter face, while others may be from any type of computer printer.

The quality of this reproduction is dependent upon the quality of the copy submitted. Broken or indistinct print, colored or poor quality illustrations and photographs, print bleedthrough, substandard margins, and improper alignment can adversely affect reproduction.

In the unlikely event that the author did not send UMI a complete manuscript and there are missing pages, these will be noted. Also, if unauthorized copyright material had to be removed, a note will indicate the deletion.

Oversize materials (e.g., maps, drawings, charts) are reproduced by sectioning the original, beginning at the upper left-hand corner and continuing from left to right in equal sections with small overlaps.

Photographs included in the original manuscript have been reproduced xerographically in this copy. Higher quality 6" x 9" black and white photographic prints are available for any photographs or illustrations appearing in this copy for an additional charge. Contact UMI directly to order.

ProQuest Information and Learning
300 North Zeeb Road, Ann Arbor, MI 48106-1346 USA
800-521-0600

Université d'Ottawa • University of Ottawa

Investigation of Bose-Einstein Condensation Effects with Excitons in Cu_2O

By

Mathieu Massé

Thesis submitted to the
Faculty of Graduate and Postdoctoral Studies
in partial fulfillment of the requirements
for the degree of Master of Science in Physics

Department of Physics

University of Ottawa
Ottawa, Ontario
January 8, 2001

Abstract

Experimental observations are presented on Bose-Einstein condensation of excitons in Cu_2O at low temperatures. These observations deal with traveling exciton packets in a high quality natural crystal. The properties of the exciton packets are examined using two different excitation depths of formation of the excitons (affecting the size of initial exciton cloud). The properties of the condensate include for example: the amplitude, the velocity of the exciton packet, the critical conditions for condensation and phase diagram. Interference effects of two coherent packets are also studied using these different initial excitation depths. Stimulated emission of particles into the exciton packet by injection of thermal excitons in the crystal volume is investigated in greater detail as well as the attenuation of the lateral laser beam (used to create the thermal excitons that trigger the amplification phenomenon).

Sommaire

Des observations expérimentales de la condensation de Bose-Einstein d'excitons dans le Cu_2O á basses températures seront présentées. Ces observations portent sur des paquets d'excitons voyageant dans un cristal naturel de haute qualité. Les propriétés du paquet d'excitons sont examinées en utilisant deux profondeurs d'excitation pour la formation des excitons (grosseurs initiales des nuages d'excitons). Les propriétés du condensat incluent par exemple: l'amplitude du paquet, sa vitesse, les conditions de formation d'un condensat et un diagramme de phase. Les effets d'interférence entre deux paquets cohérents sont aussi étudiés en utilisant ces deux profondeurs d'excitation initiale. L'émission stimulée de particules dans le paquet d'excitons par l'injection d'excitons thermiques est étudiée en plus grand détail ainsi que l'atténuation du faisceau laser latéral (utilisé pour créer les excitons thermiques qui déclenchent le phénomène d'amplification).

Acknowledgements

I would like to thank Dr. Fortin for his help and support during this project. I also thank Eric Benson, André Merizzi, Mitch Campbell, John Taylor, Nicholas Sabourin and Luc Charron for help and discussions during these last two years. And finally I must thank my parents for giving me the opportunity to continue my studies at the graduate level and last but not least Josée for listening to me talk about my experiments and problems all the time.

Statement of Originality

Unless otherwise stated the results presented in this thesis come from experiments performed by the author at the University of Ottawa. Some of the results printed in this thesis were presented at the following conferences:

- Excitonic Superfluidity in Cu_2O, M. Massé and E. Fortin, ACFAS in Ottawa, May 1999.
- Excitonic Superfluidity in Cu_2O, M. Massé, E. Fortin and E. Benson, CAP conference in Fredericton, June 1999.
- Spatially dependent amplification of an excitonic Bose-Einstein condensate in Cu_2O, M. Massé and E. Fortin, CAP conference at York University, June 2000.
- Investigation of Bose-Einstein Condensation Effects with Excitons in Cu_2O, M. Massé, OCIP Graduate Student Seminar, December 2000.

Results appearing in publications:

- Spatially dependent amplification of an excitonic Bose-Einstein condensate in Cu_2O, E. Fortin and M. Massé, *Inter. Jour. of Mod. Phys.*, Accepted.

Contents

List of Figures

List of Tables

Introduction

Atomic Bose-Einstein condensates are widely studied, in particular Sodium and Rubidium condensates. The temperatures needed to achieve these condensates are in the mK range, making them hard to observe. However Bose-Einstein condensation (BEC) of excitons in Cu_2O has also been the subject of many researches in the last ten years [1, 2, 3] and are achievable at liquid helium temperatures. The experimental results have raised debates among theoreticians [4, 5, 6, 7, 8]. The most recent theory proposed includes the effect of the coupling between excitons and phonons [4, 9]. Bose-Einstein condensation of excitons has been extensively observed and analyzed; the basic properties of the exciton packet, including interference phenomenon and stimulated emission, have been well established [10]. Investigation on the effect of the initial packet conditions (different sizes of exciton clouds and phonon populations) are still lacking in observations and explanations.

The excitons are used for BEC because they are an easily available boson system, obtainable through optical absorption. The low effective mass of the exciton enables BEC to be achievable at temperatures in the liquid ^{4}He range. Also, the paraexcitons (excitons with spin zero) have a rather long lifetime, providing a chance to observe exciton transport over long distances, this by non-optical detection (the transition of the paraexciton state to the ground state being forbidden).

This research is mainly focused on the formation of the packet using two different laser penetration depths (affecting the size of the initial exciton cloud and the phonon population). The exciton packets have previously been created within a few atomic layers of the crystal due to the penetration depth of the exciting laser pulse: we present here results of traveling exciton packets created in a bigger volume of the crystal and comparing them with the results obtained previously [10, 11]. To verify different properties of an exciton packet we need to vary different initial parameters, such as: the initial density of the packet, the bath temperature of the crystal and also the wavelength of the laser beam used to create thermal excitons for the stimulated emission phenomenon

(this permits to see the interaction of the exciton packet, when amplified, with phonons by using wavelengths that create different phonon populations in the crystal).

Another important phenomenon is the interference between two excitonic condensates; it can be attributed in our case to BEC [12]. Two coherent condensates can interfere in the crystal to produce one condensate, not equal to the mathematical sum of the two initial exciton signal. The interference experiments are redone using different initial dynamics (different initial penetration depth of the laser pulse) to see if they influence the interference properties of the resulting condensate.

Stimulated particle emission into the condensate is the last phenomenon studied in this thesis. Stimulated emission of particles into the condensate is achieved by laterally injecting into the crystal a beam or a pulse of laser created thermal excitons. It is observed that the thermal excitons created by the lateral beam trigger non-condensed excitons surrounding and following the condensed packet to fall into this one. These observations are made by analyzing the amplification of the condensate and the attenuation of the pulsed lateral laser as the position of the lateral pulse is varied relatively to the position of the traveling exciton packet (we can decide which part of the exciton packet gets hit by the thermal excitons).

The thesis is separated into four chapters. Chapter one deals with the related theory behind the experiments: BEC itself, excitons and the different phenomena attributed to BEC. The different experimental setups including lasers, data acquisition, etc..., are presented in chapter two. Chapter three presents the experimental results and interpretations dealing with the initial dynamics of the exciton packets: the effects on the properties of the packets and the interference phenomenon. Stimulated emission of particles in the condensate using a lateral pulse of excitons is presented separately in chapter four.

Chapter 1

Theory

This chapter deals with the essentials of the theory of Bose-Einstein condensation. The basic properties of the system in which condensation is achieved experimentally are introduced in the following sections. Effects related to Bose-Einstein condensation are also presented.

1.1 Bose-Einstein Condensation

At low temperature and high density, quantum effects are an important factor in the interaction between particles in a system. In this regime the particle's wave functions determine the type of interactions. There are two types of quantum particles: fermions and bosons. A fermion (half-integer spin particle) wave function is odd under particle exchange

$$\Psi(r_1, r_2) = -\Psi(r_2, r_1), \tag{1.1}$$

where the boson (spin-integer particle) is even under particle exchange

$$\Psi(r_1, r_2) = \Psi(r_2, r_1). \tag{1.2}$$

Two properties arise from the symmetry of the particle wave function: fermions can only have one particle occupying a single quantum state, while an unlimited number of bosons can occupy a single quantum state. The phenomenon of Bose-Einstein condensation (BEC) has the last property as its main cause. This new state of matter (the superfluid state) has properties that are quite different from the ones we usually deal

with: liquid, solid and gas; and these differences are caused by the particle's wave functions symmetry. The main properties that are unique to a superfluid is irrotational flow and that it is resistance free (the viscosity goes to zero).

1.1.1 Ideal Bose Gas

To explain BEC, one needs to know what an ideal Bose gas is. An ideal Bose gas is a system where quantum statistics are the dominant factor in the behaviour of the particles but with negligible interactions. To examine the properties of an ideal Bose gas we need to take a look at the partition function of the system. Starting with the boson partition function L, in the Grand Canonical Ensemble:

$$L(z,V,T) = \sum_{N=0}^{\infty} z^N e^{\beta \sum \varepsilon_{\vec{p}} f_{\vec{p}}} = \prod_{\vec{p}} \left[\sum_{f_{\vec{p}}} \left(z e^{-\beta \varepsilon_{\vec{p}}} \right)^{f_{\vec{p}}} \right], \tag{1.3}$$

where N is the number of particles, V the volume, T the temperature, $f_{\vec{p}}$ is the occupation number of a state with energy $\varepsilon_{\vec{p}}$, $\vec{p}$ is the momentum, β is equal to $\frac{1}{k_B T}$ and z is the fugacity (the fugacity is related to the chemical potential μ by $z = e^{\beta\mu}$). The total number of particles is limited by $\sum f_{\vec{p}} = N$. For bosons, $f_{\vec{p}}$ is any positive integer, since the number of particles in a state is unlimited. The sum over $f_{\vec{p}}$ becomes a geometric series $\left(\sum_{s=0}^{\infty} r^s = \frac{1}{1-r}\right)$ reducing the partition function for bosons to:

$$L(z,V,T) = \prod_{\vec{p}} \frac{1}{1 - z e^{-\beta \varepsilon_{\vec{p}}}}. \tag{1.4}$$

With this partition function one can get the equations of state:

$$\frac{PV}{k_B T} = \log L(z,V,T) = -\sum_{\vec{p}} \log(1 - z e^{-\beta \varepsilon_{\vec{p}}}), \tag{1.5}$$

$$N = z \frac{\partial}{\partial z} \log L(z,V,T) = \sum_{\vec{p}} \frac{z e^{-\beta \varepsilon_{\vec{p}}}}{1 - z e^{-\beta \varepsilon_{\vec{p}}}}. \tag{1.6}$$

In the limit as $V \to \infty$ the possible values of $\vec{p}$ form a continuum and the sum over $\vec{p}$ in eq. 1.5 and 1.6 is replaced by an integration such that $\sum_{\vec{p}} \to V \cdot \frac{2s+1}{h^3} \int d^3\vec{p}$ where s is the particle spin and h is Planck's constant. Rewriting eq. 1.5 and 1.6 one gets:

$$\frac{P}{k_B T} = -\frac{4\pi \cdot (2s+1)}{h^3} \int_0^{\infty} dp\, p^2 \log(1 - z e^{-\beta p^2/2m}) - \frac{1}{V} \log(1-z), \tag{1.7}$$

$$n = \frac{4\pi \cdot (2s+1)}{h^3} \int_0^{\infty} dp\, p^2 \frac{1}{z^{-1} e^{\beta p^2/2m} - 1} + \frac{1}{V} \frac{z}{1-z}. \tag{1.8}$$

One notices in those two equations that the ground state term has been split from the sum before the conversion to an integral. For bosons the ground state term can be as important as the rest of the states. One can now integrate eq. 1.7 and 1.8 to find the relation between P, n, T and z:

$$\frac{P}{k_B T} = \frac{(2s+1)}{\lambda^3} g_{5/2}(z) - \frac{1}{V}\log(1-z), \tag{1.9}$$

$$n = \frac{(2s+1)}{\lambda^3} g_{3/2}(z) + \frac{1}{V}\frac{z}{1-z}, \tag{1.10}$$

where $\lambda = \sqrt{\frac{2\pi\hbar^2}{mk_B T}}$ and $g_n(z)$ is the sum $g_n(z) \equiv \sum_{l=1}^{\infty} \frac{z^l}{l^n}$. From the partition function one can also find the average occupation number $< f_{\vec{p}} >$:

$$< f_{\vec{p}} >= -\frac{1}{\beta}\frac{\partial}{\partial \varepsilon_{\vec{p}}} \log L = \frac{z e^{-\beta\varepsilon_{\vec{p}}}}{1 - z e^{-\beta\varepsilon_{\vec{p}}}}. \tag{1.11}$$

The average occupation number $< f_{\vec{p}} >$ is simply $z/(1-z)$ for the ground state ($\varepsilon_{\vec{p}} = 0$). Therefore, one can rewrite the eq. 1.11 as:

$$\frac{< f_0 >}{V} = n - \frac{2s+1}{\lambda^3} g_{3/2}(z). \tag{1.12}$$

This equation implies that there is a finite number of particles in the ground state if:

$$n > \frac{2s+1}{\lambda^3} g_{3/2}(z). \tag{1.13}$$

This macroscopic occupation of the ground state is called Bose-Einstein condensation. Replacing the values of λ and $g_{3/2}(z)$ at $z = 1$, one can write a critical density above which the particles will condense into the ground state:

$$n_c = 2.612 \cdot (2s+1) \cdot \left(\frac{mk_B}{2\pi\hbar^2}\right)^{3/2} T^{3/2}. \tag{1.14}$$

One can also find the fraction of particles that will condense by rearranging eq. 1.12 and by dividing both sides by the density n:

$$\frac{< f_0 >}{N} = 1 - \frac{2s+1}{n\lambda^3} g_{3/2}(z). \tag{1.15}$$

We replace $g_{3/2}(z)$ by $g_{3/2}(1)$ since for the condensed fraction to be non-zero, $z \to 1$. Using $g_{3/2}(1) = \frac{n\lambda_c^3}{2s+1}$, where λ_c is calculated at the critical temperature T_c, and putting this result in eq. 1.15 we get:

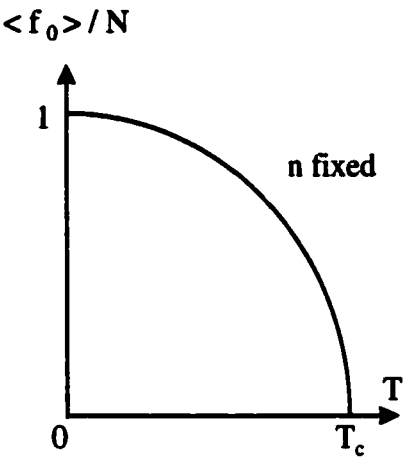

Figure 1.1: Average occupation of the ground state as a function of temperature.

$$\frac{< f_0 >}{N} = \begin{cases} 1 - \left(\frac{T}{T_c}\right)^{3/2} & T \leq T_c \\ 0 & T \geq T_c \end{cases} . \tag{1.16}$$

Equation 1.16 is graphically represented in fig. 1.1; we can see that only a certain fraction of the particles will occupy the ground state for $T < T_c$. For $T > T_c$ no energy level is occupied by a finite fraction of all the particles; in this case the particles are spread over all energy levels. For example in our experiments we typically get fractions of $\sim 95\,\%$ ($T = 2\,K$, $T_c = 16\,K$, initial density of $10^{18}\,cm^{-3}$) of condensed particles.

The pressure of the gas can be calculated using eq. 1.9, the last term of that equation can be ignored since it is of the order $\log(N)$ compared to the first term of the order N. This has for effect that no particle in the ground state contributes to the pressure. Using the same procedure as for $< f_0 > /N$ we get P as a function of T:

$$P = \begin{cases} g_{5/2}(z) \cdot (2s+1) \cdot k_B T/\lambda^3 & n < n_c \\ 1.342 \cdot (2s+1) \cdot k_B T/\lambda^3 & n > n_c \end{cases} , \tag{1.17}$$

where $g_{5/2}(1) \cong 1.342$ for $n > n_c$. In fig. 1.2 the pressure is plotted as a function of the density, for three temperatures. The density is simply related to the temperature by substituting $T = cst \cdot n^{2/3}$ for $z = 1$ from eq. 1.14 into eq. 1.17. The dashed line represents the critical pressure for BEC, proportional to $n^{5/3}$. A notable feature of this graph is the saturation of the pressure of the gas in the condensed regime. This is a direct indication of the phase change of the particles from gas to condensed gas. After the transition, breaks in the properties of the gas will be apparent.

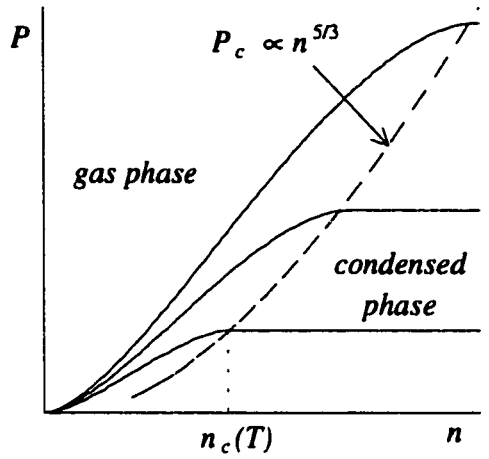

Figure 1.2: Isotherms of an ideal Bose gas.

1.1.2 Condensate Properties

One of the properties of a condensate is superfluidity, as observed in liquid ^{4}He, below the λ-point of 2.17 K, and linked with BEC. The condensate has two components: a normal component formed of all the particles in the excited states ($\varepsilon_{\vec{p}} \neq 0$) and a superfluid component composed of the particles in the ground state ($\varepsilon_{\vec{p}} = 0$). The normal component will behave as a classical gas (low density) or a liquid (high density). The superfluid component behaves differently: it has irrotational flow, meaning that the condensate will move as a whole. This is derived from general principles of quantum mechanics, stating that since the particles are invariant under translation (consequence of the fact that there is macroscopic occupation of a single state), the condensate is described by a single wave function (product of all the condensed particle's wave functions).

The condensate can also be viewed as a wave (matter wave) with a definite phase: as a consequence interference should occur between two condensates, this will be treated in sec. 1.3.

Excitons in a semiconductor crystal have been used here in experiments on Bose-Einstein condensation; this system of bosons is described in the next section.

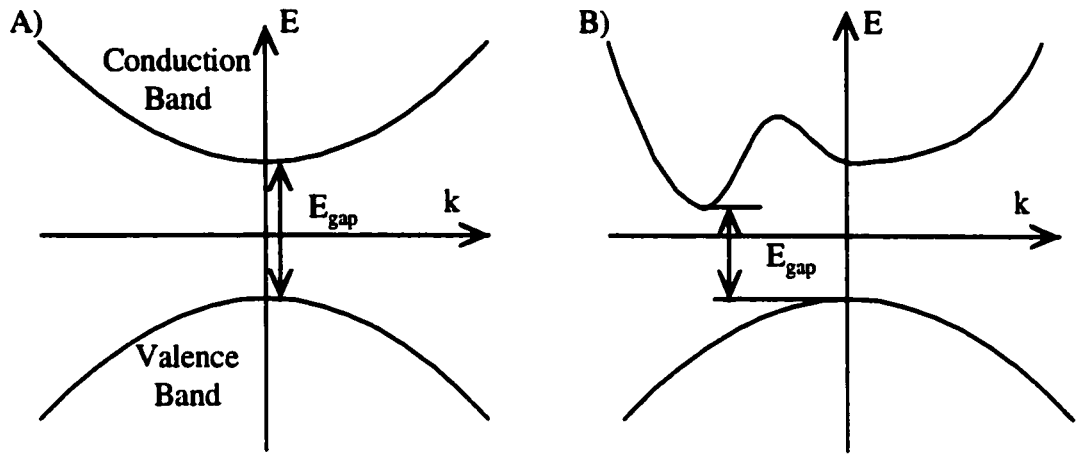

Figure 1.3: Band structure for A) direct gap, B) indirect gap semiconductor.

1.2 Exciton System

1.2.1 Semiconductor Energy Bands

Electrons in a crystal are confined to energy bands. These bands, formed by the periodicity of the crystal lattice, are separated by a forbidden gap (band gap) where no energy levels are permitted. The highest filled band is called the valence band and the next band (after the band gap) is called the conduction band. The band gap is the major factor for determining the properties of a crystal. A crystal behaves as an insulator when the allowed energy bands are either full or empty (no electrons can move). In the other extreme, in a metal the band is partially filled (10 to 90 % filled) so there is no problem to have conduction. A semiconductor is situated between these two extremes.

The energy bands of a semiconductor can result in either a direct gap or an indirect gap. These gaps will be a function of the electron wavevector $\vec{k}$. We say a gap is direct when the lowest energy transition requires no change in electron momentum $\hbar\vec{k}$. For the indirect gap, there is a change in momentum by phonon absorption or emission. Figure 1.3 shows a representation of the two common band structures.

The probability of excitation of an electron by the absorption of a photon is dependent on the density of states of the initial and final energy levels. Experimentally, this probability can be represented by the absorption coefficient α which is a function of the incident photon wavelength. The intensity of light (I) which is transmitted in crystal at a distance z is given by the Beer-Lambert law:

$$I = I_0 e^{-\alpha z}, \tag{1.18}$$

where I_0 is the intensity of light incident on the crystal surface.

1.2.2 Excitons

When an electron is excited by light with an energy greater than the energy of the gap, it is promoted to the conduction band and cascades down to the excitonic level in the gap, the excess energy is converted into phonons. The electron left an empty hole in the valence band which can be viewed as particle of positive charge. The electron and the hole are still physically close to each other. They bind (they have opposite charges) and form a new entity called an exciton, much in the same way a proton and an electron combine to form a hydrogen atom; however for the exciton the Coulomb interaction is screened by the periodic lattice field, and the masses of the components are much smaller. Since the spin of the electron is $\pm 1/2$ and the hole is $\pm 1/2$, the combination of the two results in a neutral particle with a spin of zero or one, making it a boson. Excitons with spin one are labeled orthoexcitons and excitons with spin zero are called paraexcitons.

The binding energy of the excitons follows the same type of series as for the hydrogen atom, but modified by the parameters ε and μ, which take in account the screening effect of the ions in the lattice:

$$E_B = \frac{e^4 \mu_{ex}}{2\hbar^2 \varepsilon^2 n^2} \qquad n = 1, 2, 3, \ldots , \tag{1.19}$$

where e is the electronic charge, ε is the static dielectric constant ($\simeq 7$ in Cu_2O [13]) and $\mu_{ex} = m_e m_h/(m_e + m_h)$ is the exciton reduced mass with m_e and m_h the electron and hole respective effective masses. From fig. 1.4 (schematic of eq. 1.19) we can see that the exciton energy levels are located in the band gap of the crystal. This will allow absorption of photons in the region supposed to be transparent to light.

There are two types of excitons, apart from ortho-para excitons: Frenkel and Wannier excitons. The difference between the two is the radius of the exciton (half the distance between the electron and the hole). The Frenkel excitons have a radius smaller/or of the order of the lattice constant and are bound to their parent atoms; Wannier excitons have a radius larger than the lattice constant and are free to move throughout the crystal. The exciton radius is given by:

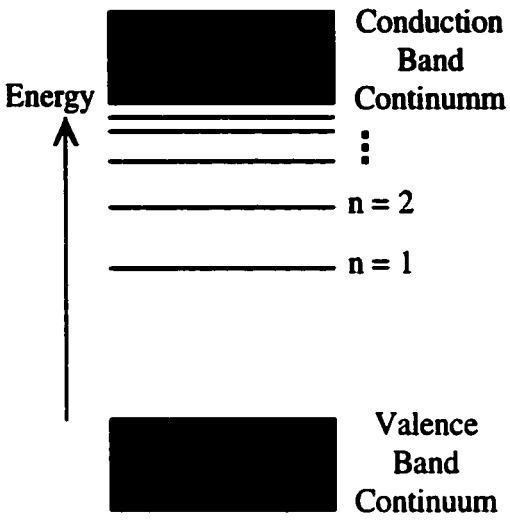

Figure 1.4: Exciton energy levels for $\vec{k} = 0$.

$$r_{ex} = a_0 \frac{m_0}{\mu_{ex}} \varepsilon n^2, \tag{1.20}$$

where a_0 is the Bohr radius and m_0 is the free electron mass.

The time between creation and recombination of the electron and hole pair is the exciton lifetime τ ($\approx 8\,msec$ [14] for Cu_2O at $2\,K$). The probability of recombination is governed by the quantum selection rules and the density of state of the initial and final energy state. However, the electron and the hole can be induced to recombine by thermal fluctuations or by the presence of an electric field of the same order of magnitude as that of the field in between the electron and the hole (see sec. 2.1). This electric field can be generated by a defect in the crystal lattice (impurity ions), or the field can be created for the purpose of recombination by a Schottky barrier in the exciton path.

The density of excitons created by the laser pulse in the crystal will vary with depth and can be calculated by the following method: the density of excitons in a layer dz parallel to the surface is equal to the loss of photons by absorption in dz divided by dz; here we have to assume that each photon produces one exciton. By using eq. 1.18 and the fact that $I(z) \propto \frac{N(z)}{A}$ where $N(z)$ is the number of photons in the crystal at the distance z from the surface of illumination A, the density will be given by:

$$n(z) = -\frac{1}{A}\frac{d}{dz}N(z) = -\frac{1}{A}\frac{d}{dz}N_0 e^{-\alpha z} = \frac{\alpha N_0}{A} e^{-\alpha z}, \tag{1.21}$$

where α the absorption coefficient and N_0 is the number of incident photons. For eq. 1.21 to be valid, the absorption time of the photons in the crystal must be smaller than the

exciton lifetime. This is no problem because the absorption time is less than $10^{-12}\,sec$ compared to the lifetime of $8\,msec$.

The density of excitons created in the crystal can be controlled by the incident laser intensity and also by the laser light wavelength (via the dependence on the absorption coefficient of the crystal).

1.2.3 Exciton Condensation

The excitons in Cu_2O have a mass of $2.7\,m_0$ [15] and a radius of $\approx 0.7\,nm$ [16], making them behave much like an ideal Bose gas. The exciton gas must be dilute and the condition for this is $nr_{ex}^3 << 1$, where n is the exciton density. This criterion is satisfied in Cu_2O for densities up to $\approx 10^{20}\,cm^{-3}$ (we will see in sec 2.3 that we do not reach densities of that magnitude). The small radius of the exciton prevents Mott dissociation (breakdown of the exciton into an electron-hole plasma). This transition occurs when $nr_{ex}^3 \approx 0.3$ (for copper oxide $n = 10^{21}\,cm^{-3}$). A repulsive exciton-exciton potential [17] insures that there will be no formation of biexcitons (molecules consisting of two exciton) and provides stability for the moving condensate described in this section.

The critical density n_c needed to achieve BEC is calculated with eq. 1.14; this gives for paraexcitons at a temperature of $2\,K$:

$$n_c \cong 8 \times 10^{16}\,cm^{-3}, \tag{1.22}$$

which corresponds to a dilute gas compared to the criterion mentioned above. To compare with achievable experimental exciton densities we use the following equation:

$$n_{ex} = \frac{photons\ absorbed \cdot \alpha \cdot 0.63}{area}, \tag{1.23}$$

where 0.63 replaces $e^{-\alpha z}$ in eq. 1.21: this corresponds to the fraction of excitons absorbed in an absorption length $(1/\alpha)$. We can substitute in eq. 1.23 the number of photons in a laser pulse at the maximum intensity possible with our laser, the absorption coefficient at the wavelength of the laser and the area of illumination used. We thus get an average density for our two wavelengths:

$$\begin{aligned} n_{ex} &= \frac{8 \times 10^{14} \cdot 1.25 \times 10^{2}\,cm^{-1} \cdot 0.63}{3 \times 10^{-2}\,cm^2} \cong 2 \times 10^{18}\,cm^{-3} \qquad for\ \lambda = 585\,nm \\ n_{ex} &= \frac{8 \times 10^{14} \cdot 3 \times 10^{3}\,cm^{-1} \cdot 0.63}{3 \times 10^{-2}\,cm^2} \cong 5 \times 10^{19}\,cm^{-3} \qquad for\ \lambda = 532\,nm \end{aligned} \tag{1.24}$$

this maximum initial density yields a density much higher than the critical density needed for BEC, but does not exceed the criterion for a dilute gas and the criteria for Mott dissociation.

The theoretical density calculated in eq 1.22 assumed that the exciton gas is at lattice temperature; this is not true in our case, since the excitons are created indirectly: the electron is excited high in the conduction band and cascades down to the exciton energy level by shedding its excess kinetic energy in the form of phonons, which leads to the heating of the exciton gas. Also at high exciton density, Auger processes can occur (an exciton recombines emitting a photon which is absorbed by another exciton) leading again to heating the exciton gas and reducing its density. The heating effect at high exciton densities ($10^{18} - 10^{19}\,cm^{-3}$) can produce exciton gas temperatures up to $30\,K$ [18].

The lattice will also be heated by phonons; the thermal energy Q is equal to the number of photons times the excess energy of each photon. This excess energy is given by $E_\lambda - E_{n=1}$. $E_{n=1}$ corresponds to the energy of the paraexciton in the $n = 1$ level ($2.021\,eV$ see sec. 2.3). The next set of equations is used to evaluate the final lattice temperature in the volume delimited by the illumination area and one absorption length:

$$\begin{aligned} Q &= m \cdot c(T) \cdot \Delta T, \\ N_0 \int dE &= m \int_{T_0}^{T_f} c(T) dT, \\ n_{ex}\left(E_\lambda - E_{n=1}\right) &= \frac{\rho c_0}{4}\left[T_f^4 - T_0^4\right], \end{aligned} \tag{1.25}$$

where $c(T) = c_0 T^3$ ($c_0 = 5.86 \times 10^{-6}\,J/g \cdot K$) is the specific heat capacity at low temperature in Cu_2O [19], $\rho = 6.14\,g/cm^3$ is the mass density of Cu_2O, T_f and $T_0 = 2\,K$ are the final and initial temperatures. At an exciton density of $3 \times 10^{20}\,cm^{-3}$ and a wavelength of $532\,nm$ we get a final temperature of $27\,K$; and for $\lambda = 585\,nm$ at the same density we get $T_f = 20\,K$. However spectroscopic measurements have shown that the exciton gas reaches thermal equilibrium with the bath temperature ($2\,K$) after approximately $30\,nsec$ [20], so condensation should occur some short time after the pulse.

The exciton packet propagates away from the illumination surface by means of a large density gradient:

$$\Delta n(z) = \frac{d}{dz} n(z) = \frac{-\alpha^2 N_0}{A} e^{-\alpha z}, \tag{1.26}$$

due to the large absorption coefficient. If a condensate forms in the crystal it will travel drag-free to the opposite face of creation (due to the superfluidity of the condensate).

It will propagate at a velocity close to the velocity of sound in Cu_2O, which is $v_s = 4.5 \times 10^5\, cm/s$ [21], and as a coherent cloud (see next section). If the cloud of excitons does not condense (due to low density or high temperature, i.e., below critical conditions) it will still diffuse to the opposite face of creation, but at a reduced velocity due to drag from interaction with the crystal lattice; broadening of the packet should also be observed. The diffusion length l of normal excitons in a high quality crystal is of the order of 1 to $2\,mm$ and since the crystal thickness is $1.94\,mm$ the superfluid component will have to be distinguished form the normal component by means of a change in the properties (eg. velocity, amplitude, etc) of the traveling cloud of excitons.

A solution to superfluid travel of exciton condensates has been proposed by Loutsenko and Roubtsov [4]. They propose that the interaction between excitons and phonons play a key role when the velocity of propagation of the condensate is near the sound velocity. The Hamiltonian of the model has three separate terms: an exciton term, a phonon term and an interaction with an exciton-phonon potential. The most important result is the prediction of a critical velocity v_0 above which the sign of the effective potential changes, from repulsive to attractive. The critical velocity for Cu_2O is $\sim 0.5 - 0.7\, v_s$. Above the velocity of sound the potential returns to repulsive. Propagation of the condensate in $v_0 < v < v_s$ leads to a family of stable stationary solutions. The resulting particle distribution has the form of a soliton:

$$n(x) = n_0 sech^2\left(\frac{x - x_0}{\Delta}\right) \qquad \frac{1}{\Delta} = \beta n_0, \tag{1.27}$$

where x_0 is the soliton peak position, the spatial width Δ is related to the soliton amplitude n_0 by the parameter β. This solution corresponds to our condensed packet.

The theory of Loutsenko and Roubtsov also predicts that below the critical velocity a stable condensate cannot propagate; therefore below the critical velocity the transport of the packet is diffusive and the particle distribution has the form:

$$n(x,t) = \frac{n_0}{\sqrt{4\pi D t}}\, exp\left(\frac{-(x - vt)^2}{4Dt}\right) exp\left(\frac{-t}{\tau}\right), \tag{1.28}$$

which is the 1D solution of the diffusion equation with drift term:

$$\frac{\partial n}{\partial t} = D\frac{\partial^2 n}{\partial x^2} - v\frac{\partial n}{\partial x} - \frac{n}{\tau}, \tag{1.29}$$

where v is the drift velocity, D is the diffusion coefficient and τ is the particle lifetime. The drift term may originate from the coupling of excitons with LA phonons produced by the exciton cooling described in this section. Compared to the superfluid regime, in

the diffusive regime the width of the packet increases as a function of time (this in fact defines the diffusion coefficient).

1.3 Condensate Interference[1]

Two ideal classical gas clouds cannot display interference because there is no coherence between the two. The arbitrary phase of the cloud is a result of the superposition of the individual particle wave functions, which are in this case uncorrelated.

If all the particles are in the same state (the condensate), they all have the same wave function. This has for effect that the cloud now inherits the coherence present between the particles; the cloud now has a definite phase. If two condensates have a definite phase relationship they are said to be mutually coherent and can interfere.

Since the condensate can be described by a solitary wave, and the medium in which it propagates is nonlinear, the mechanism behind interference is not as simple as linear superposition of coherent waves giving rise to a set of maxima and minima in the resulting wave, as usually associated with interference. However in nonlinear optic, there is a phenomenon that deals with interaction between two femtosecond high intensity laser pulses which is similar to our experimental system. The coherent laser field is replaced, in our case, by the coherent exciton-phonon polarization field of high amplitude that describes our condensate. The nonlinear response of the crystal can be expressed as a perturbation expansion in odd terms of the polarization field limited to fifth order:

$$-i\frac{\partial\psi}{\partial t} = a\frac{\partial^2\psi}{\partial x^2} + b|\psi|^2\psi - c|\psi|^4\psi. \tag{1.30}$$

The waves will interact according to the fundamental interactions of their constituents (excitons). Therefore the first nonlinear term corresponds to the attractive two-body interaction. The higher order nonlinear term corresponds to the three body repulsive interaction preventing biexciton formation. The case of two condensates traveling uniformly in the same direction separated by an initial distance has been solved numerically (1D case was assumed, the contribution of thermal exciton was ignored) [11]. The initial conditions used were the following:

$$\psi(x,t) = [A_1(x,t) + A_2(x,t+\tau)]\, e^{iw(t-x/v)},$$

[1]It was pointed out that a more appropriate term for condensate interference would be nonlinear interaction between two coherent condensates.

$$|A_i(0,t)|^2 = |A_{0,i}|^2 sech^2\left(\frac{t}{\Delta}\right), \tag{1.31}$$

experimental results were fitted to $|\psi|^2(x,t)$ using the numerical solution [11].

Transverse interference (i.e. two condensate separated by a distance perpendicular to their common propagation direction) is also possible. However the theory of Loutsenko and Roubtsov says that the attractive potential changes sign and becomes repulsive for interaction perpendicular to the propagation direction, rejecting the possibility of transverse interference. No other models have been proposed yet, but observations have been presented: constructive interference leading to the formation of a larger or denser packet is observed.

1.4 Amplification of a Condensate

In sec. 1.1 we saw that bosons can have multiple occurrences in a given quantum state, as compared to fermions which obey the Pauli exclusion principle. This has for effect that the scattering probability of a boson, in a state already occupied by other bosons is enhanced by a factor of $f+1$, f being the occupation number of the final state. This means that quantum attraction can occur if the final state is occupied by a high number of bosons. Light amplification by stimulated emission of radiation (LASER) is a good example of this effect using massless bosons (photons). This is only a specific example, because amplification by stimulated emission is a much more general effect that can be applied to any bosonic field. In our experiments we observe stimulated emission of optically inactive paraexcitons (this is done without participation of radiation).

The basic exciton scattering process (spontaneous form) consists of the annihilation of an exciton with energy E_i and wavevector $\vec{K}_i$, the creation of an exciton with energy E_f and wavevector $\vec{K}_f$ and the simultaneous emission (or absorption) of an acoustic phonon, we thus deal with a three body elementary process. This is the chain of events that occur after injection of hot excitons in the crystal, leading to the energy relaxation and establishment of a quasi-thermodynamic equilibrium.

The initial exciton (E_i, $\vec{K}_i$) is coupled to a continuum of final states, defined by the set of vector ($\vec{K}_f$, $\vec{q}$) which satisfy energy and momentum laws:

$$E_i = E_f \pm \hbar\omega_q \qquad \vec{K}_i = \vec{K}_f \pm \vec{q}, \tag{1.32}$$

with the following additional constraint:

$$E_{i,f} = \frac{\hbar^2 K_{i,f}^2}{2m}, \qquad \hbar\omega_q = \hbar\vec{q}v, \tag{1.33}$$

where v is the longitudinal sound velocity and m the exciton effective mass. From the point of view of excitonic motion, this succession of spontaneous events leads to the diffusive exciton transport modeled by the diffusion equation.

In the stimulated version of the process, an incident exciton field (f_c, E_c, $\vec{K}_c$) induces the exciton scattering, where $f_c > 1$ is the occupation number of mode c. Additional conditions are prescribed for the direction and magnitude of $\vec{K}_f$ and $\vec{q}$:

$$E_f = Ec \qquad \vec{K}_f = \vec{K}_c \tag{1.34}$$

The time rate change of the average number of bosons in mode c gives the growth of the bosonic rate [22]:

$$\begin{aligned}\frac{\partial f_c}{\partial t} = \frac{2\pi}{\hbar}\sum_q \gamma^2(q)\{f_{c+q}(1+f_c)[(1+f_q)\delta(\hbar\omega_q + E_c - E_{c+q}) \\ + f_q\delta(\hbar\omega_q - E_c + E_{c+q})] - (1+f_{c+q})f_c[(1+f_q)\delta(\hbar\omega_q - E_c + E_{c+q}) \\ + f_q\delta(\hbar\omega_q + E_c - E_{c+q})]\}\end{aligned} \tag{1.35}$$

where $f_i = f_{c+q}$ and f_q are respectively the occupation probability of excitons and acoustic phonons with energy E_k and $\hbar\omega_k$ and $\gamma(q) = \gamma_0 \cdot \sqrt{q}$ is the matrix element of the exciton-phonons interaction. An excitonic Bose condensate with $f_c >> 1$ on the R.H.S. of eq. 1.35 can provide the triggering term for stimulated excitonic transition. Stimulated exciton scattering can still occur even below Bose condensation threshold because modes near $\vec{K} = 0$ have already large occupation numbers in the quantum-degenerate statistical regime. In eq. 1.35 the amplification process is expressed by the first term, while the second one expresses the loss process where an exciton is scattered out of the mode f_c by the creation of an exciton of wavevector $\vec{K}_c \pm \vec{q}$. The amplification of the traveling exciton condensate is achieved by stimulated exciton scattering induced by the excitonic field (f_c, E_c, $\vec{K}_c$), if the stimulated exciton emission overcomes the induced exciton absorption (a net gain will be achieved).

The population inversion and gain from stimulated emission process (assumed in a laser), is not necessary in the exciton stimulated emission when the photon character vanishes (no radiation) [23]. It is noted that in fact stimulated emission can be observed at densities under the critical density for BEC [23].

Chapter 2

Experiment

This chapter presents the description of the exciton detector, sample preparation, data acquisition and the optical setups used for the experiments on Bose-Einstein condensation of excitons.

2.1 Exciton Mediated Photovoltaic Effect

Photoluminescence failed to prove the existence of Bose-Einstein condensation of orthoexcitons in Cu_2O [20, 21, 24, 25, 26]. The reason is that the orthoexciton's lifetime is $\sim 1\,nsec$, making its photoluminescence a measure of excitons at initial times in the crystal. The paraexciton has a longer lifetime but a low radiative efficiency making detection by luminescence very difficult; a non-optical method is instead needed to observe the paraexcitons. The detection method used in this project is the exciton mediated photovoltaic effect [27]. The effect was first used for solar cells, to convert sunlight into electrical energy [28].

Figure 2.1 is a representation of this basic method. A semi-transparent gold layer is deposited on the front surface of the Cu_2O sample and a copper electrode on the back surface. The gold contact is an ohmic contact; it can pass a large current with only a small voltage. The copper contact is a rectifying contact; the respective Fermi levels at the interface (Cu/Cu_2O) line up and lead to a bending of the energy bands. The potential barrier ϕ_B at the interface is of the order of $1\,V$ [28, 29]. This results in a high electric field region W (depletion width) which extends to a depth of $10 - 100\,nm$ in Cu_2O [30]. This will create a local static electric field of the order of $\phi_B/W \sim 10^5 - 10^6\,V/cm$. The required field to dissociate an exciton in Cu_2O is of the order $E_B/(r_{ex}e) \sim 10^6\,V/cm$, so a fraction of the excitons will be dissociated and detected as an external current or

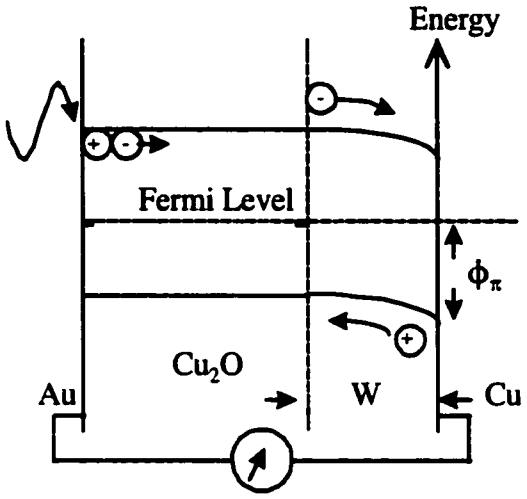

Figure 2.1: Basic idea of the exciton mediated photovoltaic effect.

voltage depending on the resistance between the gold and the copper electrodes. A small resistance will produce an external current and a large resistance an external voltage.

This setup (fig. 2.1) is only used with low intensity laser light. For high intensity ($multimegawatt/cm^2$ pulsed illumination) and for time-resolved measurements, needed for observation of Bose-Einstein condensation, another arrangement for the electrodes is needed because the high power of the laser beam would damage the gold electrode. Also, the high series impedance ($\sim 10^9\,\Omega$) of the sample at low temperature would result in long time constants for the detected signal (nanosecond resolution is needed for our experiment). To correct this, we need to deposit both the gold electrode and the copper electrode on the same surface and opposite to the illumination face. Several types of electrode were studied and the arrangement in fig. 2.2 was the one producing the highest excitonic signal amplitude [3]. The copper electrode is the same size as the illumination spot of the laser creating the exciton cloud ($2\,mm$ diameter) and is surrounded by a ring of gold (see sec. 2.2.3). The effective detector region ($\approx$ size of copper patch) is $0.03\,cm^2$ and $10 - 100\,nm$ deep. The detector impedance is now given by the separation between the copper and gold electrodes; it is a bit hard to measure, since each time the electrodes are redone the separation can be different due to the deposition technique. This detector will only measure excitons that have traveled through the crystal, because the crystal acts as a light filter. Light which, by reflection within the sample holder, reaches the detector directly will produce a photosignal used in our case as a reference timing.

The linearity and the efficiency of the detector was studied at $532\,nm$ by illuminating the detector directly with the laser light [10]. The detector linearity was confirmed over

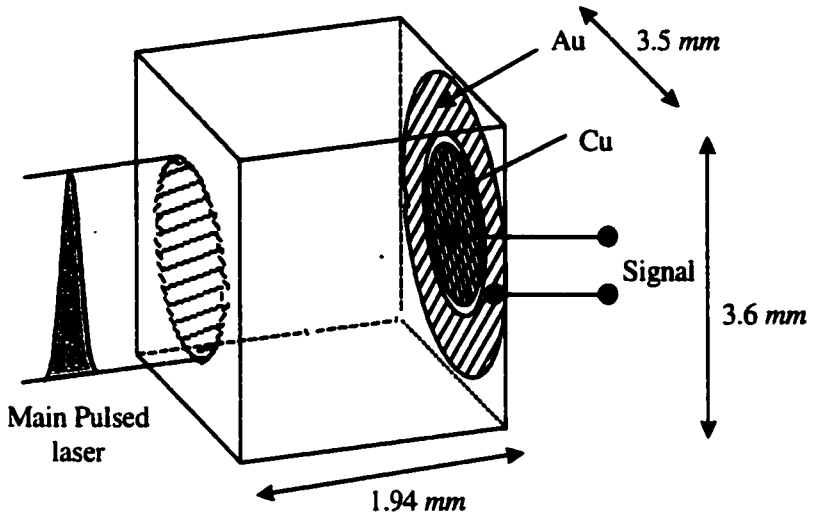

Figure 2.2: Electrode configuration for high intensity time-resolved photovoltaic detection.

many orders of magnitude of light intensity and the observed efficiency was of the order of 1%. If the detector is illuminated with weakly absorbed laser light in the time resolved geometry (see fig. 2.2), the efficiency η is reduced to 0.1%, since the electrodes are not illuminated directly. These two results are in agreement with efficiencies obtained by solar cell researchers [31]. The signal $S(t)$ in mV as a function of time is thus given by the following equation:

$$S(t) = \eta n(t) v A \tag{2.1}$$

where $n(t)$ is the density of excitons as a function of time, v the velocity of the excitons and A the detector area.

2.2 Sample Preparation

The crystal used during the experiments is a high quality natural single crystal cut into a parallelepiped oriented in the <100> direction by a crystallographer. The crystal size varied during the experiments due to polishing and chemical etching. The crystal size was $1.97 \times 3.8 \times 3.8\, mm^3$ at the beginning of this project and at the end the size dropped to $1.94 \times 3.5 \times 3.6\, mm^3$ due to polishing.

Step 1	9.5 μm Al_2O_3 powder on glass sheet with distilled water for $\sim 1\,min$, longer if epoxy and/or electrodes are present. N.B. This step is the one removing the most material but the epoxy and/or the electrodes *must* be removed.
Step 2	Rinse with distilled water/methanol solution in ultrasonic cleaner. Wipe dry with tissue paper.
Step 3	1 μm diamond paste on Microcloth with polishing fluid for $\sim 15\,min$.
Step 4	Rinse with distilled water/methanol solution in ultrasonic cleaner. Carefully touch dry with optical tissue paper.
Step 5	0.25 to 1 μm diamond powder on Microcloth with no lubricant for $\sim 1\,min$.
Step 6	Rinse with distilled water/methanol solution in ultrasonic cleaner. Carefully touch dry with optical tissue paper.

Table 2.1: Polishing steps.

2.2.1 Polishing

The sample needs to be polished to remove scratches and marks on the crystal as the large scratches will be enlarged during the chemical etch. Also previous electrodes and/or epoxy for the contacts have to be removed. The sample polishing consists of a few basic steps (see table 2.1). These steps are mostly a guideline, since polishing is more an art than a science; results can vary due to operator skill and experience. The times are also more of a suggestion: if one step is done rapidly the next step will have to be done longer.

The polishing is done by holding the sample between two fingers or under one finger depending on the crystal's size. Step 3 and 5 are done on a variable speed turntable. The higher the speed of the turntable the faster the polishing will be. The restriction on the speed is mostly the dexterity of the operator: the sample can easily be dropped if the speed is too high. The best way to know when to change powder is to look at the sample through a microscope; if no visible improvements are made, it is time to change the powder. After polishing, the crystal should have a nice reflective surface.

2.2.2 Chemical Etching

The chemical etching is performed on the sample after the polishing is done. It is used to remove the top atomic layers of the crystal that have been damaged during the polishing. It also permits future electrodes to adhere to the crystal more easily (otherwise they could

Step 1	Rinse in distilled water.
Step 2	Soak for 1 *min* in methanol with final 20 *sec* in ultrasonic cleaner.
Step 3	Etch for 3 *min* in HBF_4 ($\sim 5\,\mu m/min$), then dilute quickly with distilled water.
Step 4	Repeat step 1 and 2.
Step 5	Soak for 90 *sec* in Bromine(2% vol.)/Methanol solution with final 30 *sec* in ultrasonic cleaner.
Step 6	Repeat step 2 and 6.
Step 7	Repeat step 2 and 1. Then quickly blow dry with He or N_2 to eliminate water spots.

Table 2.2: Chemical etching procedures.

scratch off). The procedures in table 2.2 were designed by solar cell researchers and proven to lower surface recombination and to maximize the barrier field at the Cu/Cu_2O interface [32].

2.2.3 Electrode Deposition

The electrodes needed for the exciton detector are deposited on a polished face of the crystal using thermal evaporation. Before the deposition, masks are applied to the crystal to produce the gold ring or the copper disk pattern. The masks are used to consistently deposit the electrodes with a separation of 250 μm between the two. Four guide posts in the mask holder are used to achieve concentricity between the two masks. The crystal is aligned in the mask holder using Teflon screws. The gold ring pattern is deposited first in two steps, because of the shape of the mask(see fig. 2.3). One needs to carefully center the crystal in the mask holder, making sure that the copper electrode will be placed in the middle to maximize its efficiency. The second deposition is needed to close out the ring of the gold electrode; this is done by rotating the mask by 180^o. The copper electrode is deposited last to minimize exposure to heat of the Cu/Cu_2O interface (this would oxidize the crystal surface into amorphous CuO). Again close inspection is necessary to see if the electrode is centered. The electrodes are evaporated to a thickness of around $80 - 100\,nm$, this is to prevent penetration of the epoxy used to secure the electrical leads.

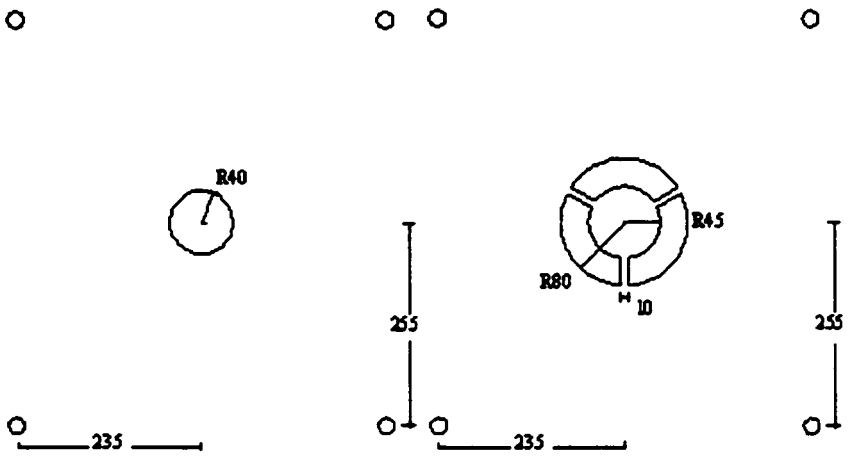

Figure 2.3: Mask configuration. The units are μm and the values starting with a R stand for a radius of x μm.

Step 1	Set sample firmly in sample holder.
Step 2	Solder gold wires to vacuum feedthroughs.
Step 3	Cut wire to desired length.
Step 4	Bend end of wire into a small foot.
Step 5	Position wire foot on the electrode.
Step 6	Deposit a small drop of epoxy on the foot of the wire to make contact.
Step 7	Let cure for at least 48 hours.

Table 2.3: Wire bonding procedures.

2.2.4 Wire Contacts

To collect the signal from the electrodes small (50 μm diameter) gauge gold wires are needed. The difficulty in this step is attaching the wires on the electrodes; a two-part silver conducting epoxy is used for this task. Epo-Tek 410E was used here because it cures at room temperature and survives many thermal cycles. The procedures for bonding the wire contact to the electrodes is summarized in table 2.3.

The amount of epoxy needed can be judged by practicing on a microscope slide until the desired quantity is achieved. The epoxy bond can be removed with the use of cotton swabs and methanol; this also removes the gold electrode. Polishing is needed to remove the copper electrode, since it will partly diffuse into the crystal [28].

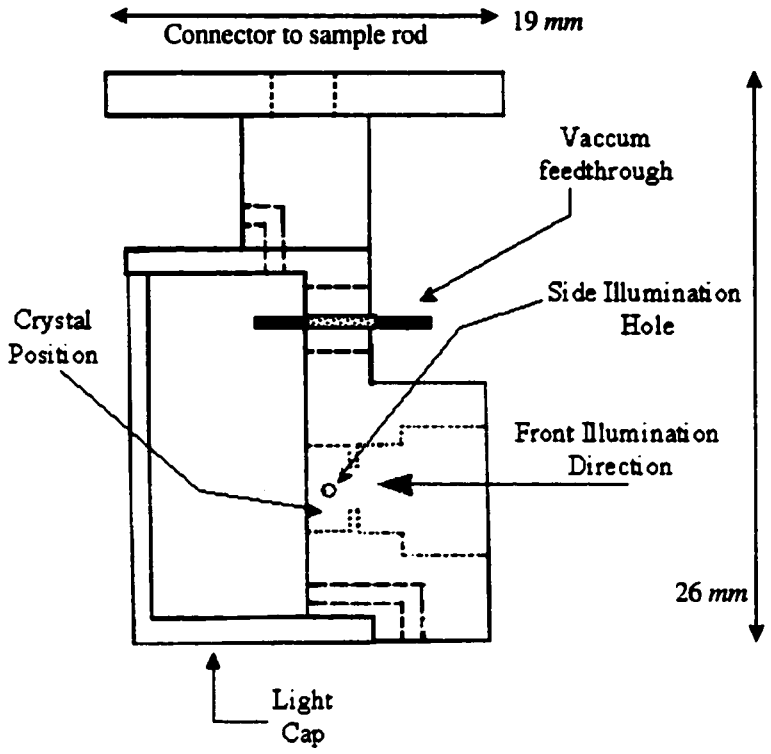

Figure 2.4: Side view of the sample holder.

2.2.5 Sample Holder

A special sample holder was designed to properly fix the sample in the optical cryostat. It is made out of copper to reduce differential thermal contractions with the sample and to provide a good medium to keep the crystal at the bath temperature. The sample holder used for the experiments was built at the Science shop of the University of Ottawa. The holder consists of a cylinder block with a cavity into which the crystal is deposited (see fig. 2.4). A 2 *mm* diameter illumination hole is placed centered on the crystal, where the main laser beam hits the crystal. A laser beam can also illuminate the sample on its lateral side, through a hole (1 *mm* diameter) positioned at 1 *mm* from the crystal surface (see sec. 2.4.5 and 2.4.6 for the use of this hole). This hole traverses the sample holder from one side to the other to permit the measurement of transmitted lateral light. The holder is covered with a Delrin light cap to prevent most of the stray light from hitting the electrodes directly. Vacuum feedthroughs provide a solid position for attaching the coaxial cable transmitting the signal out of the cryostat.

2.3 Lasers

The high density of excitons needed for the BEC experiments are created optically in the crystal with high intensity lasers. Four lasers are used for our experiments: a frequency doubled pulsed Nd:YAG laser operated at 10 pulses per second, a pulsed dye laser pumped by the Nd:YAG, a CW Ar^+ gas laser and a CW dye laser pumped by the Ar^+ laser; all are vertically polarized .

The Nd:YAG laser has an output wavelength of $532\,nm$ and a pulse duration of $8\,nsec$. This laser is used to create the exciton cloud that will either diffuse or ballistically move through the crystal. The absorption coefficient (α) of the crystal at this wavelength is $3 \times 10^3\,cm^{-1}$ (penetration depth of $3\,microns$). The peak power of the Nd:YAG is around $15\,MW$.

The pulsed dye laser pumped by the Nd:YAG laser produces output in the visible spectrum. The wavelengths used with this laser are: $585\,nm$ ($\alpha = 1.25 \times 10^2\,cm^{-1}$, penetration depth of $80\,microns$), $605.4\,nm$ ($\alpha = 3.3 \times 10^1\,cm^{-1}$, penetration depth of $300\,microns$) and the last one corresponding to the 1S orthoexciton energy ($2.033\,eV$ [33] or $609.83\,nm$). The crystal has an absorption coefficient of around $3 \sim 5\,cm^{-1}$ [34] (penetration depth of $2500\,microns$) at the 1S transition. The dye solution used for an output at $585\,nm$ is $53\,mg/L$ of Rhodamine 590 and $7\,mg/L$ of Rhodamine 610. For the output in the $605 - 610\,nm$ region the solution is: $87\,mg/L$ of Kiton Red 620 and $24\,mg/L$ of Rhodamine 640; both solution are in methanol. The pulse duration is $6\,nsec$ and the peak pulse power is around $3\,MW$. The average power of the laser varies with the wavelength used. Figure 2.5 presents the average power of the laser as a function of the wavelength with the dye used to obtain the wavelengths in the $605 \sim 610\,nm$ region.

The CW Ar^+ gas laser has a multiline output (several wavelengths); the two principal wavelengths are 488.0 and $514.5\,nm$. Its maximum output power (all lines) is around $2.6\,W$ and is only used here to pump the CW dye laser. The CW dye laser has an output wavelength in the visible spectrum; the wavelengths used are the same as with the pulsed dye laser except for $585\,nm$ which is not used in CW. The dye solution is $1\,g/L$ Rhodamine 590 in ethylene glycol. The maximum output power is around $0.5\,W$ which also varies with wavelength (see fig. 2.6).

The average power (P_{avg}), exiting a diaphragm of the same size as the aperture covering the sample, is measured using a calibrated power meter. The intensity for a CW beam is simply the average power divided by the aperture area. The peak intensity I for a pulsed laser is:

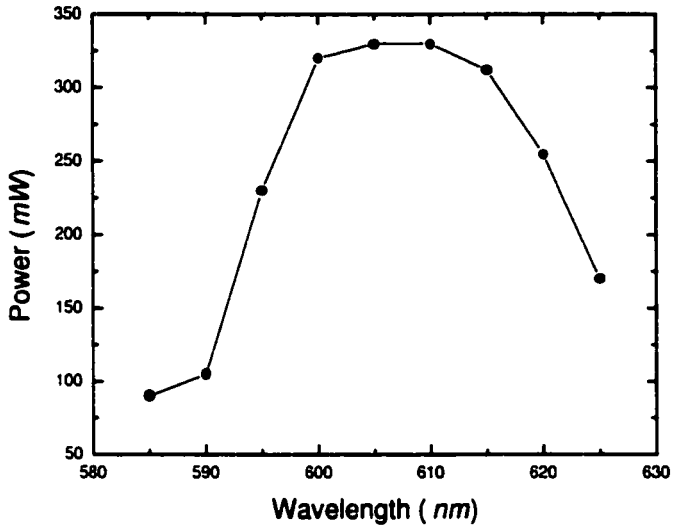

Figure 2.5: Pulsed dye laser power as a function of the wavelength for the dye solution Kiton Red 620 and Rhodamine 640.

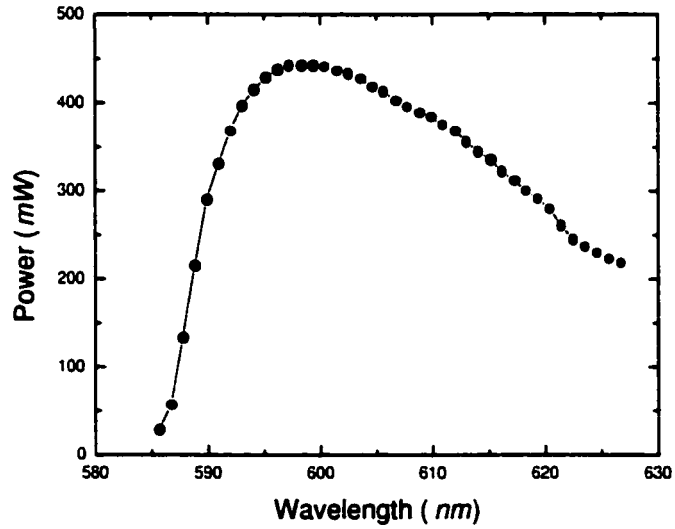

Figure 2.6: CW Dye laser power as a function of the wavelength for the dye solution Rhodamine 590.

$$I = \frac{P_{avg}}{Af\delta t}, \tag{2.2}$$

where A is the illumination area, f is the repetition rate and δt is the pulse duration. For exciton density calculations we make the assumption that the peak intensity of the pulse is the same as that of a square pulse with a duration of δt. This assumption is valid since we only use the center portion of the Gaussian laser beam. The intensity drop over the region of interest is less than 30%.

The density of excitons in the crystal is varied by controlling the intensity of the laser pulses. This is done in either of three ways: with neutral density front surface filters, neutral density volume absorbing filters, and/or a quadruple quartz wedge attenuator. These three methods are used instead of having to change the intensity of the laser at the source which would affect the beam quality, pulse duration, wavelength, etc.

For CW lasers of moderate intensity, front surface filters can be used. Front surface filters consist of a reflective metallic coating on a glass substrate. The high peak power of the pulsed lasers would easily damage these filters; absorbing neutral density filters are used instead. Filters come in different optical densities (0.05, 0.1, 0.2, 0.3, 0.5, 1.0 and 2.0); the relation between attenuation and optical density is given by:

$$I = I_0 \cdot 10^{-OD} \tag{2.3}$$

where I_0 is the incident intensity, OD is the optical density and I is the transmitted intensity. Different attenuations are achieved by stacking multiple filters to gradually reduce the intensity. The disadvantage with the filters is that they slightly deviate the beam; this happens because a wedge is cut between the two faces to reduce etalon effects. Small deviations from the rated optical densities can also arise when stacking multiple filters.

A quadruple quartz wedge attenuator will resolve these problems. This device is based on the Fresnel reflection equation for polarized light. The quartz wedge absorbs a negligible amount of light which is either reflected or transmitted, the transmission being a function of the incident beam angle [35]. The beam deviation produced by the first wedge is canceled by the second; and the beam offset produced is then cancelled by the second pair of two counter-rotating wedges. A computer controlled stepper motor rotates the two pairs of wedges to produce a desired attenuation (highly repeatable and precise, less than $0.05\,OD$). In theory one could calculate the attenuation of the beam as a function of the angle of the plates, but at high attenuation this differs from calculation,

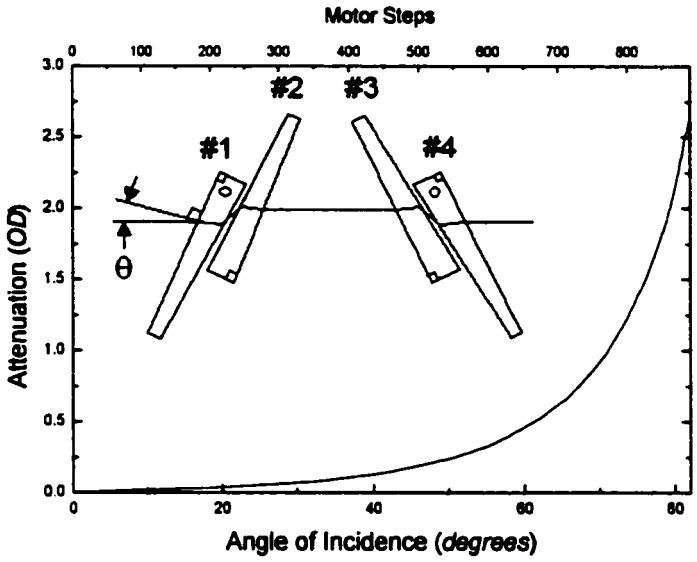

Figure 2.7: Attenuation in optical density as a function of the angle of incidence (motor steps).

due to beam divergence or residual orthogonal polarization. To correct for this one needs to do a calibration; a computer program subroutine is used to calibrate the device by measuring the intensity throughput with a power meter as a function of the stepper motor step angle. To position the stepper motor at a desired attenuation the computer program uses a lookup table (see fig. 2.7 for an example) and uses linear interpolation to find the number of steps corresponding to the desired OD.

Initial alignment of the device is very crucial to achieve high optical densities. The laser beam must be centered on the entrance slit and perpendicular to the first and third wedge's front faces (see inset of fig. 2.7) so that it clears the output slit. Also the two pairs of wedges must be parallel to each other to define the $0\,OD$. This is verified by observing the reflections of the incident beam on the wedges. The best way to do this is to make sure that the reflections will hit a surface far enough away to achieve a good centering, however a few meters should suffice. The first wedge will produce two reflections: one from the front surface, the other from the back surface, separated by 1^o (the wedge angle). The second wedge produces the same reflections since its surfaces are parallel to the surfaces of the first wedge. Again the third and fourth wedges will produce the same reflections if the angle is 0^o. The manufacturer (Newport) intentionally tilted the first pair of wedges by $+1.3^o$ and the second pair by -1.3^o, making the reflections from the first and second pair distinguishable (this tilt does not affect performance of

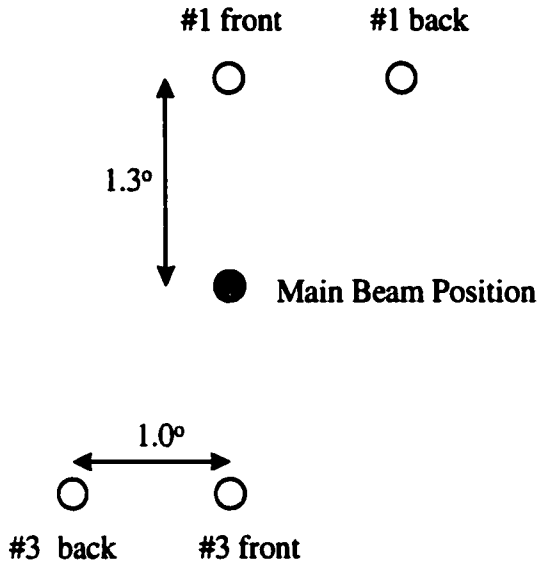

Figure 2.8: Schematic of the reflections produced by the quadruple quartz wedge attenuator. The numbers correspond to the wedges in fig. 2.7; front and back correspond to which face of the wedge the reflection comes from.

the device). If the wedges are perfectly aligned four laser spots should be visible, in the configuration depicted in fig. 2.8.

2.4 Experimental Setup

2.4.1 Optical Cryostat

To reach the temperatures needed for the Bose-Einstein condensation experiments an optical liquid Helium cryostat is used. This optical cryostat enables us to reach temperatures below liquid ^{4}He ($4.2\,K$) and also to illuminate our sample. The cryostat is mounted with four sets of optical windows, each set consists of two vacuum spaced fused quartz plates.

An active cooling/heating system is used to maintain sample temperatures stable over long periods of laser illumination and also to change the samples at low temperatures in a relatively short time.

This system consists of two heaters, a pumping port and a needle valve controlling the liquid He flow in the sample chamber. One of these heaters is situated in the bottom of the cryostat; it affects the sample temperature indirectly by vaporizing liquid He. If the liquid He entering the sample chamber is heated high enough it will vaporize and serve

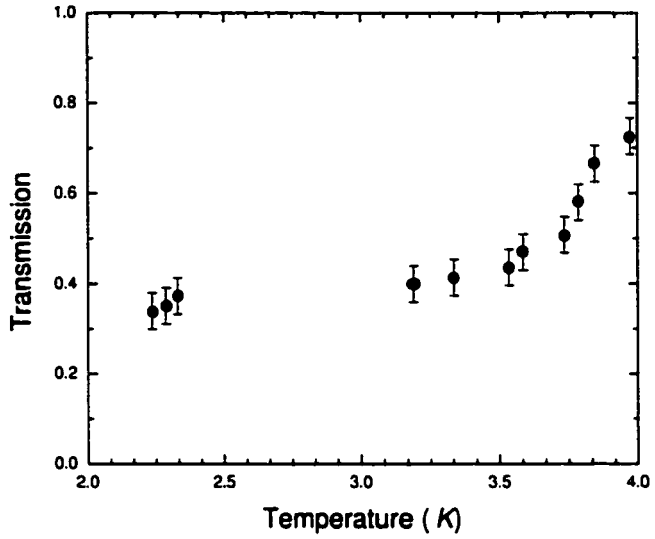

Figure 2.9: Optical transmission through $2.5\,cm$ of liquid He as a function of the liquid temperature.

as a gas thermal bath instead of a liquid bath. The second heater is situated above the sample holder, on the sample rod. This heater directly heats the sample by conduction through the sample rod. The sample rod consist of a $1\,m$ long Invar rod finished on one end with a cylindrical copper block, where the heater is mounted, to which the sample holder is attached. The other end of the sample rod has a cover to form a vacuum seal with feedthroughs for the temperature sensors, electric heater power, sample signal and fiber optics. The pumping port is used to lower the temperature of the He bath; a high pumping rate will produce a high cooling rate. The temperature could be controlled by adjusting the heating rate, the liquid He flow and the pumping rate. The heating rate is controlled by externally changing the current supplied to the two heaters. The liquid He flow is controlled with the needle valve. The pumping rate change is achieved with the use of a computer controlled stepper motor mounted to a valve on the pumping line.

This system permits us to obtain three temperature regimes: superfluid He ($\sim$ 2 to $2.17\,K$), liquid He (2.17 to $4.2\,K$) and gaseous He ($4.2\,K$ and higher). Most of the results were done in the superfluid phase of He with little variation on the temperature, $2\,K$, which is used in the following sections. If results are presented as a function of the temperature, the actual values will be stated.

It is important to note that in the liquid phase of He, bubbles are present in the liquid,

attenuating the laser beams by means of multiple reflections and scattering. Transmission through the liquid He was measured [10]. Results are shown in fig. 2.9. The transmission of He in the superfluid and gas phases is nearly one. The superfluid phase has a high thermal conductivity and it prevents the formation of bubbles.

Two sensors mounted in the cryostat provide the temperature readings. One is mounted on the bottom of the sample chamber and the other on the copper cylinder just above the sample holder. The two sensors are silicon diodes which have a temperature calibrated resistance. A temperature controller sends small electrical pulses to the sensors and determines the resistance. This is then converted to a digital signal by a lookup table and linear interpolation, displayed on the controller.

2.4.2 Data Acquisition

The time resolved measurements are all recorded using a digitizing oscilloscope (Tektronics model 620b) with a maximum sampling rate of $2\,GigaSample/sec$ with $500\,MHz$ bandwidth on two channels and two auxiliary $500\,MegaSample/sec$ channels all operating with $50\,\Omega$ input impedance. The traces are averaged over many laser pulses (~ 100 pulses) to reduce random background noise which in some cases can be as large as the signal itself. The sampling rate used was $500\,MegaSample/sec$ since the oscilloscope could only hold 2000 points per trace and a $4\,\mu sec$ window was usually required. Once a sufficient averaging is done the traces are downloaded from the oscilloscope to a computer via a GPIB interface card. To determine when to trigger the oscilloscope we use an electrical pulse produced by the laser power supply. This signal reaches the oscilloscope through a coaxial cable connected to one of the auxiliary channels. The time zero on the oscilloscope has to be corrected since the laser light reaches the sample about $85\,nsec$ after the electrical pulse, due to a difference in signal and cable length, laser optical path and built-in trigger delay in the laser control module.

Post-processing of the raw data is done with a computer program (TEK) written for this purpose and many others. The post-processing starts off by doing the subtraction of the raw data trace with a parasite trace (see fig. 2.10 for an example of some post-processing steps). This is used to eliminate structures that weren't averaged out. These parasites are acquired in the same experimental conditions as the raw data traces but with the laser beams blocked from reaching the sample. A Savitzky-Golay smoothing filter is applied afterwards to further remove noise on the trace, thus increasing the precision of the analysis. The width of the filter is determined by the width of the main

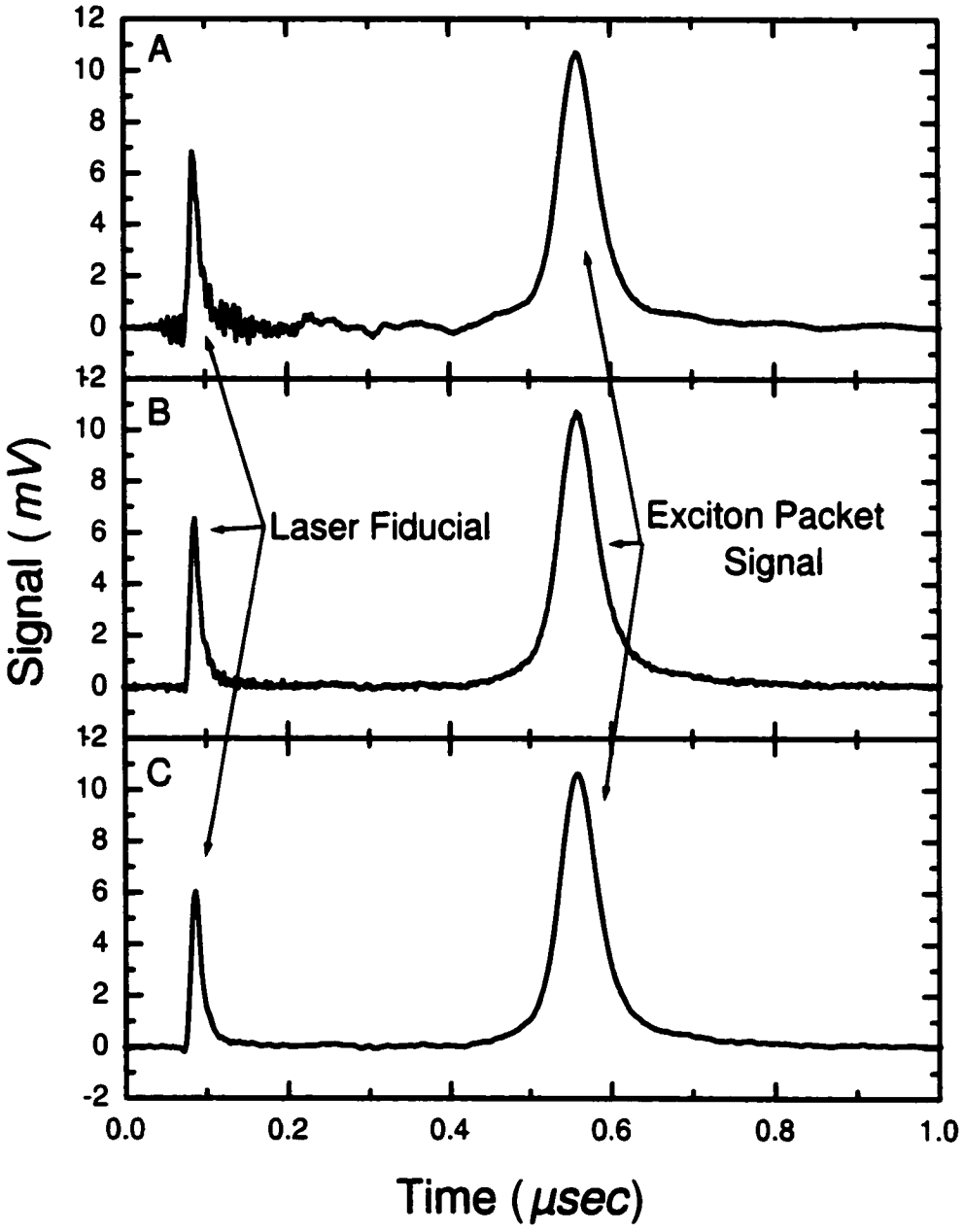

Figure 2.10: Example traces showing the post processing steps. A: Raw Data. B: Raw Data with parasites subtracted. C: Same as B but with a Savitzky-Golay filter applied.

peak and the signal to noise ratio. The larger the width of the filter the more noise will be taken out. The limitations of the filter is that if the width of the filter is too large the signal will be distorted; the peaks will be widened and reduced in amplitude. The last operation done on the traces is to time-shift them to the correct time zero, which corresponds to the laser light hitting the sample. This is done by viewing the fiducial of the laser light on the trace (see fig. 2.10); this fiducial is simply some of the laser light making its way to the detector and producing a signal.

The analysis can now be performed on the processed data. The program TEK now finds the main peak and calculates its amplitude, its arrival time, its width (FWHM), its half width on the leading edge (HWHM). Other characteristics are also extracted from the data, such as: the total integrated signal, the baseline of the signal (dubbed DC level) and a second baseline after the peak if applicable (DC level 2). All these results, including the data converted in ASCII format, are output in files readable by any spreadsheet and graphing program.

The program TEK (coded in Visual Basic by Eric Benson) controls the two stepper motors (quadruple quartz wedge attenuator and pumping valve), calibrates the attenuator (rewritten by the author to accommodate a new power meter), transfers the data from the oscilloscope (raw data and temperature from the sensors), controls the movement of a spectrometer, takes spectra from a lock-in amplifier or the oscilloscope and finally displays and manipulates the data in multiple graphical windows.

2.4.3 Single Pulse Excitation

Most of the experiments are performed using single optical pulses at $10\,Hz$ used to create the exciton gas that will travel through the crystal. Dissociation of the excitons produces the photovoltaic signal which is measured as a function of time and averaged over many laser pulses. This type of experiment is done as function of either laser intensity (exciton density) or sample temperature. Two wavelengths of laser pulses are used: $532\,nm$ and $585\,nm$. The Nd:YAG has an output at $532\,nm$ and is used to pump the pulsed dye laser to produce the $585\,nm$. To switch between the two wavelengths, a beam splitter and a mirror in the pulsed dye laser housing are removed (see fig. 2.11). With the beam splitter and the mirror the output is $585\,nm$, without $532\,nm$.

Figure 2.11 shows a schematic of the single pulse experiments. The laser light (dotted line) is directed to the sample with high reflectivity ($> 99.9\%$) multilayer dielectric mirrors. The laser beams are attenuated with neutral density filters and a quadruple quartz

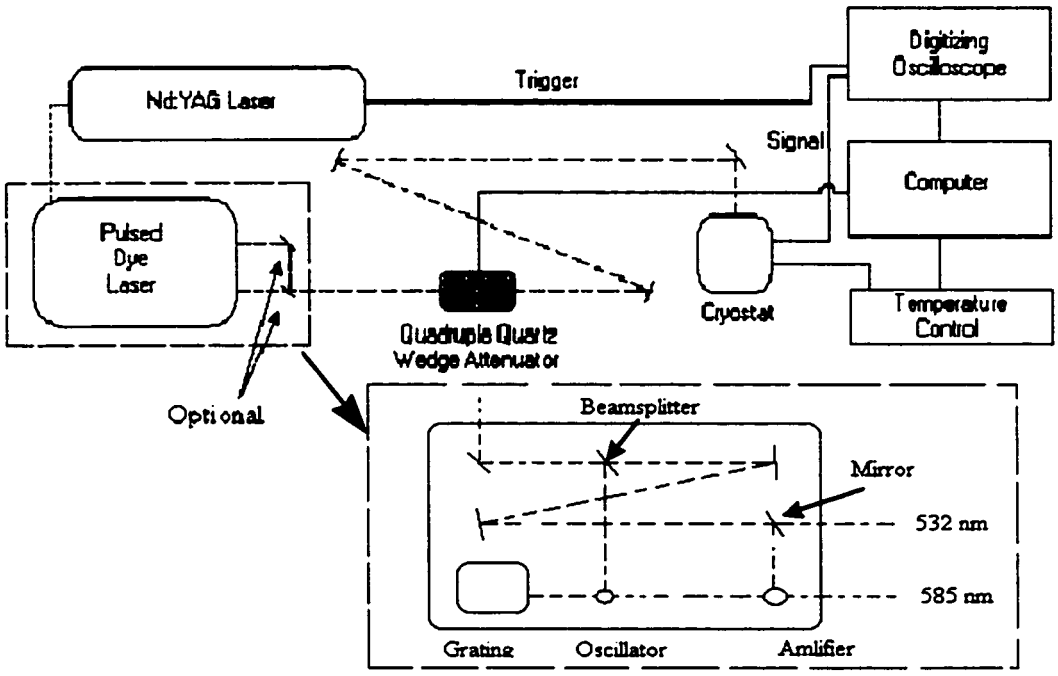

Figure 2.11: Schematic of the experiments for a single pulse illumination. The pulse can either be at $\lambda = 532\,nm$ or $585\,nm$.

wedge attenuator (as mentioned in sec. 2.3). The neutral density filters are positioned as close to the cryostat as possible; this is to minimize beam deviation. The illumination geometry was shown on fig. 2.2.

The solid lines in fig. 2.11 represent the electrical cables between the different instruments. The signal cable is triply shielded; this helps to remove high frequency electrical ringing produced by the Pockels cell (within the high voltage power supply for the laser flashlamp). The ringing is further removed by using aluminum foil covering the top of the cryostat and the sample rod. Some noise can still be visible after all these precautions. To further remove the noise the temperature sensor has to be disconnected (it is not shielded against high frequencies), this has no effect if measurements at constant temperature need to be done since we can measure the temperature before disconnecting it. If measurements are to be done as a function of the temperature the sensor has to be connected, introducing noise on the traces.

2.4.4 Double Pulse Excitation

Double pulse excitation is used to observe the interference phenomenon between two coherent exciton condensates.

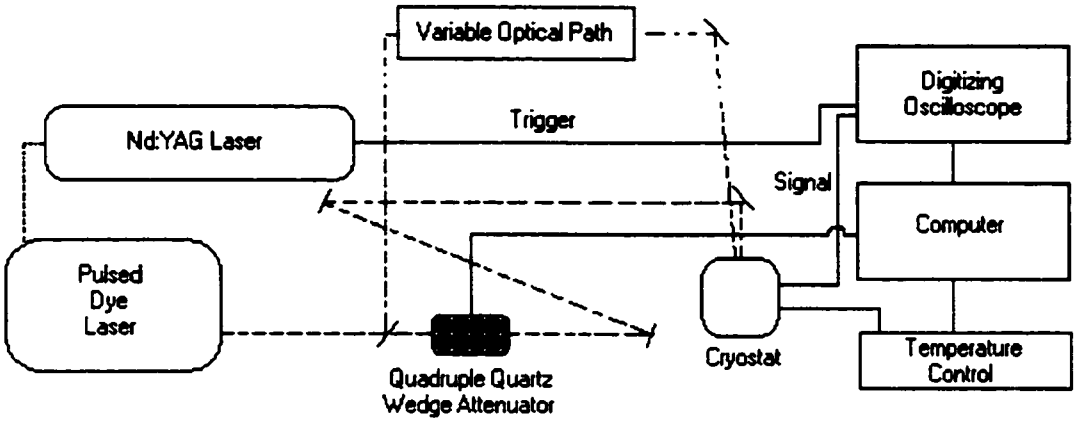

Figure 2.12: Schematic of the experiments for a double pulse collinear illumination. The pulse can either be at $\lambda = 532\,nm$ or $585\,nm$.

Longitudinal Separation

The first type of interference observed is longitudinal interference. This occurs when two exciton packets are traveling on the same axis but are separated in time, thus in space. Figure 2.12 is the schematic representing these experiments. The pulses are separated in two using a 50%/50% beam splitter. One of the beams continues to the sample the same way as in the single pulse experiment. The second beam is reflected back and forth between mirrors to produce an optical path difference with the first. This introduces a delay (δt) between the two pulses given by:

$$\delta t = \frac{Path\ Difference}{c}. \tag{2.4}$$

The delayed pulse will hit the sample surface with a small angle of incidence ($\sim 3°$), to avoid the last mirror directing the first beam to the cryostat; this small angle had no effect on the experiment. A lens is needed to refocus the beam to its original size and intensity: beam divergence expands the beam and reduces intensity; as well the $25\,mm$ mirrors used to create the optical path difference only reflected part of the laser beam.

The intensity of each beam can be controlled independently with the use of neutral density filters. The intensity of the delayed beam was readjusted for each delay using its photovoltaic signal and equalizing it to the one of the main beam. The main beam intensity did not vary and was known at all time.

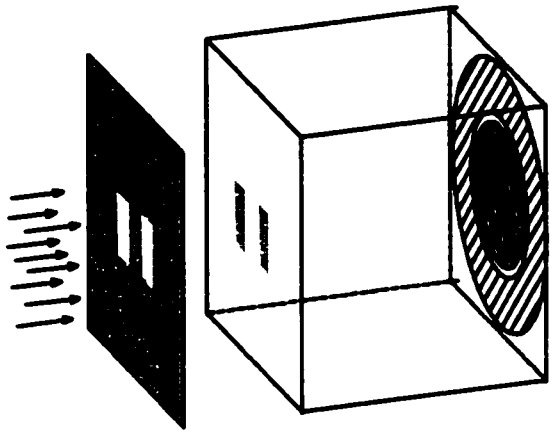

Figure 2.13: Illumination geometry for the lateral interference experiments.

Lateral Separation

The lateral interference between two exciton packets is observed using the same setup as for single pulse excitation. The difference is that slits are positioned in front of the cryostat to produce two independent exciton packets separated by the slit separation. Figure 2.13 gives a representation of the illumination geometry.

Razor blades mounted on a translation stage are used to block a desired slit. The two razor blades are separated by a distance slightly larger than that of the slit itself allowing an illumination of both or one slit. Aligning the beam to have equal intensity in the two slits proved to be a difficult task. By blocking one of the slits, we could see the photosignal given by the other slit. Then when switching to block the other slit, it could be aligned so that the photosignal was of the same amplitude. This changed the alignment of the first slit; so trial and error was used until both photosignals from each slits were of equal amplitude.

2.4.5 Single Pulse + CW Excitation

This section deals with a variation of the double pulse illumination experiments. The difference is that a CW laser beam illuminates the sample on one of its sides, perpendicular to the main beam (see the experimental setup on fig. 2.14 and fig. 2.15). The CW is tuned at the 1S orthoexciton energy ($2.0329\,eV$ or $609.86\,nm$). It is used to create "cold" excitons in the path of the main exciton cloud. The exciton cloud can be created with either the Nd:YAG pulse ($532\,nm$) or the pulsed dye laser tuned at $585\,nm$. Since the side laser beam is tuned to a weakly absorbed wavelength, it easily scatters inside the

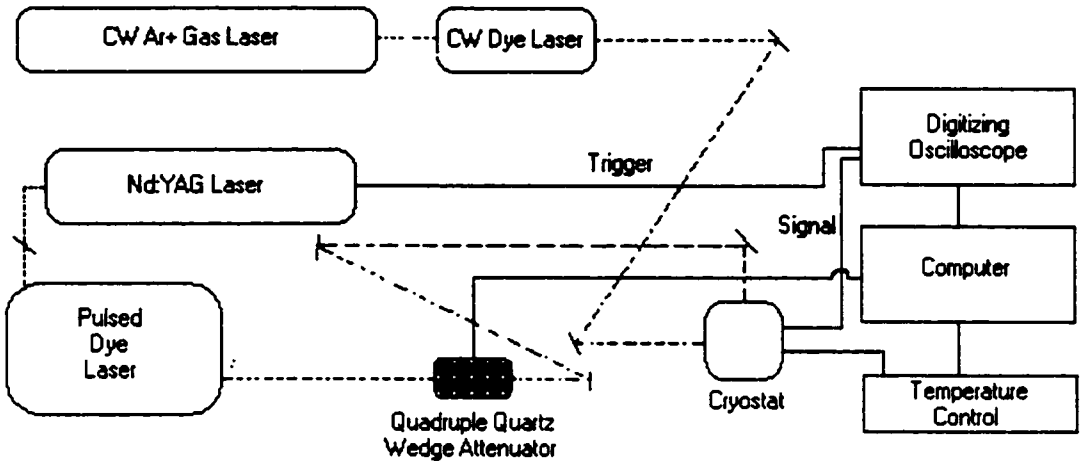

Figure 2.14: Schematic of the experiments for a single pulse illumination with an orthogonal CW illumination. The pulse can either be at $\lambda = 532\,nm$ or $585\,nm$.

crystal due to impurities and lattice defects and elevates the baseline of all the traces.

These excitons are dubbed "cold" because they are created with little excess energy compared to the paraexciton energy. These "cold" excitons will quickly convert down to the paraexciton ground state ($\tau \sim 3$ to $30\,nsec$). They are used to trigger stimulated particle emission in the exciton condensate.

2.4.6 Nd:YAG + Pulsed Excitation

The simultaneous Nd:YAG and pulsed illumination is done to further understand the stimulated emission phenomenon observable with the setup described in sec. 2.4.5. Instead of using a CW laser to create the "cold" excitons, a pulsed beam is used to control the time of injection of these "cold" excitons (see fig. 2.15 and 2.16). A problem with this setup is that it can only be used with the main beam at $532\,nm$; the $585\,nm$ pulses were emitted by the dye laser which is used at $609.86\,nm$ to create the "cold" excitons. The stimulated emission of particles in the condensate can thus only be studied here using exciton clouds created with the $532\,nm$ laser pulses.

The variable optical path difference was obtained using two different techniques. The first technique is to make the laser pulses go back and forth between sets of mirrors (as in sec. 2.4.4). The second method is to focus the laser beam into an optical fiber with a known length. The optical fiber used is 0.39-NA $200\,\mu m$ core 3M TECS hard clad multimode fiber. The length of the fiber was varied depending on the desired delay between the main and the lateral pulse. The diverging laser beam coming out of the fiber

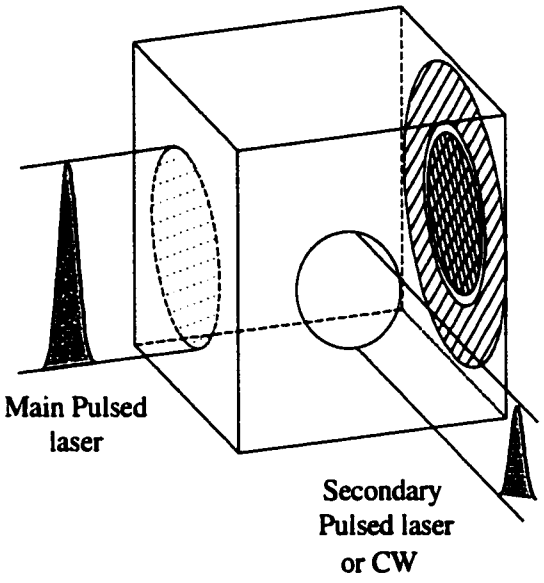

Figure 2.15: Illumination geometry showing the main laser pulse position and the secondary laser illumination.

was then brought back to a parallel beam using an aspheric lens. The delay is calculated using the following formula:

$$\delta t = \frac{fiber\ length \cdot\ core\ index\ of\ refraction}{c}, \tag{2.5}$$

where the core's index of refraction is equal here to 1.457. This method permits us to go at higher intensity and longer delays than with mirrors, attenuation in the fiber is much less then the losses on the mirrors mentioned in sec. 2.4.4.

A second optical fiber is used to collect the transmitted light of the lateral beam through the crystal. One end of the fiber is positioned on the crystal surface in the cryostat. The other end comes out of the cryostat through the cover of the sample rod. The end is then connected to a fast detector (New Focus nanosecond photodetector #1621) itself connected to the digitizing oscilloscope.

This setup permits us to vary the injection time of the "cold" excitons relatively to the position of the traveling exciton cloud in the crystal. Also, we can measure the effect of the exciton cloud on the lateral beam by examining the transmitted fraction.

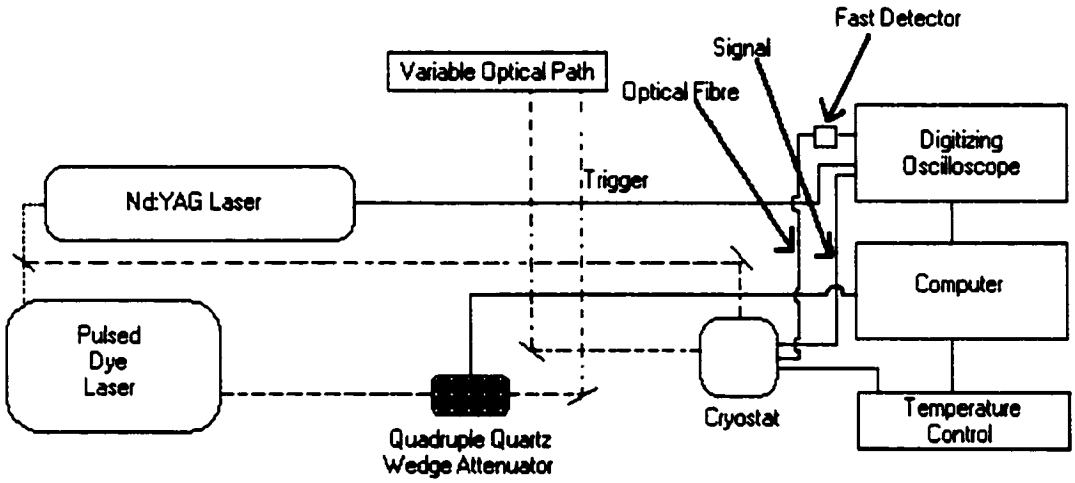

Figure 2.16: Schematic of the experiments for a single Nd:YAG pulse illumination with an orthogonal pulse illumination.

Results and Analysis

The following two chapters deal with the experimental results concerning the formation of the exciton packets (chapter 3) and the stimulated emission phenomenon (chapter 4).

The goal of the experiments is to better understand the initial formation of the exciton packet (condensed or not). By using two different excitation wavelengths to create the exciton cloud we can vary where the cloud is created (the two laser wavelengths having two different penetration depths). The basic properties of the exciton cloud are studied in chapter 3. The interference phenomenon is also studied in that chapter as a function of the illumination wavelength.

Stimulated emission of particles into the condensate is a phenomenon not fully understood and more experiments were needed to grasp the concept specific to the condensation of excitons. New experimental techniques provide new clues to solve the puzzle of amplification by stimulated emission.

Each experimental result will be accompanied by a discussion and/or an analysis which will try to explain them using the Bose-Einstein condensation phenomenon.

Note that as the experiments progressed the crystal got damaged (small crater on the front illumination surface) and this affected the observed excitonic signal, i.e. at the same laser intensity the excitonic signal amplitude diminished in the last experiments.

Chapter 3

Exciton Packets Initial Conditions

This chapter will make a comparison between two experimental conditions under which the exciton packets are created; this is useful in the sense that it can provide information on the formation of the exciton packet. The difference between the two conditions is that the excitation region (where the initial exciton cloud is created) is different in size and phonon population. This difference is achieved by using two laser excitation wavelengths (the excitons are optically created) having different absorption coefficients (α), hence different penetration depths. The two laser wavelengths used are $\lambda = 532\,nm$ and $585\,nm$. Their respective penetration depths are $3\,\mu m$ and $80\,\mu m$ ($\alpha = 3 \times 10^3\,cm^{-1}$ and $\alpha = 1.25 \times 10^2\,cm^{-1}$) with excess energies of $0.310\,eV$ and $0.098\,eV$ available for phonon creation.

3.1 Single Pulse Illumination

This section deals with experimental results in single pulse geometry as described in sec. 2.4.3. Comparisons are made by analyzing the basic properties of the exciton packets under the two conditions of formation, this at different initial conditions: exciton density and temperature. The basic properties are: amplitude of excitonic signal, velocity of the exciton packet, integrated signal of the exciton packet and packet size (given by the half width at half maximum times 2 (HWHM x 2)). Also a phase diagram of the exciton packet is made using an illumination wavelength of $585\,nm$ to compare it with prior results obtained at $532\,nm$. [10].

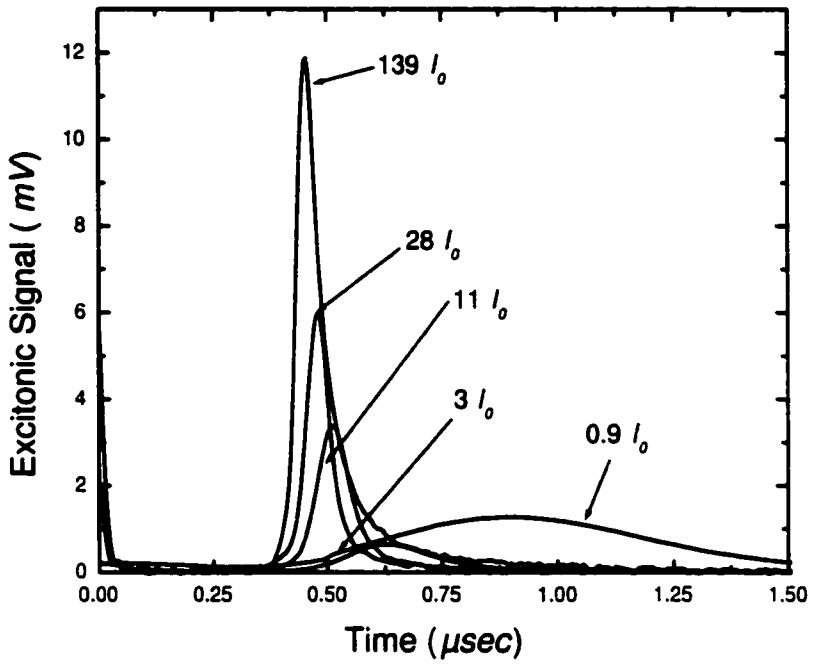

Figure 3.1: Experimental results for an excitation wavelength at $532\,nm$ at various laser intensities at $T = 2\,K$. Note that $I_0 = 10^5\,W/cm^2$ and that the trace at $0.9\,I_0$ is multiplied by a factor of 10 to make it visible.

3.1.1 Variation of exciton cloud initial density

The initial cloud density is varied by changing the intensity of the laser beam (also by changing λ) used to optically create the excitons. The results (all done at a temperature of $2\,K$) will mostly be plotted as a function of the intensity of the laser beams in units of I_0 ($I_0 = 10^5\,W/cm^2$).

Figures 3.1 and 3.2 show experimental results for an excitation wavelength at $\lambda = 532\,nm$ and $\lambda = 585\,nm$. We can see on the graphs remnants of the optical trigger at $t = 0\,\mu sec$. If we take for example the trace at $139\,I_0$ on fig. 3.1 we see a sharp peak at around $0.5\,\mu sec$ which corresponds to the exciton flux detected by our photovoltaic detector. As the intensity of the laser beam is increased (equivalent to an increase in exciton density) we can see a large increase in the photosignal (dubbed excitonic signal) of the exciton cloud. All of the exciton clouds can be fitted using three soliton equations (eq. 1.27); an example is shown in fig. 3.3. The reason why three equations are used is

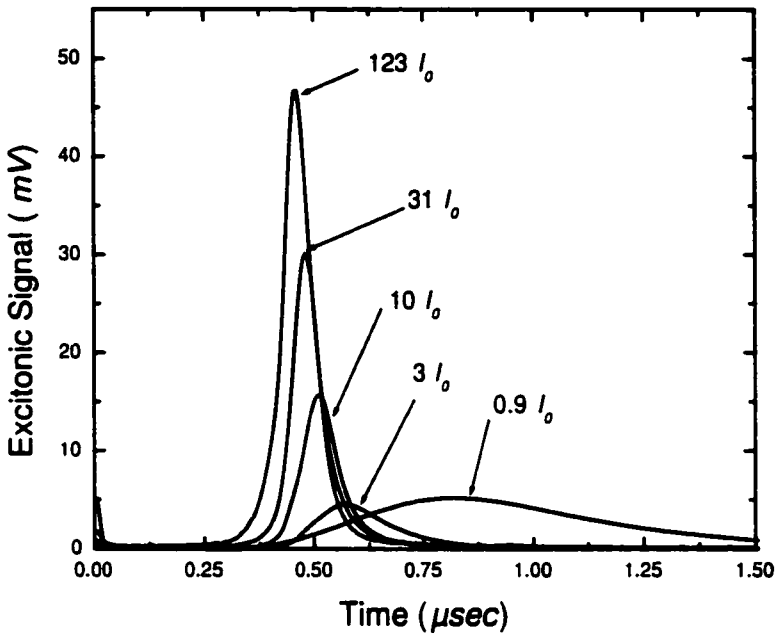

Figure 3.2: Experimental results for an excitation wavelength at $585\,nm$ at various laser intensities at $T = 2\,K$. Note that $I_0 = 10^5\,W/cm^2$ and that the trace at $0.9\,I_0$ is multiplied by a factor of 10 to make it visible.

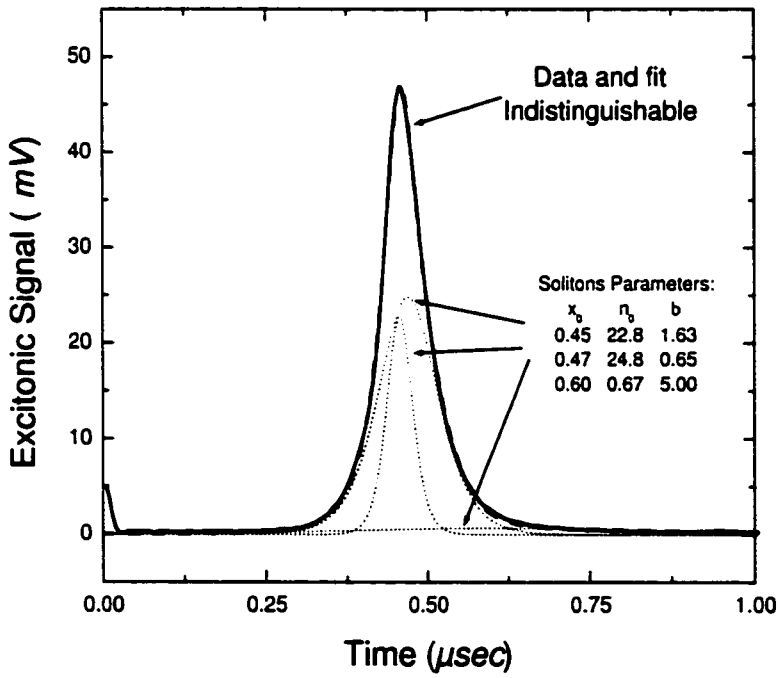

Figure 3.3: Fit of a trace taken under illumination at $\lambda = 585\,nm$ with an intensity of $123\,I_0$. Note that the fit and the data traces are indistinguishable from each other. The fit consists of the sum of three soliton equations with different parameters.

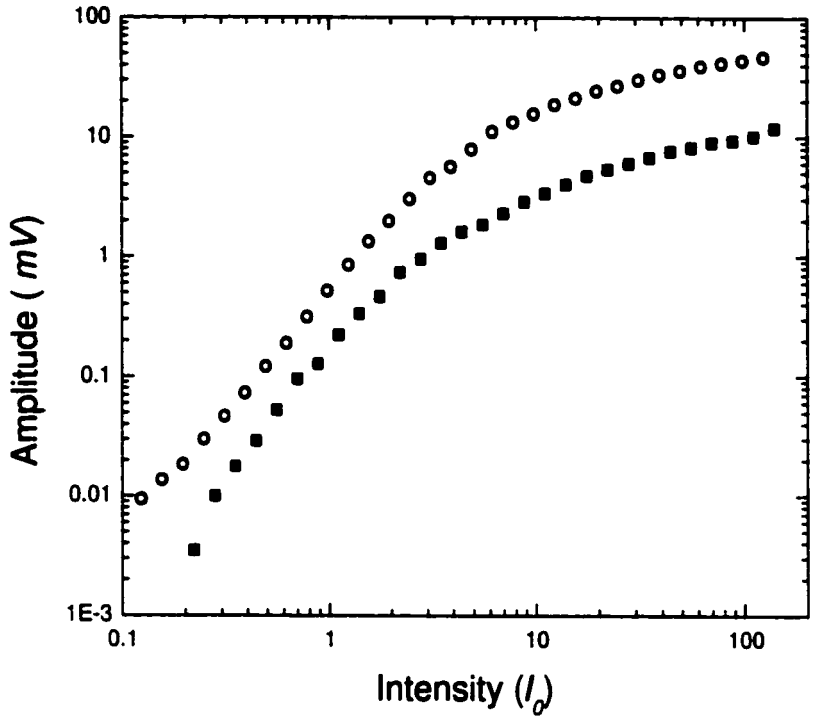

Figure 3.4: Amplitude of the exciton packet as a function of the laser intensity at $T = 2\,K$. Squares correspond to an excitation wavelength of $\lambda = 532\,nm$ and circles to an excitation wavelength of $\lambda = 585\,nm$.

that the exciton cloud is thought to have three components (analogous to a comet): a core, a coma (surrounds the core) and a tail. This will be discussed in sec 3.2.1 and 4.1.

The amplitude of the photosignal of the exciton cloud (fig. 3.4) varies over 5 orders of magnitude. This is due to the exciton cloud going from a diffusive to a ballistic packet and that the number of excitons increases. We see that the amplitude of the packets created with a laser at a wavelength of $585\,nm$ are on average $\sim 3-4$ higher than those created with a laser tuned at $532\,nm$ at the same intensity, and that for all the range of intensities (note that at the same intensity the packets created at $\lambda = 585\,nm$ have a smaller initial density than at $532\,nm$). This is partially due to different phonon populations. In the case of the laser tuned at $585\,nm$ fewer phonons are created. Also, the surface recombination is higher at $\lambda = 532\,nm$, since they are created closer to the surface. They also have a different density gradient and a more violent initial expansion probably influencing the final packet.

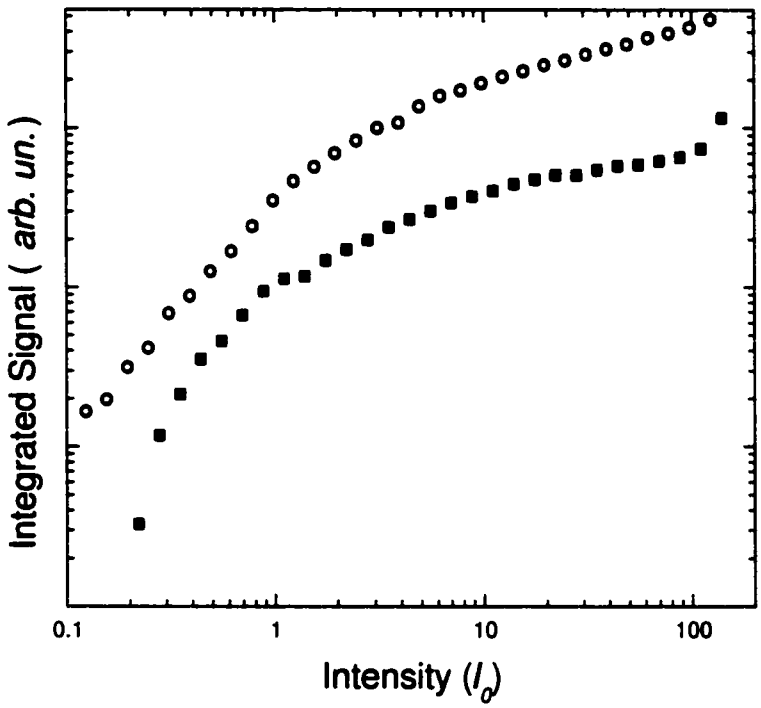

Figure 3.5: Integrated signal of the exciton packet as a function of the laser intensity at $T = 2\,K$. Squares correspond to an excitation wavelength of $\lambda = 532\,nm$ and circles to an excitation wavelength of $\lambda = 585\,nm$.

The total integrated signal (area under the curve) of the photosignal (fig. 3.5) follows the same trend as that of the amplitude of the packet (this is a measure analogous to the number of excitons in the detected packet). The only difference is that the factor between the two curves ranges from to 2 to 10. More excitons are left "behind" the packet at $\lambda = 532\,nm$ since we create the same number when we illuminate at the same laser intensity.

The next two properties of the exciton cloud are the most important because they tell us whether the exciton cloud is diffusive or condensed (ballistic). If we look at fig. 3.6, we see the normalized velocity of the exciton packet. The velocity of the packet is normalized with the velocity of sound in the crystal ($v_s = 4.5 \times 10^5\,cm/sec$). This graph contains a wealth of information. First we notice that there is no evident difference between the two different conditions of illumination, except at low intensities. The packets created with $\lambda = 585\,nm$ at low intensity have a velocity that levels off at around 32% of the

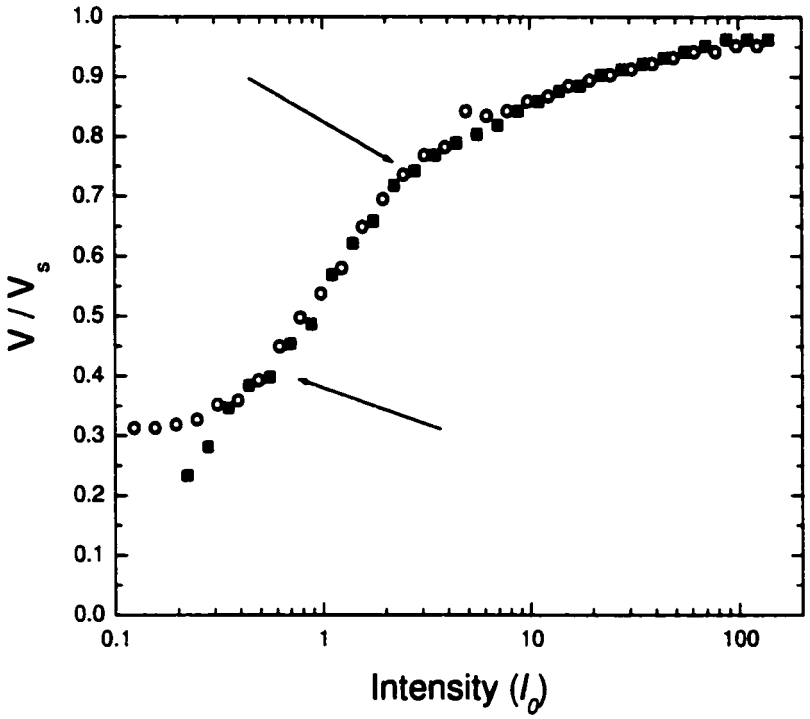

Figure 3.6: Normalized velocity of the exciton packet as a function of the laser intensity at $T = 2\,K$. Squares correspond to an excitation wavelength of $\lambda = 532\,nm$ and circles to an excitation wavelength of $\lambda = 585\,nm$.

sound velocity; compared to the illumination at $532\,nm$ which does not; it will probably level off at intensities lower than these. In both illumination schemes the exciton clouds at high intensities tend to saturate at a value around 96 % of the sound velocity.

The other important feature about this graph is the appearance of two inflection points (marked with arrows on the graph). Inflexion points in the properties of the exciton clouds mark changes in the physical nature of the exciton cloud (going from diffusive to ballistic). The first inflexion point ($\sim 0.5 - 0.6\,I_0$) corresponds to the intensity where the exciton packet reaches the condensed phase, but does not stay condensed for all of the transit time (time for the packet to travel from one face to the other of the crystal). The second inflexion point ($\sim 2 - 3\,I_0$) corresponds to a packet now condensed for all of the transit time. From the first inflexion point intensity we can get the initial exciton density giving condensation; this will be used when comparing the experimental critical density and the theoretical critical density. We note here that the critical (initial) density in the

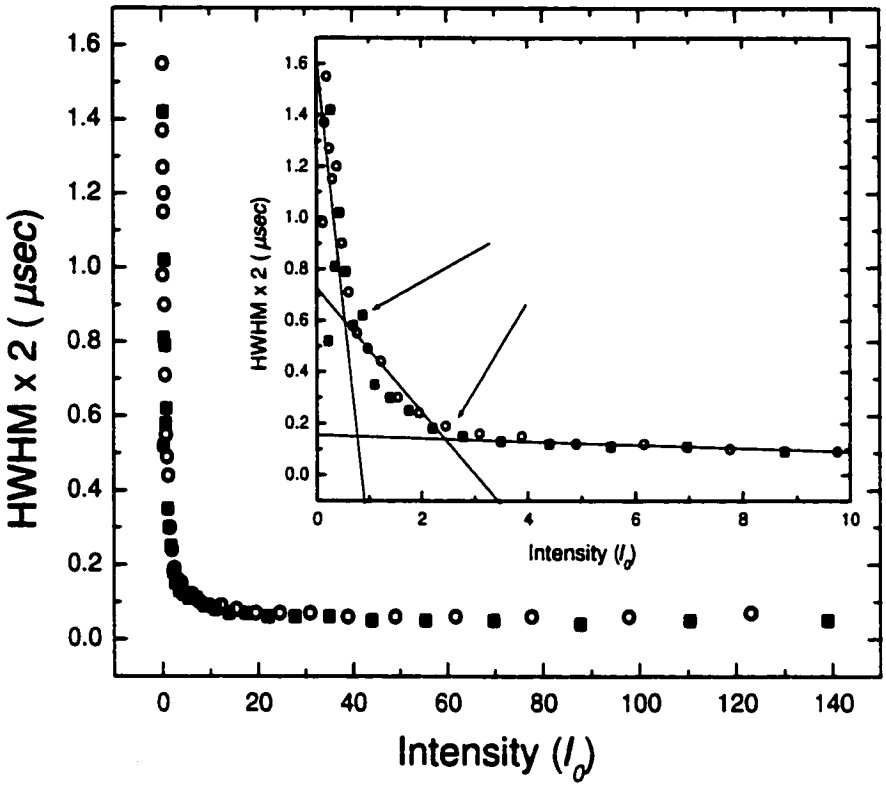

Figure 3.7: Half width at half maximum of the leading edge of the exciton packet as a function of the laser intensity at $T = 2\,K$. Squares correspond to an excitation wavelength of $\lambda = 532\,nm$ and circles to an excitation wavelength of $\lambda = 585\,nm$.

two illumination conditions is different; they have the same critical intensity but since $\lambda = 585\,nm$ has a larger penetration depth the initial density is smaller than $\lambda = 532\,nm$. The theoretical critical density is the same in both cases so why the difference? The higher phonon population and surface recombination in the $\lambda = 532\,nm$ case lowers the initial density of the exciton cloud or maybe the excitons are just left behind the packet, probably reducing the density to that of the $585\,nm$ case.

Figure 3.7 shows the HWHM x 2 on the leading edge of the photosignal of the exciton cloud as a function of the intensity of the laser beam used to create the exciton cloud. The leading edge is chosen here because the photosignal of the exciton cloud is not symmetric (to be explained later on). There is no significant difference between the two illumination wavelengths in this property of the exciton clouds. The cloud width goes to infinity if

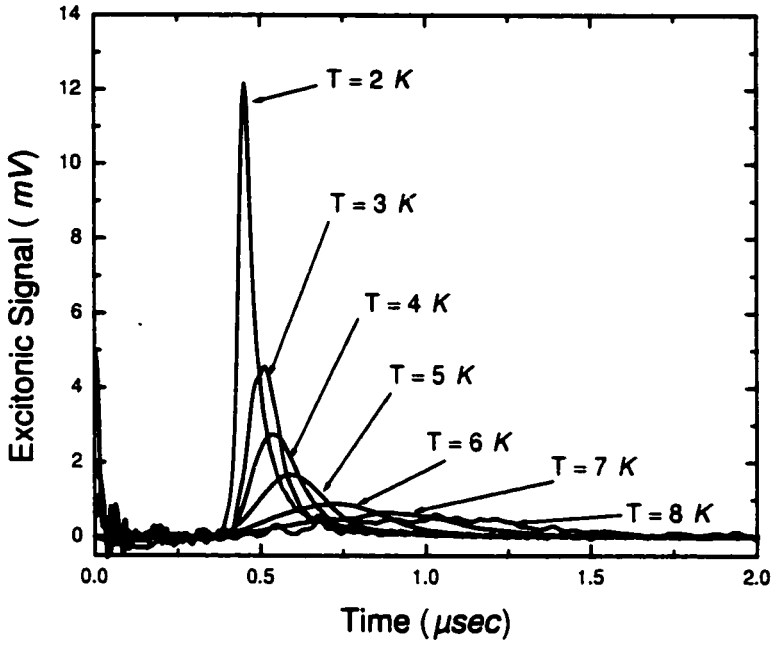

Figure 3.8: Experimental traces for an excitation wavelength at $532\,nm$ as a function of sample temperature at an intensity of $139\,I_0$.

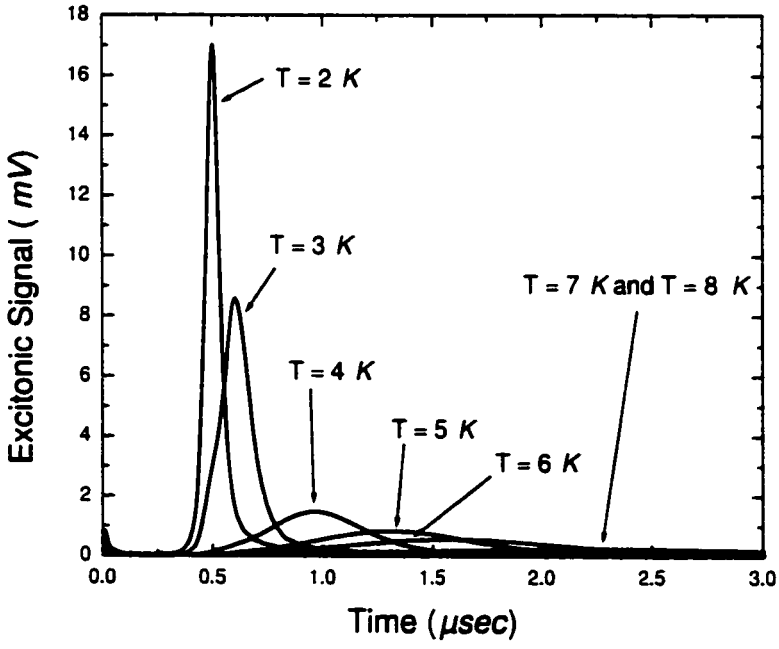

Figure 3.9: Experimental traces for an excitation wavelength at $585\,nm$ as a function of sample temperature at an intensity of $8\,I_0$.

the intensity goes to zero; at low intensity (low density) the cloud is diffusive, so the lower the density the more the cloud spreads during travel. At high laser intensities the half width of the packet saturates to $\sim 0.1\,\mu sec$; when a packet is condensed only the amplitude and the velocity change (the latter only slightly because it also saturates, see prior paragraphs).

In the inset of fig. 3.7, we can see a zoomed version of the graph. The arrows point to two inflexion points in the curve. These inflexion points correspond to those in fig. 3.6.

The next section deals with the same type of analysis on the exciton cloud but as function of sample temperature instead of incident intensity.

3.1.2 Variation of bath temperature

Experimental results showing the exciton clouds as the temperature is varied are presented in fig. 3.8 and fig. 3.9. These results are for illumination wavelengths of $532\,nm$ and $585\,nm$, and fixed intensities of $139\,I_0$ and $8\,I_0$. Note that for the results taken at temperatures higher than $4.2\,K$ (liquid He temperature) the repetition rate of the laser had to be lowered to $1\,Hz$ instead of $10\,Hz$ to prevent temperature instability. The intensity of the pulses is corrected for the scattering of light by the bubbles in the liquid He in the range of $2.17 - 4.2\,K$ (see fig. 2.9 for transmission through He). These results are similar to the ones when the intensity of the laser beam used to create the exciton cloud is varied for fixed T; experimentally an increase in temperature is equivalent to a decrease in laser intensity as expected from eq. 1.14. The following results deal with the properties of the exciton clouds as in sec. 3.1.1, the difference is that the intensities for the two types of illumination are different: $139\,I_0$ for $532\,nm$ and $8\,I_0$ for $585\,nm$. The initial exciton cloud densities are $1.0425 \times 10^{21}\,cm^{-3}$ and $1.875 \times 10^{18}\,cm^{-3}$ respectively. The results will be mostly compared on a qualitative basis.

The amplitude of the exciton packet as a function of the sample temperature is presented in fig. 3.10. Again we see that the results for the illumination at $585\,nm$ produces a signal of higher amplitude at low temperatures (where the exciton cloud has more chances of being condensed) and generally $>$ than for $532\,nm$, even though the intensity is $\sim$ 17x less. At higher temperatures both illumination types give rise to the same exciton cloud amplitude. We also note two inflexion points around $2.5\,K$ and $5\,K$ denoted by the arrows; these inflexion points will be discussed in the next paragraph.

The integrated signal (fig. 3.11) again follows the same trend as that of the amplitude of the exciton cloud. The temperature where the two curves merge is different than in the

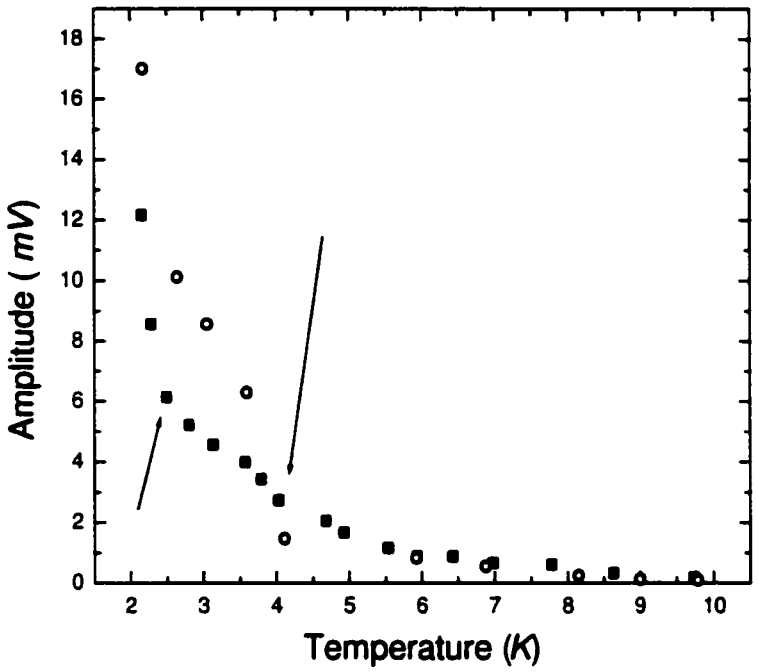

Figure 3.10: Amplitude of the exciton packet as a function of sample temperature at an intensity of $139\,I_0$ for $532\,nm$ and at $8\,I_0$ for $585\,nm$. Squares correspond to an excitation wavelength of $\lambda = 532\,nm$ and circles to an excitation wavelength of $\lambda = 585\,nm$.

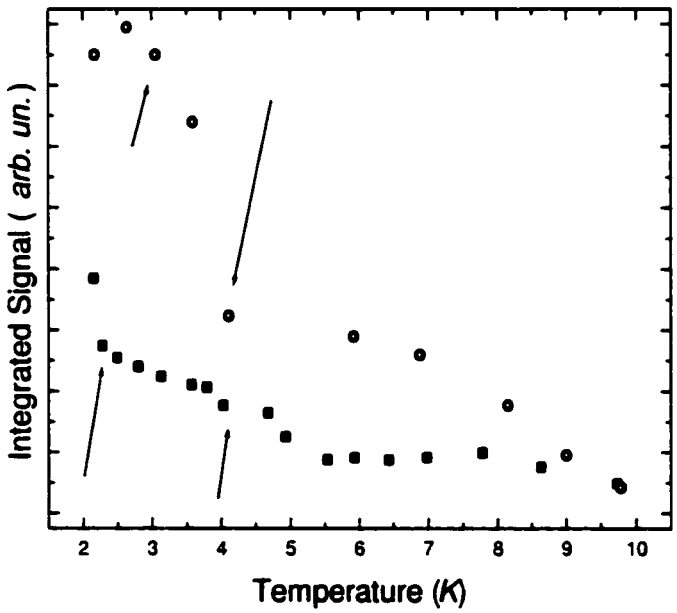

Figure 3.11: Integrated signal of the exciton packet as a function of sample temperature for an intensity of $139\,I_0$ for $532\,nm$ and $8\,I_0$ for $585\,nm$. Squares correspond to an excitation wavelength of $\lambda = 532\,nm$ and circles to an excitation wavelength of $\lambda = 585\,nm$.

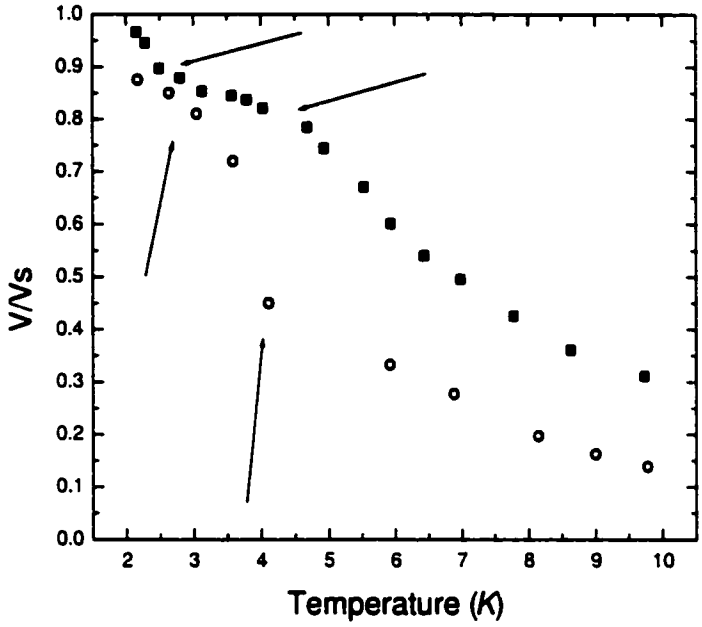

Figure 3.12: Normalized velocity of the exciton packet as a function sample temperature for an intensity of $139\,I_0$ for $532\,nm$ and $8\,I_0$ for $585\,nm$. Squares correspond to an excitation wavelength of $\lambda = 532\,nm$ and circles to an excitation wavelength of $\lambda = 585\,nm$.

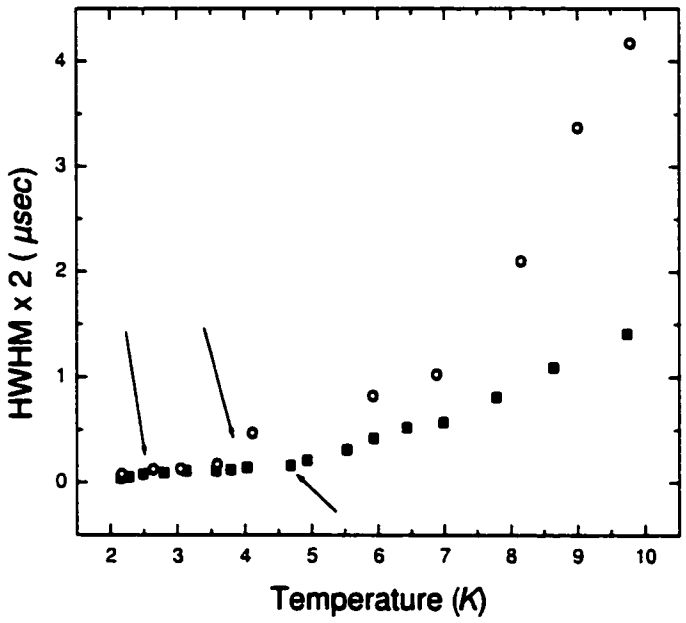

Figure 3.13: Half width at half maximum of the leading edge of the exciton packet as a function of sample temperature for an intensity of $139\,I_0$ for $532\,nm$ and $8\,I_0$ for $585\,nm$. Squares correspond to an excitation wavelength of $\lambda = 532\,nm$ and circles to an excitation wavelength of $\lambda = 585\,nm$.

case for the amplitude (it is now at a higher temperature); this remains unexplained. We also have to note the in fig. 3.10 and 3.11 two inflexion points can be seen on each graph. One around $5\,K$ and the other around $9\,K$. These inflexion points perhaps give the two critical temperatures for condensation. The highest critical temperature is analogous to the first critical intensity in the previous section: it is thought to correspond to when the packet is condensed but not for all the transit time. The lowest critical temperature would correspond to a condensed packet for all the transit time.

The normalized velocity of the exciton cloud (fig. 3.12) is different for both illumination types when the temperature is varied, as compared to when the intensity is varied (see fig. 3.6 for comparison). Both curves have the same shape but in the $585\,nm$ case the packet is slower, probably due to the difference in intensity. The arrows point to the inflexion points in the curves corresponding to the change in physical phase mentioned in the previous section. The two graphs have different critical points: the first one at $\sim 2.5 - 3\,K$ and $\sim 2 - 2.5\,K$, the second at $\sim 4 - 4.5\,K$ and $\sim 3 - 3.5\,K$ respectively for an illumination at $532\,nm$ and $585\,nm$. Phonons more numerous at an illumination at $532\,nm$, may thus play a role in the discrepancy between the two illumination types.

Figure 3.13 shows the HWHM x 2. Again, at low temperatures, both illumination types give rise to a signal of equal width; at higher temperatures they diverge from each other. This divergence occurs at the second inflexion point. The first inflexion points are hard to pinpoint due to the lack of precision (more data is needed in that region). The first inflexion point seems to be the same for both illumination types has compared to the second inflexion point which is different.

Phase diagram

Bose-Einstein condensation only occurs in our system if the density is high enough; eq. 1.14 gives the density needed for this change of phase. Under the critical density the packets are diffusive, over they are ballistic. The critical intensity is needed to calculate the final density of the packet. To find this intensity we use the HWHM x 2 at a fixed temperature. The second inflexion point in the HWHM x 2 vs intensity is used as the critical intensity for condensation (see for instance fig. 3.7). To build the phase diagram, this critical intensity is found for several sample temperatures.

Figure 3.14 shows the phase diagrams for an illumination wavelength of $585\,nm$. The top graph shows the critical intensity needed for condensation as a function of the sample temperature. This data is fitted to the following equation:

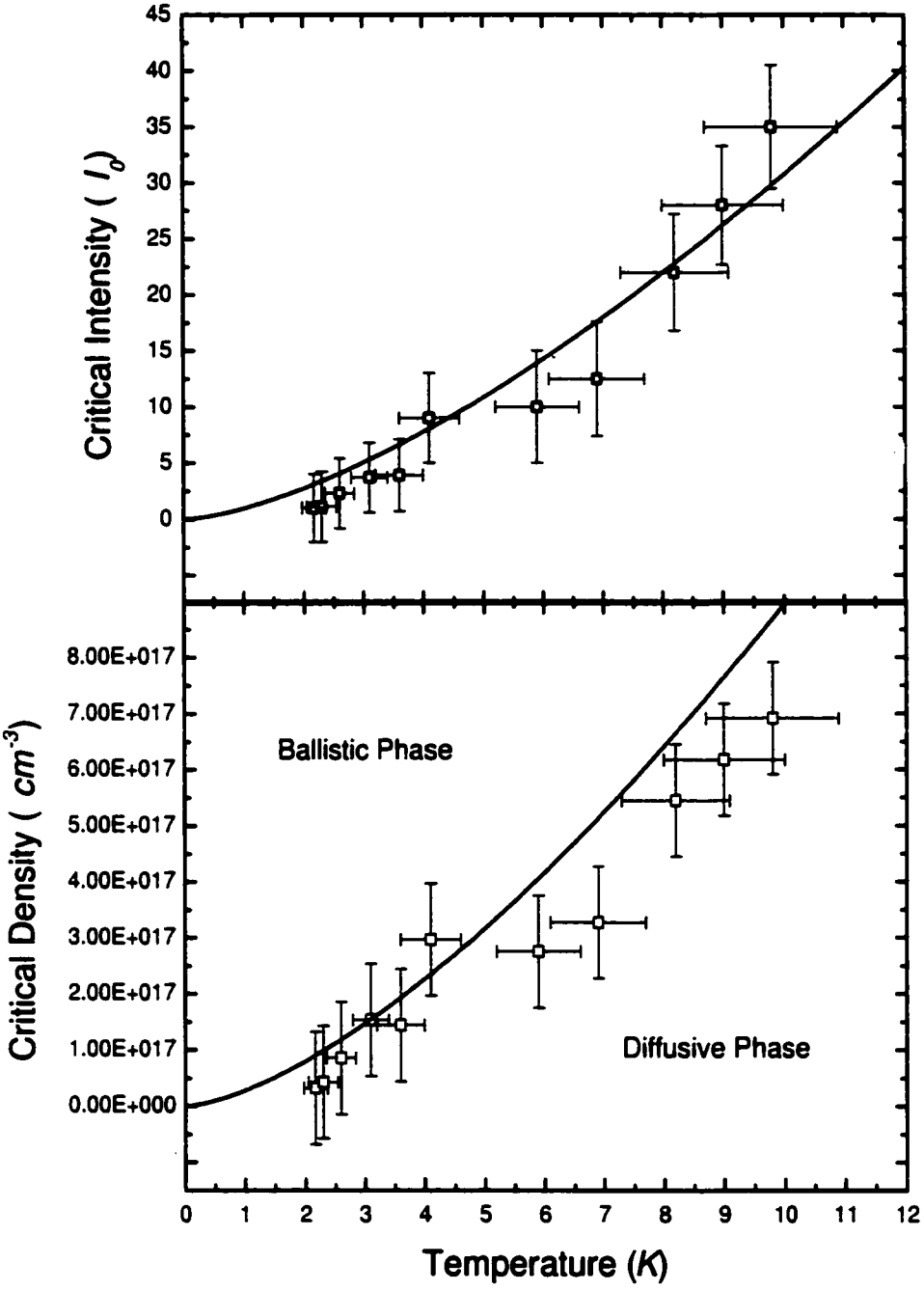

Figure 3.14: Critical intensity (top graph) and Critical density (bottom graph) of the exciton packet as a function of the sample temperature for an illumination wavelength of $585\,nm$. The fit in the top graph is the best fit of $y = cst \cdot T^{3/2}$. The curve in the bottom graph is the theoretical value of the critical density.

$$I_c = constant \cdot T^{3/2}. \tag{3.1}$$

The mean square fit gave a constant of 0.97. This critical intensity can be converted to critical density with the following equation:

$$n_c = \frac{I_c \cdot \delta t}{v \cdot (HWHM \times 2) \cdot (3.2 \times 10^{-19})}, \tag{3.2}$$

where δt is the laser pulse duration, v is the velocity of the packet and $3.2 \times 10^{-19}\,J$ is the energy needed to create one exciton. This treatment assumes that all the excitons created are in the detected packet (not true as will be seen in the next chapter) and that the volume of the packet is the width of the detected signal multiplied by the velocity.

The bottom graph of fig. 3.14 shows the critical density calculated from the critical intensity of the above graph. The line is the theoretical density needed for condensation (from eq. 1.14). We see that at low temperatures ($< 4.2\,K$) the data fit well with the theoretical one. For higher temperatures the data is shifted to the right of the theoretical line. This could be attributed to the fact that when we illuminate the sample most of the light hits the sample holder surrounding the crystal. As mentioned in the previous chapter the holder is made out of copper which easily conducts heat. Most of the heat produced by the laser beam is dissipated in the sample holder, where the temperature sensor is connected. Helium gas is not as good as liquid He for thermal contact and heat dissipation. As a result, at $T > 4.2\,K$ the temperature of the sample is likely to be higher than the actual measured temperature. If this effect could be corrected the data points at temperatures above $4.2\,K$ would be shifted to the left, bringing them in better accordance with the theoretical line.

Figure 3.15 shows the critical intensity for an illumination wavelength of $532\,nm$. This data is taken from reference [10]. The line in this case is a best fit using eq. 3.1 with the constant equal to 3.5. We see that it falls in good agreement with theoretical predictions since the critical density is proportional to the critical intensity.

We can thus conclude that the intensity phase diagram of the exciton clouds is independent of the initial conditions of illumination. Both illumination wavelengths give rise to exciton clouds that follow the theoretical temperature variations.

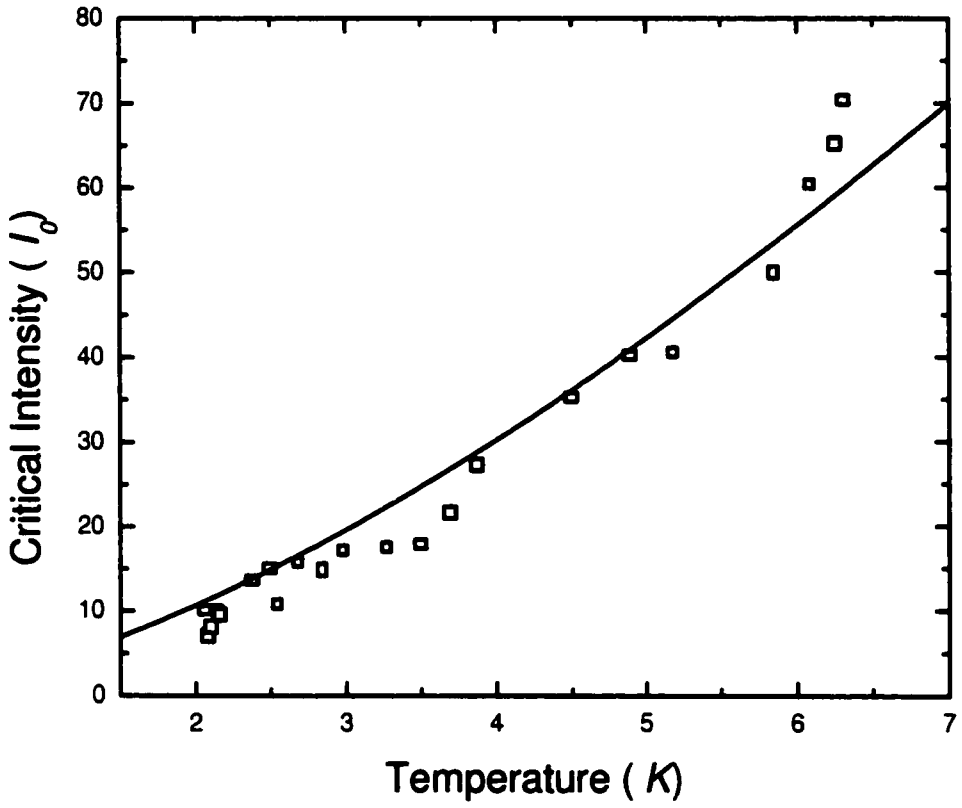

Figure 3.15: Critical intensity causing a condensed exciton packet as a function of the sample temperature for an illumination wavelength of $532\,nm$. The fit is the least square fit of $y = cst \cdot T^{3/2}$ (cst=3.78). Data taken from reference [10].

3.2 Double Pulse Illumination

Since all the particles in the exciton cloud all have the same wave function when in the condensed phase, interference should be visible when dealing with two independent condensates. These two condensates can be created in two ways: by sending two laser pulses on the sample with a delay between them (longitudinal separation) or by sending the two pulses with a spatial separation between them (lateral separation).

3.2.1 Longitudinal Separation

Longitudinal separation between two condensates is achieved by using the setup described in sec. 2.4.4. An example of results at $\lambda = 585\,nm$ for two delays is presented in fig. 3.16. The intensity of the two laser pulses is $3\,I_0$. The top graph is for a delay of $155\,nsec$ and the bottom one for $320\,nsec$. The traces labeled A are the excitonic signal of the individual pulses (meaning that they are taken when the other is not illuminating the sample). The one arriving first is dubbed main and the second delayed. We can see the optical trigger of the delayed pulse, giving us the value of the delay between the pulses. Trace B is the result when the two pulses are illuminating the sample sequentially. Trace C is simply the algebraic sum of the two traces A. One thing we can notice from the two graphs is that the maximum of trace B is much higher that the maximum of the algebraic sum (trace C). Also, the maximum when both pulses are illuminating the sample does not coincide with the maximum of either individual pulse; it stands between the two.

Figure 3.17 shows the traces for multiple delays of both laser pulses illuminating the sample, again at $\lambda = 585\,nm$. We see that as the delay is increased between the two pulses we reach a maximum in the trace B. Figure 3.18 is a plot of the amplitude of excitonic signal B and C as a function of the delay. A maximum occurs at around $225\,nsec$ in the case where both laser pulses illuminate the sample. The algebraic sum of the individual pulses show a maximum at $0\,nsec$ instead of $225\,nsec$; the algebraic sum amplitude is taken at the time position of the main pulse plus half the delay. If we look at results at $\lambda = 532\,nm$ (fig. 3.19) we see that the maximum for the excitonic signal when both laser pulses illuminate the sample is now around $60\,nsec$, much lower than in the case of $\lambda = 585\,nm$, but the signal is still higher than the algebraic sum of the individual pulses. It also shows a sharp decrease as compared to the illumination at $585\,nm$ which is much slower to merge with the amplitude of the algebraic sum.

These differences are mainly due to the amplitude differences of the exciton clouds

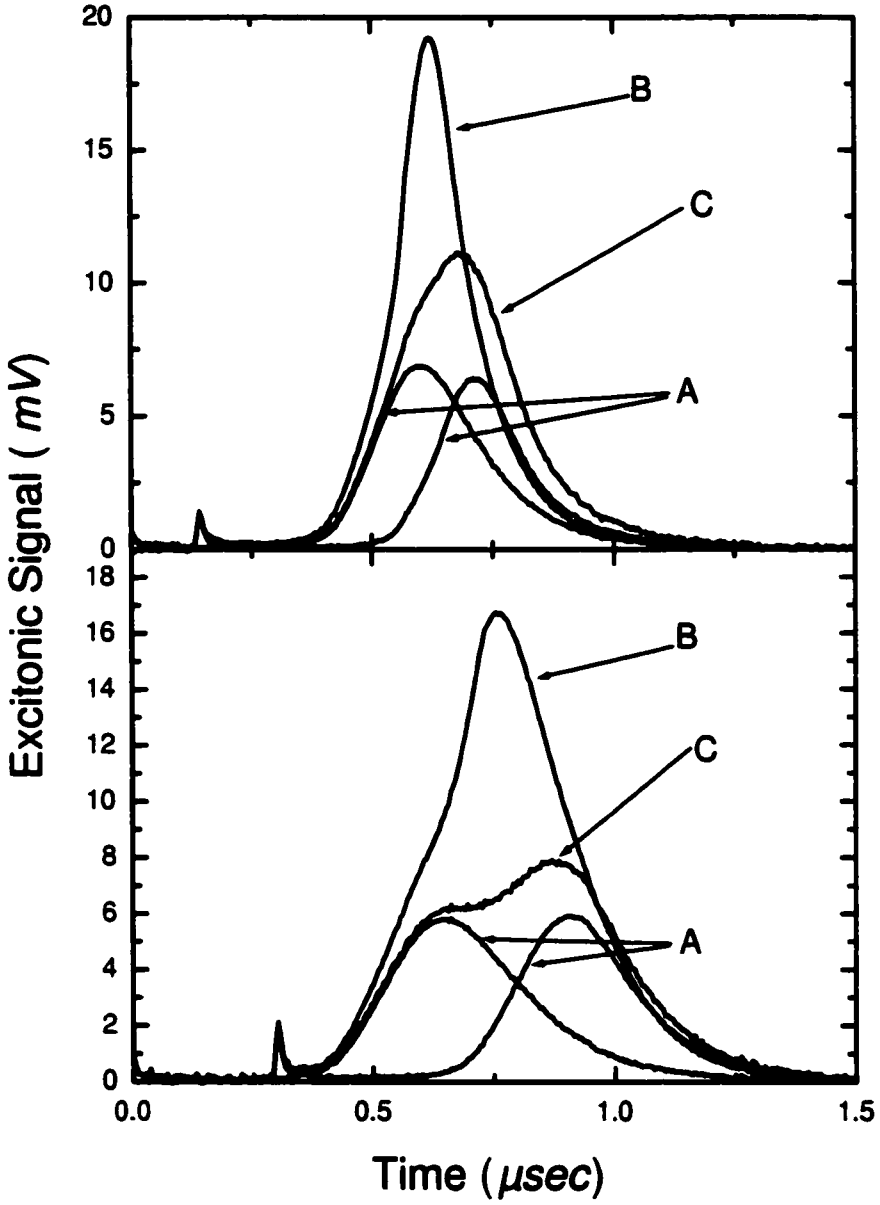

Figure 3.16: Example of longitudinal separation interference at $\lambda = 585\,nm$. Two laser pulse delays are shown: $155\,nsec$ top graph and $320\,nsec$ bottom graph. Traces A correspond to the excitonic signal of both pulses illuminating the sample independently, trace B is when both pulses illuminate the sample simultaneously and trace C is the algebraic sum of the two individual pulse signals.

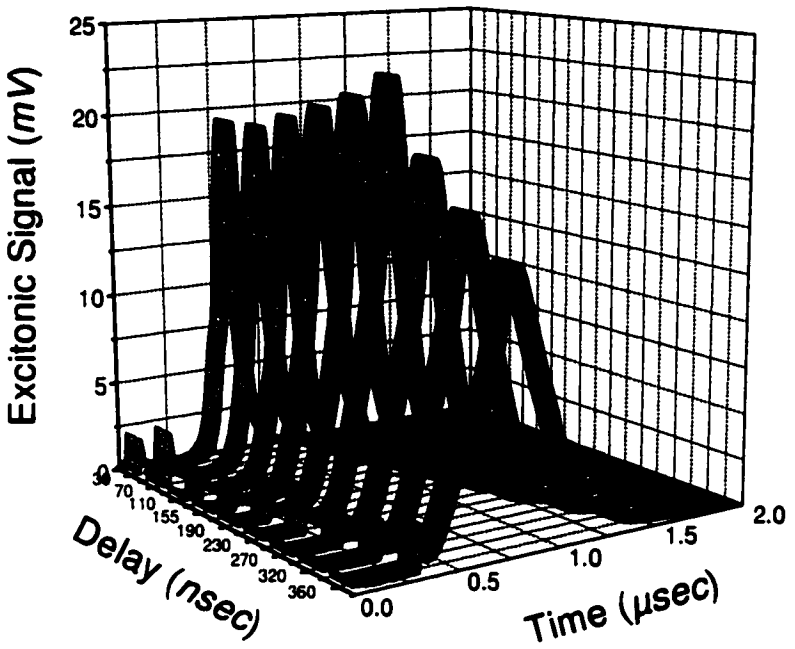

Figure 3.17: Excitonic signal when both laser pulses at $\lambda = 585\,nm$ illuminate the sample simultaneously for different laser pulse delays.

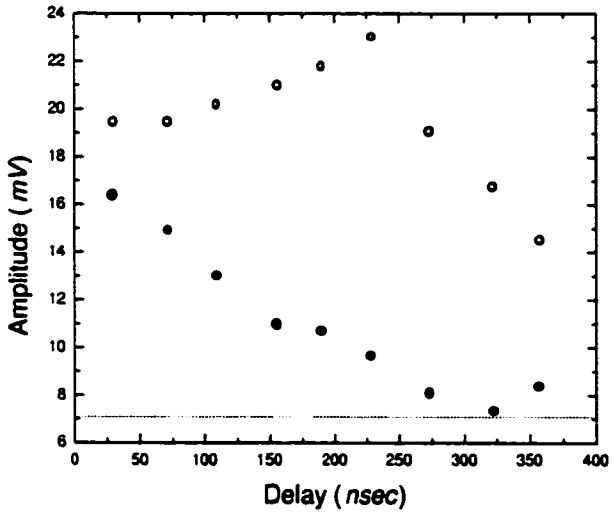

Figure 3.18: Amplitude for $\lambda = 585\,nm$ of the different excitonic signals as a function of the delay between the two laser pulses. The filled circles represent the amplitude of the algebraic sum of the excitonic signal of the individual pulses at the middle position between the two. The open circles represent the maximum amplitude when the two pulses illuminate the sample sequentially.

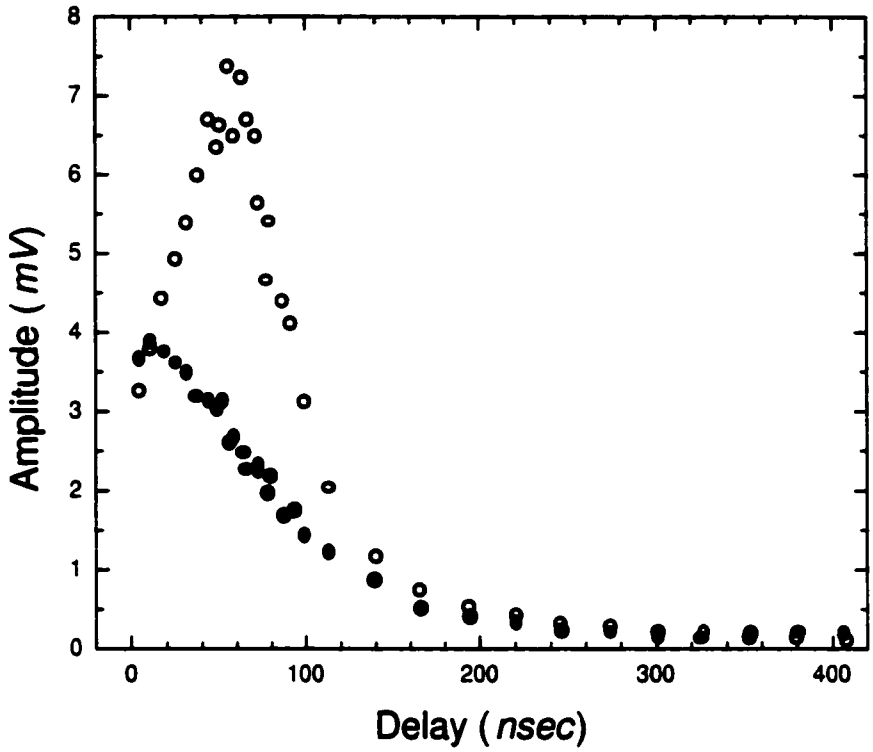

Figure 3.19: Amplitude for $\lambda = 532\,nm$ of the different excitonic signals as a function of the delay between the two laser pulses ($6\,I_0$). The filled circles are the amplitude of the algebraic sum in the middle position between the two pulses. The open circles are the amplitude in the middle position between the two pulses when they both illuminate the sample. Taken from reference [10].

created at a same laser pulse intensity. The exciton clouds created at either laser wavelength always have the same HWHM x 2 when at the same intensity (see fig. 3.7). The difference comes from the fact that the two excitation wavelengths produce exciton clouds of different amplitudes (at same intensities); if the amplitude of the exciton cloud is higher ($585\,nm$) and the HWHM x 2 is the same at both illumination wavelengths, the width at the base must be larger. Also the penetration depth of the laser at $585\,nm$ is much larger than at $532\,nm$. The net effect on the exciton clouds is that at $\lambda = 532\,nm$ they become separated at a delay much lower than at $\lambda = 585\,nm$. At low delays the two exciton clouds merge into one, acting as if the sample was only illuminated with one

laser pulse of a higher intensity. When the delay between the two laser pulses is increased the delayed exciton cloud interacts with the tail of the main cloud, merging with the tail excitons to form a larger delayed cloud. When the delay is large (enough so that the delayed cloud does not come in contact with the tail of the first) no interaction between to two clouds is visible. This occurs for both excitation wavelengths.

3.2.2 Lateral Separation

When considering interference we often think of Young's two slit experiment. The experiment is adapted here in the context of excitons instead of light by using the setup described in sec. 2.4.4. The laser pulse is split in two by the slits and thus creates two individual exciton clouds which can then interact with each other since they have a common phase.

Figure 3.20 shows the traces of the exciton signal created with a laser pulse at $\lambda = 585\,nm$ for four different laser pulse intensities. The slits used are $0.3\,mm$ wide and separated by $1\,mm$. We see again results similar to the longitudinal separation of two laser pulses. The two bottom excitonic signals are the result of illumination of only one slit (left and right slit). The dashed trace is the mathematical sum of the excitonic signal resulting from the illumination of the individual slits. The dotted trace is the observed excitonic signal when both slits are illuminated simultaneously. Like in the preceding section the observed signal is higher in amplitude than the mathematical sum of the individual signals. Figure 3.21 shows traces of exciton clouds created at $\lambda = 532\,nm$ (from reference. [10]).

By using fig. 3.4 we can find the intensity of a single laser pulse that would give rise to the same observed signal when both laser pulses are illuminating the sample; these results are listed in table 3.1. This is to see if the resulting packet is simply as if the crystal was illuminated with a single pulse at twice the intensity.

The first effect of illuminating the sample with two spatially separated laser pulses at $\lambda = 585\,nm$ is thought to be partly the same as illuminating the sample with one laser pulse at twice the intensity of the individual ones (this at low intensities), no amplification occurs in this case. At $\lambda = 532\,nm$ the factor is larger than 2, signaling that an amplification (attractive interaction between the two clouds) also occurs at the beginning of the formation of the condensate. The difference between the two sets of results may be from the fact that the penetration depth of the two laser pulses is quite different ($532\,nm$: $3.3 \times 10^{-4}\,cm$ and $585\,nm$: $8 \times 10^{-3}\,cm$). Also the number of excitons

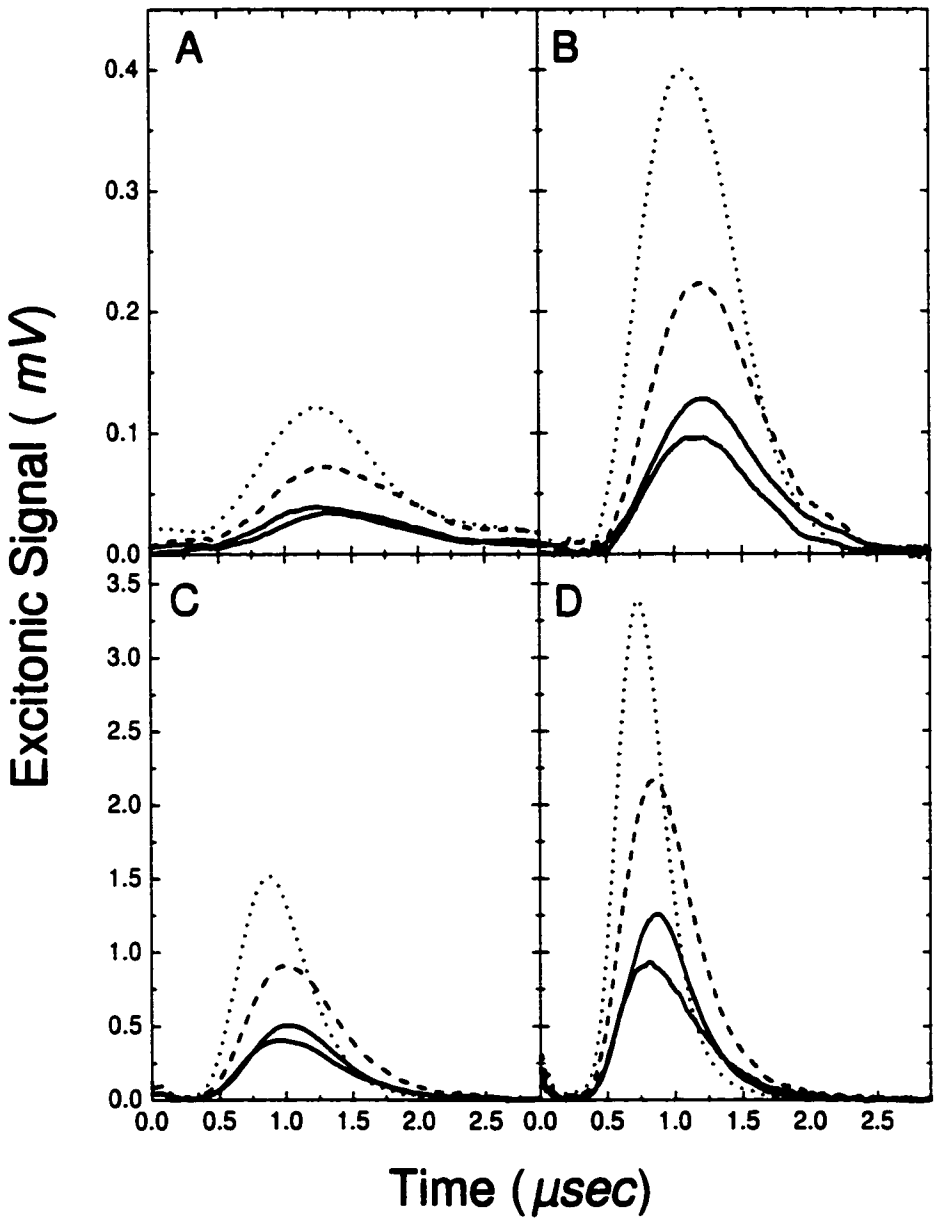

Figure 3.20: Lateral separation interference at $\lambda = 585\,nm$. Each graph is for a different pulse intensity: A: $0.35\,I_0$, B: $0.45\,I_0$, C: $1\,I_0$ and D: $1.5\,I_0$. Slit separation of $1\,mm$ and $0.3\,mm$ wide. For each graph the solid traces are the exciton clouds resulting from the illumination of each slits, the dotted trace is when both slits are illuminated simultaneously and the dashed trace is the algebraic sum of the exciton signal of each slit individually.

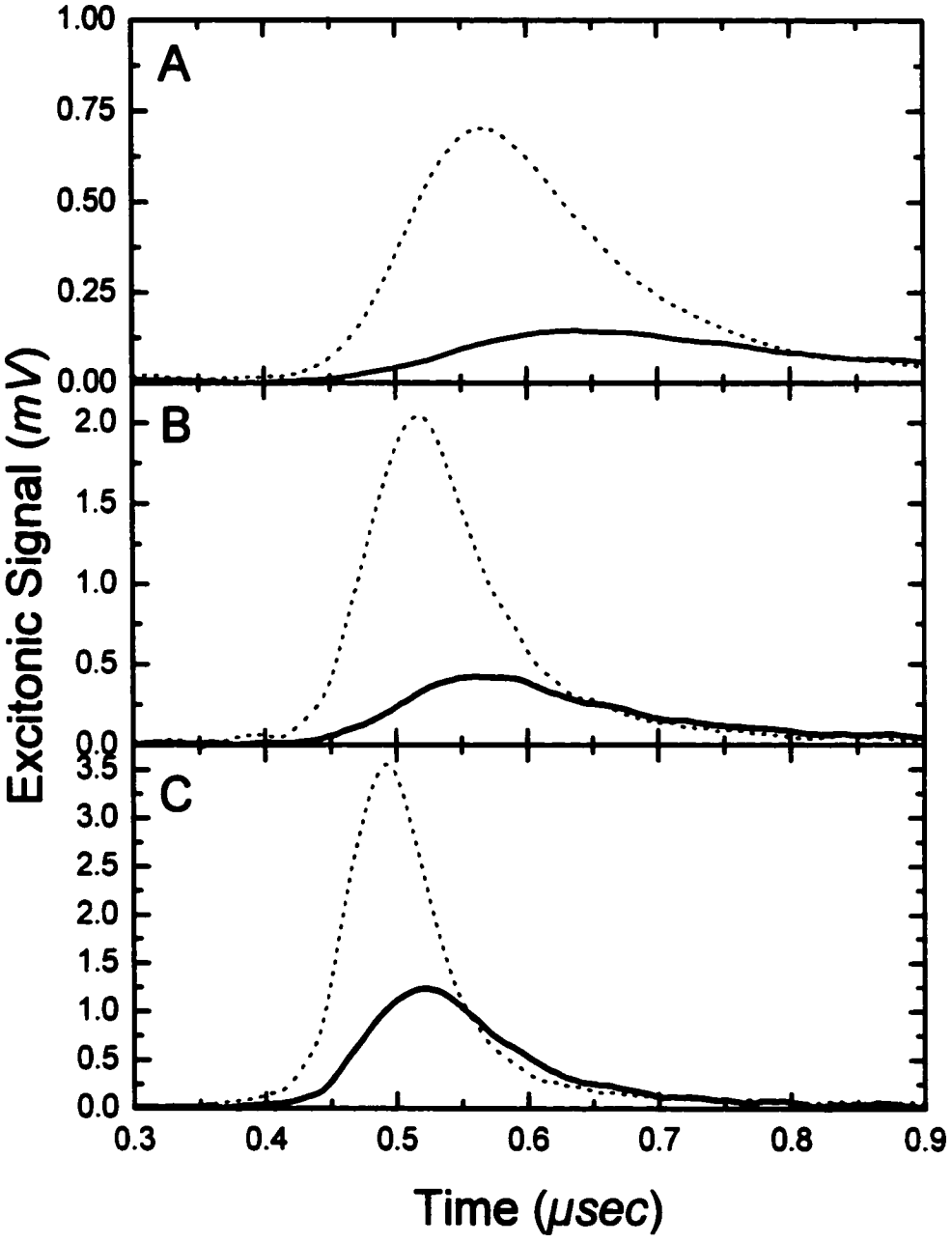

Figure 3.21: Lateral separation interference at $\lambda = 532\,nm$. Each graph is for a different pulse intensity: A: $1\,I_0$, B: $1.6\,I_0$ and C: $3.3\,I_0$. Slit separation of $1\,mm$ and $0.3\,mm$ wide. In each pair the solid trace is the average of the individual single slit traces and the other (dotted) is trace from the double slit. From reference [10].

$\lambda = 585\,nm$			$\lambda = 532\,nm$		
Laser intensity on 1 slit in I_0	Resulting laser intensity in I_0	Factor	Laser intensity on 1 slit in I_0	Resulting laser intensity in I_0	Factor
0.35	0.5	1.4	1	2.2	2.2
0.45	0.9	2	1.6	6	3.8
1	1.8	1.8	3.3	12	3.6
1.5	3	2			

Table 3.1: Equivalent single laser pulse intensity to give rise to the excitonic signal when two slits are illuminated.

in the exciton cloud may be different in the two cases, it is thought that in the case of an illumination at $\lambda = 532\,nm$ less excitons are in the packet (this will be further investigated in the next chapter). This could explain why the equivalent intensity for a one pulse illumination is higher than twice the intensity of the two individual pulses. These two factors could affect the initial interaction between the two separate clouds. Further investigation at different intensities at $\lambda = 585\,nm$ are needed to fully compare with the case at $\lambda = 532\,nm$ done previously.

Chapter 4

Stimulated Emission of Excitons into the Condensate

4.1 Single Pulse + CW Excitation

How does a "cold" population of excitons interact with the moving condensate? This section deals with this question. The injection of the thermal ("cold") excitons is achieved using the procedures described in sec. 2.4.5. This was previously done but only at an illumination wavelength of $\lambda = 532\,nm$ [36], it is here done by comparing the two illumination wavelengths used in the previous chapter. The average steady state density of excitons n created in the crystal is given by:

$$n = \frac{A\,I_{CW}}{V}\frac{\lambda}{h\,c}(1-R)\tau, \tag{4.1}$$

where A is the illuminated area, I_{CW} is the laser intensity, V the crystal volume, λ is the CW laser wavelength, $(1-R)$ includes the light loss due to reflections and τ the paraexciton lifetime. In our case this can be simplified to:

$$\begin{aligned} n &= 4\times 10^{17}\cdot I_{CW}\cdot\tau\,cm^{-3} \\ &\textit{using}: \\ A &= \pi/4\cdot 0.1^2 = 0.00785\,cm^2 \\ V &= 3.68\cdot 3.58\cdot 1.94 = 25.55\,mm^3 = 0.0255\,cm^3 \\ \lambda &= 609.86\,nm = 6.0986\times 10^{-5}\,cm \\ R &= 0.5. \end{aligned} \tag{4.2}$$

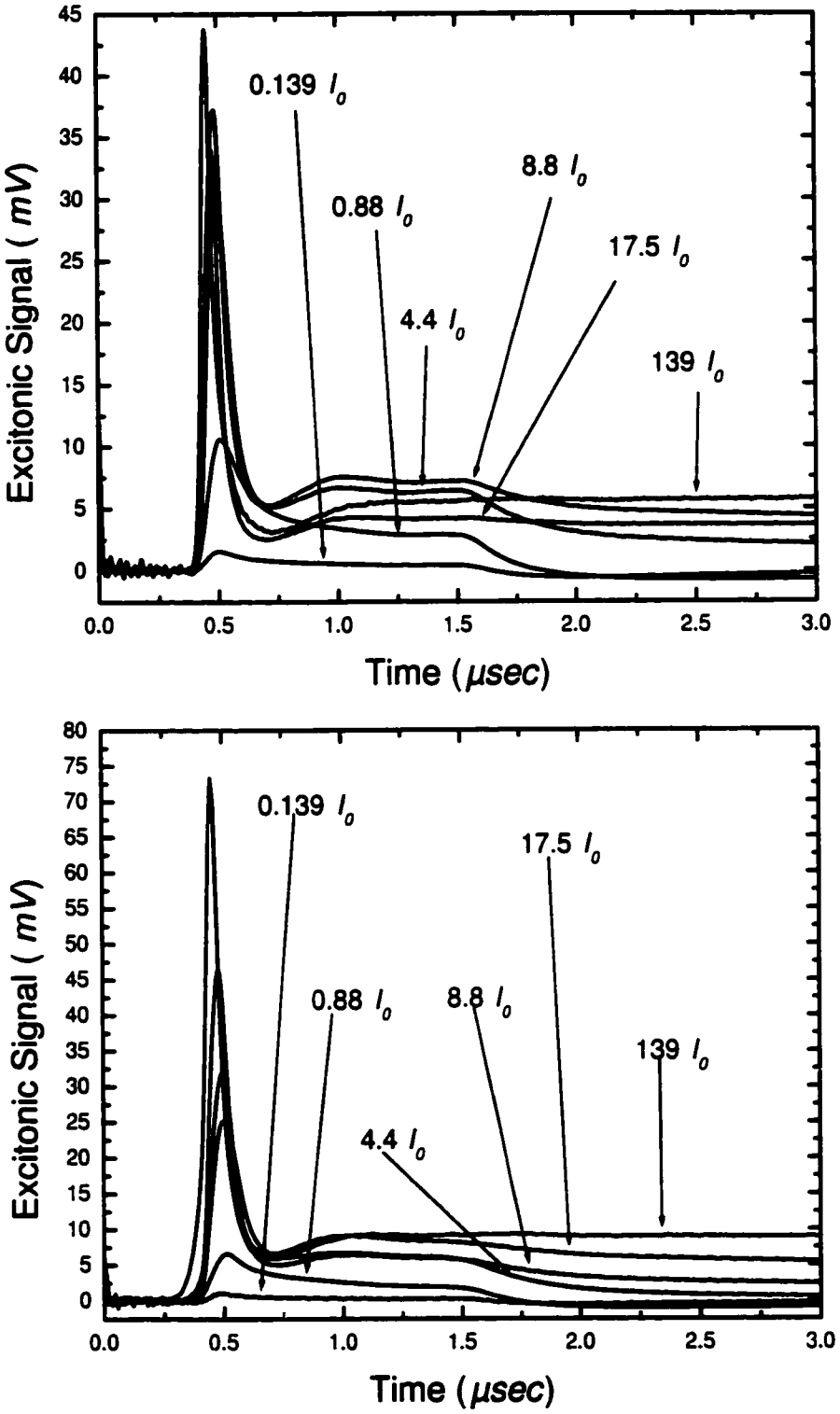

Figure 4.1: Experimental results for an excitation wavelength at $532\,nm$ (upper graph) and $585\,nm$ (lower graph) at various laser intensities at $T = 2\,K$ in the presence of an orthogonal CW laser beam tuned at $\lambda = 609.86\,nm$ with an intensity of $7.5\,W/cm^2$.

The effect of adding the thermal excitons in the path of the moving exciton cloud can be seen in fig. 4.1. The thermal excitons are created by a CW laser beam tuned at the 1S orthoexciton energy ($E_{1S} = 2.0329\,eV$). They are dubbed cold simply because the photons have no excess energy when they create the excitons apart from the $12\,meV$ resulting from the ortho to para transition. We see the resulting packets (biggest peak at around $0.5\,\mu sec$) with a tail following it (dubbed the plateau). At low pulsed laser intensity the plateau dies off at around $1.5\,\mu sec$, corresponding to three transit fractions of the main packet. A transit fraction corresponds to the time it takes for the packet to travel form one face of the crystal to the other. At higher pulsed laser intensity we see that the plateau does not die at three times the transit fraction, but continues for times up to $40\,\mu sec$[10]. Comparing the two graphs (two excitation wavelengths) we see no qualitative differences.

To explain this phenomena we can try to visualize the shape of the exciton cloud. The exciton cloud can be viewed as having three components: a core, a coma and a tail. To put this in a more graphic perspective we can think of the exciton cloud as a comet. The core is where the condensed excitons are, the coma surrounds the core and is composed of non-condensed excitons and finally a tail of non-condensed excitons following the first two components. If the crystal is only illuminated with a single pulsed laser we mostly detect the core and the coma of our exciton cloud, the tail is so long and faint in intensity that we do not see it. When the population of thermal excitons is present in the crystal the tail of the exciton cloud becomes visible (plateau). To explain this we assume that the tail of the exciton cloud is linking the two faces of the crystal (the detector's face and the illuminated face). The tail is fed by the population of thermal excitons amplifying it as it sweeps through the sample; this is where the stimulated emission of excitons into the condensate occurs. A schematic of the condensate and its tail can be found in reference [10] (note that in the schematic the term filament is used instead of tail). The tail is destroyed at three transit fractions probably because at that condensate density it can completely deplete the background of thermal excitons injected by the CW laser beam; at higher densities the tail can survive for even longer time.

If we now look at fig.4.2 we see the amplitude of the main packet and the total integrated signal of the excitonic cloud as a function of the pulsed laser intensity (the CW laser intensity remains fixed at $7.5\,W/cm^2$). We see that the amplitude and the integrated signal when the thermal excitons are present in the crystal are independent of the illumination wavelength. On the graph are also shown the resulting amplitude and the integrated signal when no thermal excitons are present; in this case there is a

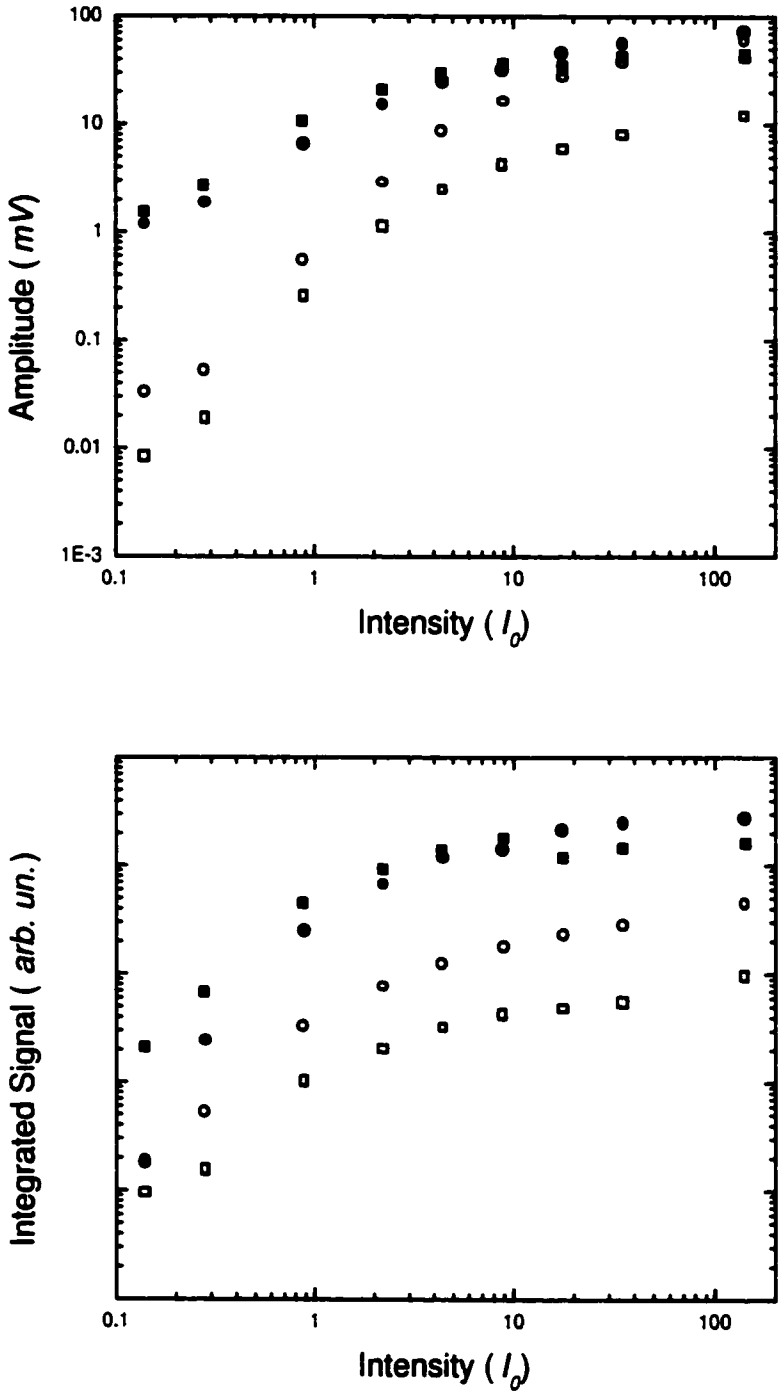

Figure 4.2: Amplitude (top graph) and integrated signal (bottom graph) of the main peak in the excitonic signal given when the crystal is illuminated with or without an additional orthogonal CW laser beam tuned at $\lambda = 609.86\,nm$ with an intensity of $7.5\,W/cm^2$. The squares correspond to an illumination at $\lambda = 532\,nm$ and the circles at $\lambda = 585\,nm$. Filled symbols correspond to the addition of the CW laser beam illuminating the sample and the open symbol otherwise.

difference (as discussed in sec. 3.1.1). We also notice that at high intensity the curves (except the one at $532\,nm$ with no thermal exciton) tend to converge.

The two graphs (traces in the presence of the CW beam) show basically the same result: when injecting the crystal with a population of thermal excitons the properties of the main packet become closely identical for the two illumination wavelengths. This tells us that in the case of the illumination at $532\,nm$ with no CW, less excitons reach the detector than in the case of $585\,nm$. With the injection of the thermal excitons in the crystal volume we seem to collect more of the excitons that were left behind the packet (the ones in the tail). This would tell us that for a fixed laser intensity (fixed number of photons) we always lose the same number of excitons, either by surface recombinations or by phonon induced recombinations. This number being different in either illumination wavelength. The only difference between an illumination at $585\,nm$ and one at $532\,nm$ is that there is more non-condensed excitons in the tail following the condensed core in the case at $532\,nm$.

If we look at the normalized velocity of the main packet and its HWHM x 2 on fig. 4.3 we see two main traces: with thermal excitons and without. Again these two properties are independent of the pulsed illumination wavelength when also illuminated with the CW laser beam. The difference with the velocities with no CW illumination is that we inject thermal excitons before the arrival of the exciton cloud thus creating packets that will have more condensed particles; as a result the velocity of the main packet is always close to the saturation point (around 96% of the velocity of sound in the crystal). The same thing happens with the HWHM x 2; it does not reach large widths at low intensity when illuminated with the CW laser beam because the packet is more condensed since it has a larger number of particles.

But what would happen if we would inject thermal excitons in the crystal with a pulsed laser instead of a CW laser? By using a pulse laser instead of the CW laser, we could control when we inject the thermal excitons, thus hitting different part of the exciton cloud. This type of experiment was performed and results are presented in the next section.

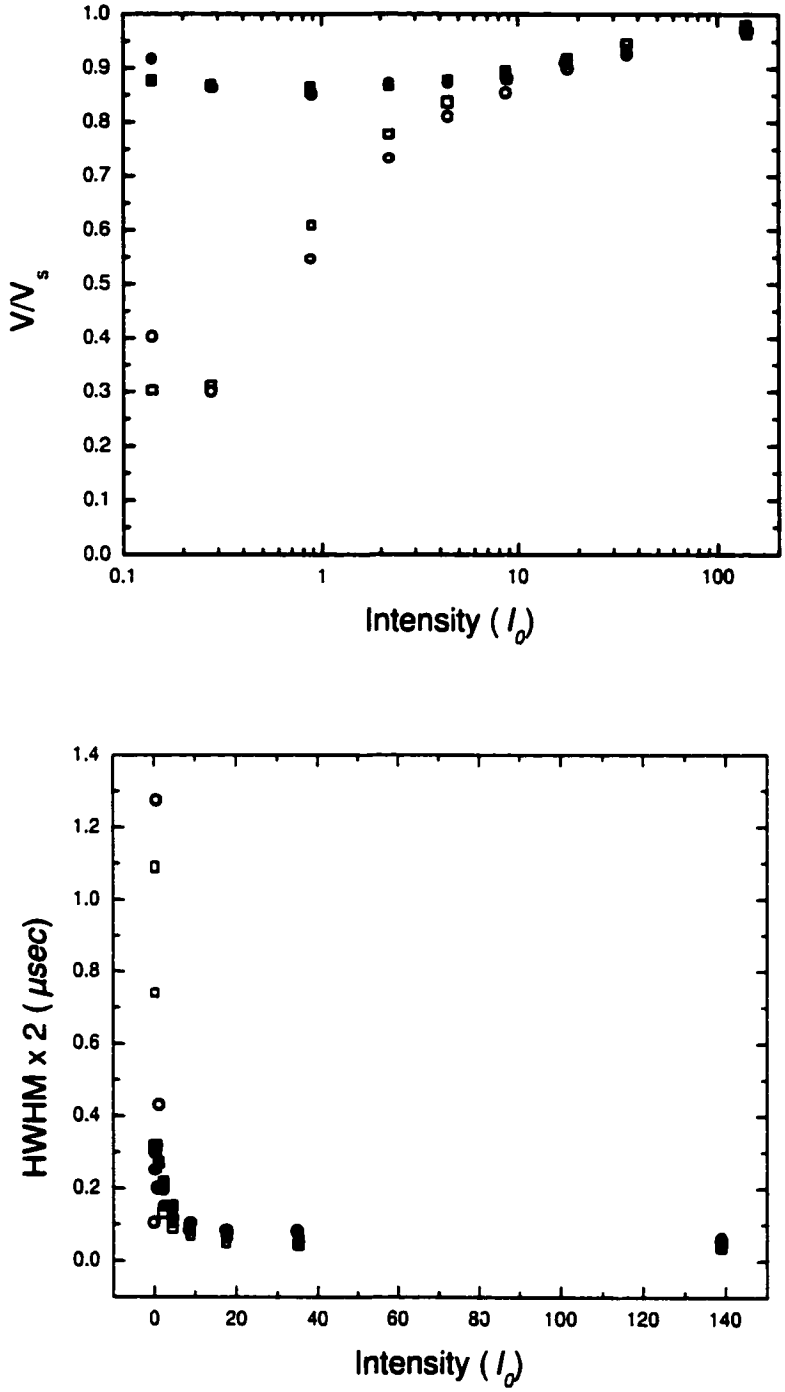

Figure 4.3: V/Vs (upper graph) and HWHM x 2 (bottom graph) of the main peak in the excitonic signal given when the crystal is illuminated with or without an additional orthogonal CW laser beam tuned at $\lambda = 609.86\,nm$ with an intensity of $7.5\,W/cm^2$. The squares correspond to an illumination at $\lambda = 532\,nm$ and the circles at $\lambda = 585\,nm$. Filled symbols correspond to the addition of the CW laser beam illuminating the sample and the open symbol otherwise.

4.2 Nd:YAG Pulse + Pulsed Excitation

The injection of thermal excitons with a CW laser beam is now replaced by injection with a pulsed laser. With a pulsed laser we can control when the thermal excitons are created in the crystal, thus synchronizing the injection of the excitons with the passage of different parts of the exciton cloud. We can thus create the thermal excitons in front, on or behind the moving exciton cloud by varying the delay between the two laser pulses.

The setup used is described in sec. 2.4.6 and once again the wavelength used to create the thermal excitons corresponds to the 1S orthoexciton energy in Cu_2O. Some graphs present the results as function of the transit fraction; as mentioned before one transit fraction is the time for a condensed exciton cloud to travel form one face of the crystal to the other. The time for one transit is approximately $470\,nsec$, this is the transit time for a condensed exciton cloud created with a laser pulse of $\sim 130\,I_0$ (1 transit fraction = $470\,nsec$).

4.2.1 Synchronized injection of thermal excitons in the path of the exciton cloud

An example of the effect of injecting thermal excitons with a lateral laser pulse delayed by $240\,nsec$ (transit fraction of ~ 0.5) is shown in fig. 4.4. The Nd:YAG laser has an intensity of $116\,I_0$, so the exciton cloud is already condensed. The thermal excitons are injected by a laser pulse of $0.15 I_0$, only a fraction of the main YAG pulse intensity. Also this lateral laser pulse is not completely absorbed by the crystal (this will prove useful in the following paragraphs). Trace A is the result from the YAG illumination alone, while trace B is the result when the lateral laser pulse also illuminates the sample. In this case, it illuminates the sample when the exciton cloud passes in front of the illumination spot of the lateral pulse. We see that the thermal excitons greatly amplify the signal of the initial exciton cloud (factor of ~ 13). Also the base of the exciton cloud signal is now enlarged on the fall side.

As mentioned above, the lateral laser pulse is not completely absorbed by the crystal ($\alpha \sim 3\,cm^{-1}$, crystal length $= 0.35\,cm$, giving an absorption of $\sim 34\%$). By monitoring this transmitted light we can investigate what is happening in the crystal regarding the amplification of the condensate. Figure 4.5 shows the resulting time-resolved signal of the transmitted lateral laser light detected by a nanosecond photodetector. The trace labeled A is the signal from the transmitted lateral light alone and trace B is the signal

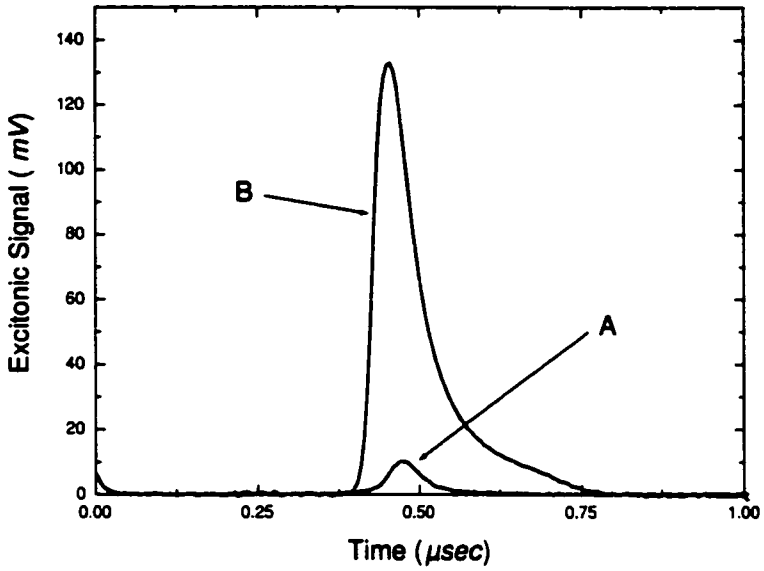

Figure 4.4: Excitonic signal detected when illuminating with only the YAG laser (trace A) and when both the YAG laser and a delayed lateral laser pulse ($\lambda = 609.83\,nm$) (trace B) are illuminating the sample. The intensity of the YAG is $116\,I_0$ and the intensity of the lateral laser pulse is $0.15\,I_0$. The delay between the two pulses is $240\,nsec$.

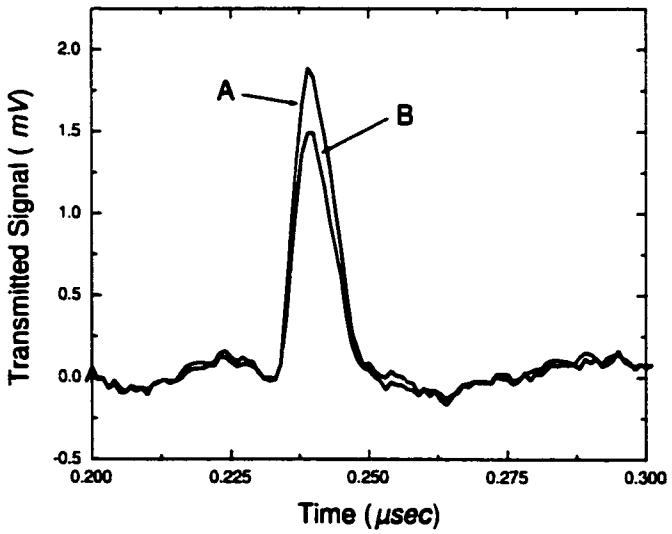

Figure 4.5: Transmitted light of the lateral laser pulse detected when illuminating with only the lateral laser (trace A) and when both the YAG laser and a delayed lateral laser pulse ($\lambda = 609.83\,nm$) (trace B) are illuminating the sample. The intensity of the YAG is $116\,I_0$ and the intensity of the lateral laser pulse is $0.15\,I_0$. The delay between the two pulses is $240\,nsec$.

of the transmitted lateral light hitting the crystal at the same time an exciton cloud is traveling in the path of this lateral laser pulse. The delay between the two laser pulse (YAG and lateral pulse) is $240\,nsec$, which means that when the lateral pulse hits the crystal the exciton cloud is in front of the lateral pulse. We see that when the exciton cloud is present in the path of the thermal excitons or of the lateral laser pulse in the crystal, the intensity of the transmitted lateral light is diminished.

But are those effects really associated with the presence of resonant 1S excitons in the crystal? Figure 4.6 shows the normalized differential attenuation (NDA) of the lateral laser pulse and the amplification factor as functions of the detuning of the energy of the lateral laser pulse from the 1S orthoexciton energy. The NDA is defined as (I-I')/I, where I is the transmitted lateral light intensity in the absence of an exciton cloud (trace A of fig. 4.5) and I' is the intensity transmitted in the presence of an exciton cloud in the crystal (trace B of fig. 4.5); the amplification factor is defined as the ratio of final to initial exciton signal amplitude. We see that both the NDA and the amplification factor drop to 0 and 1 respectively at detunings of $\pm 4 \times 10^{-4}\,eV$, showing that these two phenomena are indeed possible only if resonant excitons are created in the crystal.

Is the exciton cloud picking up that many thermal excitons that the lateral light has additional phase space to create some more (frees up phase space for more light absorption) or is the lateral light scattered or reflected by the exciton cloud? Also since we inject only a relatively small amount of thermal excitons, how can we have an amplification that large? By varying the delay between the two laser pulses (variation of the relative position of the exciton cloud and the thermal excitons) we can perhaps solve these questions.

Figure 4.7 shows the amplification factor of the excitonic clouds signal and NDA of the lateral laser pulse as functions of the transit fraction (trigger time) for the same laser pulse intensities as in fig. 4.4. We see that the amplification factor reaches a maximum at a transit fraction of around $\sim$ 70%, this when the exciton cloud has passed the illumination spot of the lateral laser pulse; the tail of the cloud is thus in front of the illumination spot. At lower transit fractions we always have an amplification even if the lateral laser pulse hits the crystal before the exciton cloud can be in contact with it. This is simply due to the fact that the thermal excitons have a long lifetime, they are still in the crystal volume when the exciton cloud crosses the crystal length. The amplification factor drops to one after one transit fraction simply because the lateral laser pulse hits the crystal as the exciton cloud is detected producing no effect on the main exciton cloud, yet still affecting the tail. This will be discussed later. The NDA reaches a maximum at

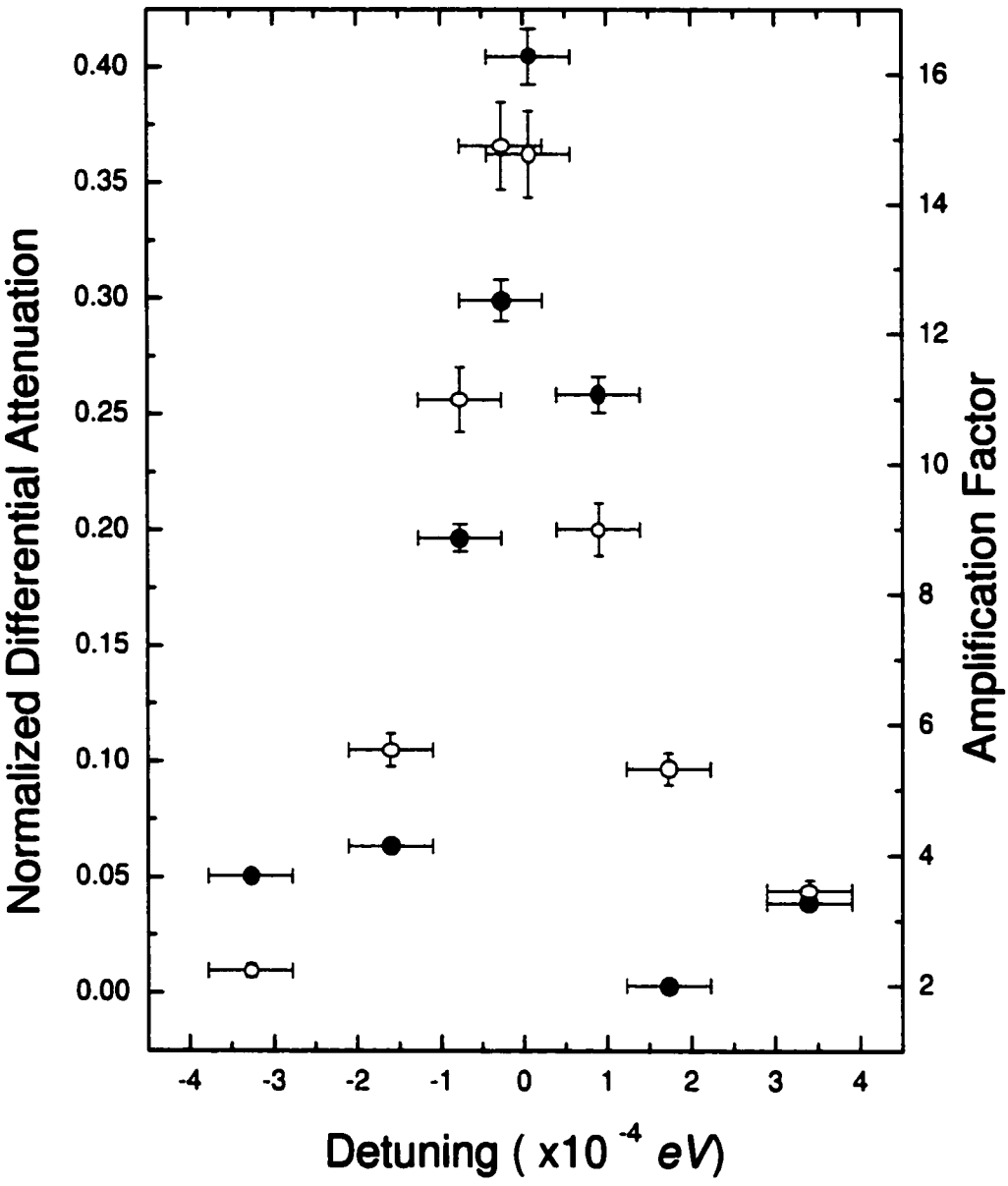

Figure 4.6: Amplification factor (open circles) of the condensate and normalized differential attenuation of the lateral laser pulse (filled circles) as functions of the lateral laser pulse energy detuning from the orthoexciton energy. The YAG intensity is $116\,I_0$, the lateral laser pulse intensity is $0.15\,I_0$ and is delayed by $310\,nsec$.

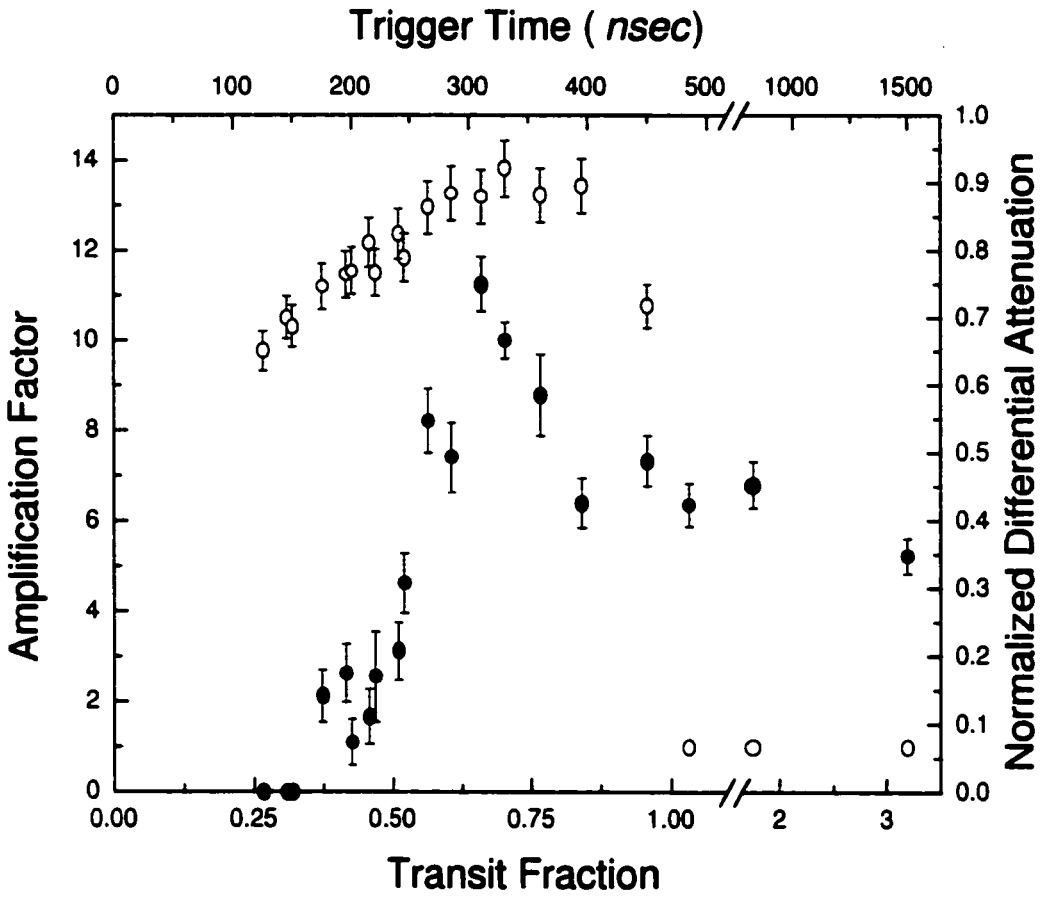

Figure 4.7: Amplification factor (open circles) of the condensate and normalized differential attenuation of the lateral laser pulse (filled circles) as functions of the transit fraction of the packet (trigger time of the lateral laser pulse). The YAG intensity is $116\,I_0$ and the lateral laser pulse intensity is $0.15\,I_0$.

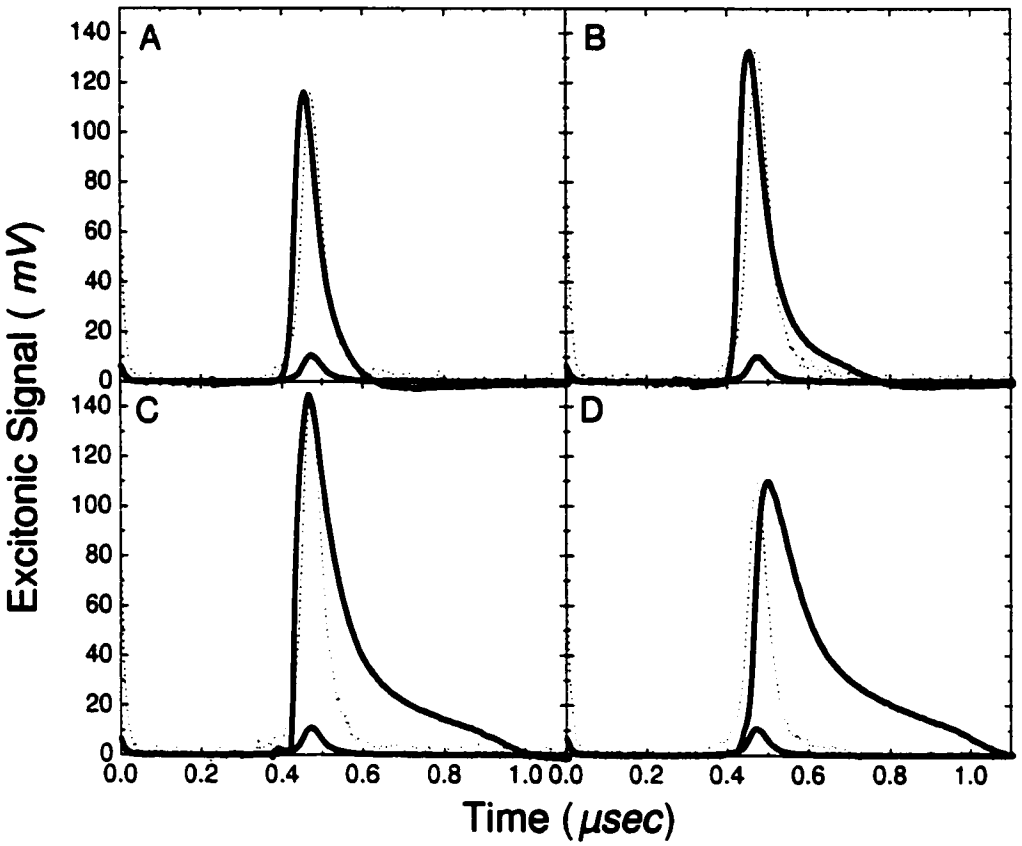

Figure 4.8: Excitonic signal showing the exciton packet and the amplified packet for trigger times A: 145 *nsec*, B: 240 *nsec*, C: 395 *nsec*, and D: 450 *nsec*. The dashed curves represent the original exciton packet multiplied by a factor to make them correspond to the amplified packets. The YAG intensity is $116\,I_0$ and the lateral laser pulse intensity is $0.15\,I_0$.

a transit fraction slightly smaller ($\sim$ 65%) than for the amplification factor. We see that for transit times smaller than 35% no attenuation is produced as expected (the lateral laser pulse crosses the crystal before the exciton cloud reaches it). For transit fractions higher than one, we see a different scenario than for the amplification factor: the NDA doesn't drop to zero but stays at values around 40% up to a transit fraction higher than 3! It even seems to follow the same trend as the plateau did when the injection of thermal excitons is done with the CW (see fig. 4.1). It drops at two transit fractions and again at three (larger trigger times are needed to conclude further on this observation). This means that something is in front of the illumination spot of the lateral laser pulse even at long times.

Let us look at a few traces at different delays to see what could be happening. Figure 4.8 shows the excitonic signal and the amplified excitonic signal for four trigger times: 145, 240, 395 and 450 $nsec$ (transit fraction: 0.3, 0.51, 0.84 and 0.95). We also see dashed curves that represent the non-amplified excitonic signal multiplied by a numerical factor to have its amplitude match the amplitude of the amplified excitonic signal. The main thing that can be seen on these four graphs is that the tail of the amplified signal widens and its amplitude relative to the main peak increases as the trigger time is increased. The second thing noticeable on the graph is the position of the maximum of the amplified excitonic signal. With the aid of the dashed traces we can see that for graph A and B the amplified signal is faster than the non-amplified one, for graph C the two signals are very close to each other and finally for graph D the amplified signal is now slower when the exciton cloud is amplified. This could indicate that we "amplify" the non-condensed excitons surrounding and following the core of condensed excitons. As the resonant 1S excitons sweep through the tail of non-condensed excitons they stimulate the non-condensed tail to condense and follow the condensed packet, thus the long tail and shifted maximum. This could explain why the maximums in the graphs are closer to 0.7 transit fraction rather than 0.5.

4.2.2 Investigation of the amplification as a function of laser intensities

To further understand the "amplification" of the exciton cloud, the intensity of the YAG laser was varied for a fixed delay and lateral laser intensity (310 $nsec$ and 0.9 I_0). The delay is that producing the maximum in amplification for a 116 I_0 laser pulse created exciton cloud. The intensities of the YAG cover the range from forming a diffusive to

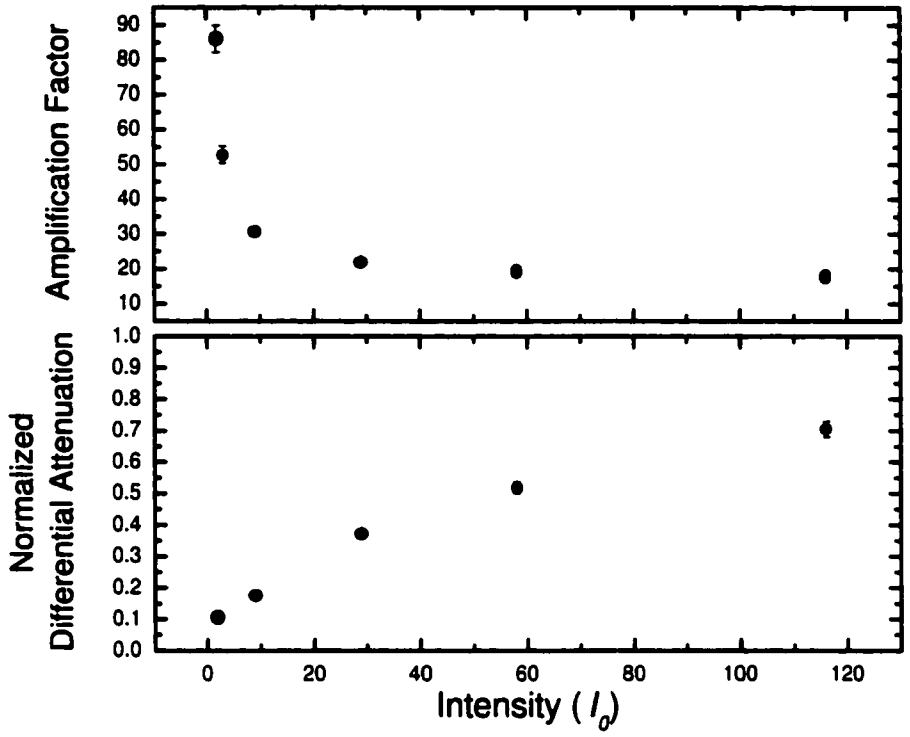

Figure 4.9: Amplification factor of the packet and normalized differential attenuation of the lateral laser pulse as a function of YAG intensity. The intensity of the lateral laser pulse and the trigger time are kept fixed at $0.9\,I_0$ and $310\,nsec$ respectively.

a condensed ballistic packet. We clearly see that at low YAG intensity we get a higher amplification factor than at high YAG intensity. The amplification factor is different but the final amplitude of the amplified exciton cloud varies only a little with YAG intensity; the difference in the amplification factor comes from the amplitude of the non-amplified YAG which varies dramatically with a variation of the YAG intensity. The NDA follows a trend opposite to the amplification factor: it is low at low YAG and high at high YAG. We cannot conclude much from the NDA as a function of YAG intensity because the synchronization is broken as the intensity of the YAG is varied thus coupling two effects: trigger time variation and intensity variation. The synchronization is broken because the exciton cloud velocity changes as the intensity of the YAG laser is changed. The lateral laser pulse was synchronized to hit the crystal for an exciton cloud transit fraction of 65%. As the intensity is lowered the lateral laser pulse goes from hitting the tail of the

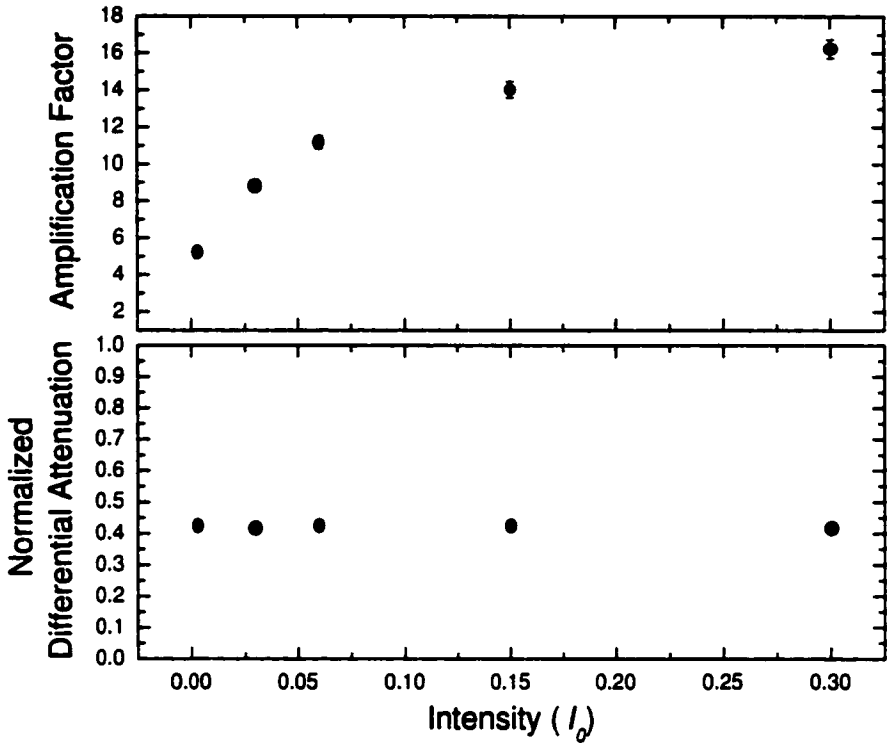

Figure 4.10: Amplification factor of the packet and normalized differential attenuation of the lateral laser pulse as a function of lateral laser pulse intensity. The intensity of the YAG pulse and the trigger time are kept fixed at $116\,I_0$ and $310\,nsec$ respectively.

exciton cloud to hitting the front of the exciton cloud.

The intensity of the lateral laser can also be varied, this without affecting the synchronization. Figure 4.10 shows the results as the intensity of the lateral pulse is varied for a fixed YAG intensity ($116\,I_0$) and fixed trigger time ($310\,nsec$). We see that as the intensity of the lateral laser pulse is increased the amplification factor is also increased. This means that as the number of resonant excitons is increased in the crystal it can trigger more and more non-condensed tail excitons to either condense or simply follow the condensed core of the exciton cloud toward the electrodes. As for the NDA we see that it is independent of the lateral laser pulse intensity. This tells us the attenuation of the laser pulse is probably not due to phase filling effect but simply to the addition of a second absorption coefficient due to the presence of the condensate in the crystal.

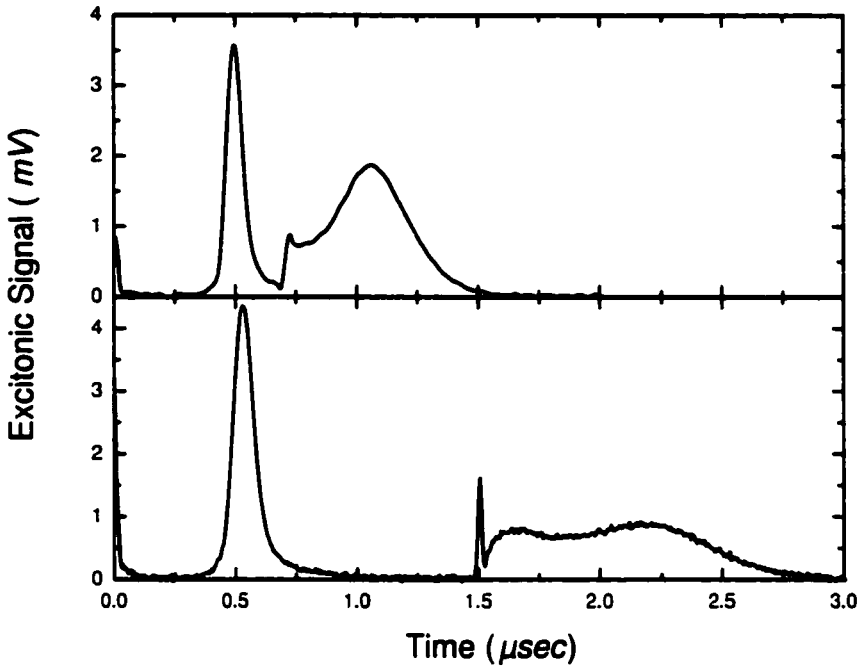

Figure 4.11: Excitonic signal detected with both the YAG laser and a delayed lateral laser pulse illuminating the sample. The top graph is for a delay of $700\,nsec$ (YAG intensity: $10\,I_0$, lateral pulse intensity: $0.007\,I_0$) and the bottom graph is for a delay of $1500\,nsec$ (YAG intensity: $15\,I_0$, lateral pulse intensity: $0.011\,I_0$).

4.2.3 Lateral laser pulse illumination at high transit fraction

What happens to the exciton cloud when illuminated with a lateral laser pulse delayed beyond one transit fraction? Will the tail of the exciton cloud still be "amplified"? Figure 4.11 shows results for delays of 700 and $1500\,nsec$ (transit fractions of 1.48 and 3.2 respectively) and answers part of this question. We see on the two graphs a second packet emerging after the arrival of the lateral laser pulse (the optical trigger of the lateral laser pulse is still visible on the two graphs) without affecting the first excitonic signal detected. This means that the non-condensed excitons in the tail of the exciton cloud are still present in the crystal even $1.5\,\mu sec$ after their creation and they are still triggered to ballisticaly move toward the electrodes. Will this amplification last the lifetime of the excitons ($\tau = 8\,msec$ [14]) or will it stop before? Observations at even higher trigger times are needed to see if it is only the tail's non-condensed excitons that can account

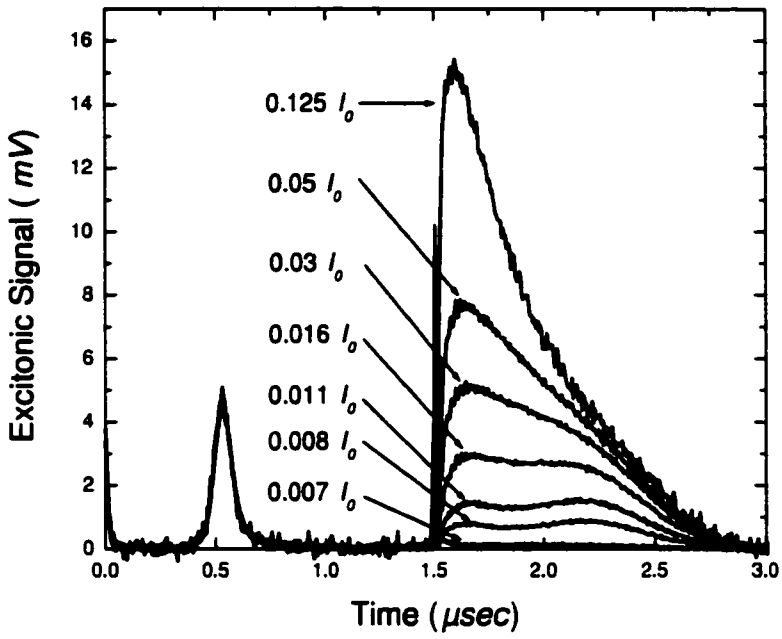

Figure 4.12: Excitonic signal detected when both the YAG laser ($15\,I_0$) and a delayed lateral laser pulse are illuminating the sample for different lateral laser pulse intensities at a fixed delay of $1500\,nsec$.

for this effect.

In fig. 4.12 we can see the effect of the variation of the lateral laser pulse intensity on the second emerging packet. This was done for a trigger time of $1500\,nsec$ and a YAG laser intensity of $15\,I_0$. We can see that the higher the intensity of the lateral pulse the higher the amplitude of the second feature, which also changes shape (it develops a tail). This is similar to the effect on the amplification of the main packet as a function of lateral laser intensity, with a higher lateral laser pulse intensity one is able to trigger more non-condensed exciton (previously in the tail) to form a bigger secondary feature.

The comet explanation for our exciton cloud seems to be confirmed with these experiments; injecting resonantly created excitons in the crystal causes the non-condensed excitons (either from the coma or the tail of the exciton cloud) to condense or to follow the condensed excitons toward the electrodes of the exciton detector.

Conclusion

Observations on the initial exciton cloud have been reported for excitons created in Cu_2O. Two different excitation wavelengths were used to create the exciton cloud in the crystal: $\lambda = 532\,nm$ and $\lambda = 585\,nm$. These two wavelengths permit us to create exciton clouds with different initial sizes since the penetration depth of the laser light is different for the two wavelengths.

We have seen that the main differences between condensate illuminated at the two wavelengths is the amplitude of the signal. At $585\,nm$ the exciton cloud has a much higher amplitude than at $532\,nm$; at this last wavelength fewer excitons reach the detector or follow the exciton cloud. Some of the initial excitons recombine due to the higher phonon population and to surface recombinations (smaller penetration depth). Except for the amplitude and the total integrated signal (measure of the number of excitons) no difference can be seen in the exciton cloud; they both condense at the same laser intensity (same number of initial excitons) and both follow a $T^{3/2}$ function which is prescribed by theory. Also, in the case of an illumination wavelength at $585\,nm$ the final density of the exciton cloud follows the theoretical predictions for the critical density as a function of temperature.

We have then explored the interference for two exciton condensates either created sequentially or laterally. The observed differences between the resulting excitonic signal at the two illumination wavelengths were simply a change in the position of the maximum of amplification (time position) and also a change in the time it took for the amplification to fall to zero (this time was longer at $\lambda = 585\,nm$). These differences are the result of the excitonic clouds having different shapes: at $585\,nm$ the exciton clouds are wider at the base compared to $532\,nm$. The effect on the interference is mainly a function of the base of the two exciton clouds; if they are close enough to be in contact with each other more interactions between the two clouds occurs. For lateral interference, it is thought that at low intensity the resulting effect is the same as illuminating the sample with a single laser pulse at twice the intensity. At higher intensity some interference effects are

visible.

Condensate amplification was also studied to further understand the stimulated emission of excitons into the moving condensate. By using a CW laser to inject resonantly created thermal excitons in the path of the moving exciton cloud, amplification was observable. It was observed that when the thermal excitons are present in the crystal the resulting exciton cloud properties are independent of the illumination wavelength used to create the packets. With the injection of thermal excitons in the crystal we recover the excitons that were left behind the packets and that were never detected. Because the exciton clouds are independent of the illumination wavelength we can conclude that the number of excitons left behind in the case of an illumination wavelength at $532\,nm$ is larger than at $585\,nm$; this because when no CW beam is illuminating the sample the signal is lower at $532\,nm$. We also observe at low pulsed laser intensity ($< 5\ I_0$)the formation of an exciton plateau that disappears at 3 times the transit time of the main exciton cloud. This again could be explained with the comet interpretation of the exciton cloud: the thermal excitons trigger non-condensed excitons to follow the main core of condensed excitons; at high intensity the thermal excitons manage to push more non-condensed tail excitons to follow the main packet, this is why no drop at 3 times the transit time occur.

The CW laser was replaced by a pulsed laser tuned at the same wavelength to probe different parts of the exciton cloud with the thermal excitons. The results showed that the main amplification occurs in the tail of the exciton cloud (non-condensed excitons). This more or less confirms our belief that the exciton cloud is in the shape of a comet. We also saw the formation of a second exciton cloud when the delayed laser pulse hit the crystal after the main exciton cloud is detected, this second packet was observed for delays up to $1500\,nsec$. Again this is thought to be the non-condensed excitons that are left in the crystal volume that condensed and move toward the detector.

Future work will be focused on a further understanding of the amplification of the condensate. A new crystal will be used to suppress the 1S orthoexciton transition. This crystal is oriented differently than the one used in this research; under a certain incident light polarization the 1S orthoexciton transition is forbidden. Thus enabling us to turn on and off the 1S absorption just by changing the laser light polarization. By combining this and the previous ones the phenomenon may be more fully understood. Investigation of the amplification at longer trigger times is also scheduled, this to find the delay where no more effect will be visible (no more secondary packet immerging behind the main one). This could help to pinpoint the exact lifetime of the excitons in the crystal.

Bibliography

[1] A. Griffin, D.W. Snoke and S. Stringari, *Bose-Einstein Condensation*, Cambridge University Press, Cambridge, 1995.

[2] S.A Moskalenko and D.W. Snoke,*Bose-Einstein Condensation of Excitons and Biexcitons: and Coherent Nonlinear Optics with Excitons*, Cambridge University Press, Cambridge, 2000.

[3] E. Benson, E. Fortin and A. Mysyrowicz, *Phys. Stat. Sol. (b)*, **191**, 345 (1995).

[4] I. Loutsenko and D. Roubtsov,*Phys. Rev. Lett.*, **78**, 3011 (1997).

[5] G.A. Kopelevich, N.A. Gippius and S.G. Tikhodeev, *Solid State Commun.*, **99-2**, 93 (1996).

[6] A.R. Vasconcellos, M.V. Mesquita and R. Luzzi, *Europhys. Lett.*, **49**, 637 (2000).

[7] G.M. Kavoulakis and A. Mysyrowicz, *Phys. Rev. B*, **61-24**, 16619 (2000).

[8] D.B. Tran Thoai and H. Haug, *Solid State Commun.*, **115**, 379 (2000).

[9] D. Roubtsov and Y. Lépine, *Phys. Rev. B*, **61**, 5237 (2000).

[10] E. Benson, *Ph.D. dissertation*, 140 (1999).

[11] E. Benson, *M.Sc. dissertation*, 80 (1995).

[12] E. Benson, E. Fortin, B. Prade and A.Mysyrowicz, *Europhys. Lett.*, **40**(3), 311 (1997).

[13] M. Kavoulakis, G. Baym and J.P. Wolfe, *Phys. Rev. B*, **53**, 7277 (1996).

[14] K. O'Hara, *Ph.D. dissertation*, (1999).

[15] N. Caswell, J.S. Weiner and P.Y. Yu,*Solid State Commun.*, **40**, 843 (1981).

[16] D.W. Snoke, A.J. Shiels and M. Cardona,*Phys. Rev. B*, **45**, 11693 (1992).

[17] A.I. Bobrysheva and S.A. Moskalenko,*Phys. Status Solidi (b)*, **119**, 141 (1983).

[18] J.L. Lin and J.P. Wolfe,*Phys. Rev. Lett.*, **71**, 1222 (1993).

[19] L.V. Gregor,*Jour. Chem.*, **66**, 1645 (1962).

[20] D. Snoke, J.P. Wolfe, and A. Mysyrowicz, *Phys. Rev. B*, **41**, 11171 (1990).

[21] D.W Snoke, J.P. Wolfe and A. Mysyrowicz, *Phys. Rev. Lett.*, **64**, 2543 (1990).

[22] E. Hanamura and H. Haug,*Phys. Rep. C*, **33**, 209 (1977).

[23] A. Imamoglu, R. J. Ram, S. Pau, and Y. Yamamoto,*Phys. Rev. A*, **53**, 4250 (1996).

[24] D. Hulin, A. Mysyrowicz and C. Benoit a la Guillaume, *Phys. Rev. Lett.*, **45**, 1970 (1980).

[25] D. Snoke, J.P. Wolfe, and A. Mysyrowicz, *Phys. Rev. Lett.*, **59**, 827 (1987).

[26] A. Mysyrowicz, D. Snoke and J.P. Wolfe, *Phys. Stat. Sol. (b)*, **159**, 387 (1990).

[27] E. Tselepis, E. Fortin and A. Mysyrowicz, *Phys. Rev. Lett.*, **59**, 2107 (1987).

[28] E. Fortin and W.M. Sears, *Can. J. Phys.*, **60**, 901 (1982).

[29] L.C. Olsen and R.C. Bohara, *Appl. Phys. Lett.*, **34**, 47 (1979).

[30] J. Bardeen, *Phys. Rev.*, **71**, 717 (1947).

[31] A.A. Berezin and F.L. Weichman, *Phys. Stat. Sol. (a)*, **71**, 265 (1992).

[32] C. Olsen, F.W. Addis and W. Miller, *Solar Cells*, **7**, 247 (1982-1983).

[33] L. Hanke, D. Fröhlich and H. Stolz, *Solid State Commun.*, **112**, 455 (1999).

[34] P.W. Baumeister, *Phys. Rev.*, **121-2**, 359 (1961).

[35] K. Bennett and R.L. Byer, *Appl. Opt.*, **19**, 2408 (1980).

[36] A. Mysyrowicz, E. Benson and E. Fortin, *Phys. Rev. Lett.*, **77**, 896 (1996).